Chapter 5

Profile Optimization for Wet-Printed Polymer Films

5.1 Overview

In Chapter 4 we introduced a new wet printing method to pattern the organic light-emitting materials used for full-color OLED applications. A big challenge faced by most wet-printing techniques, including LAMP, is to achieve a uniform printed film thickness. As can be seen from Figure 4.15b, Figure 4.16d and Figure 4.17, the printed layer after the evaporation of solvents are usually not uniform in thickness. Since a uniform film thickness is critical for a uniform light emission and thus brightness, the wet-printing process need to be optimized to result in a more uniform thickness. In this chapter, different approaches are used to improve the printed film thickness. They are a co-solvent approach, a surfactant approach, and a solvent vapor annealing approach.

The information in this chapter was presented in Ref. [33–35].

5.2 Profile Non-Uniformity

A non-uniform film thickness of the organic film is a common issue for wet printing techniques, including ink-jet printing [4, 11, 44, 58] and our LAMP method. A typical cause of the un-even surface is the so-called "coffee ring effect", first modeled by Deegan [18]. When the contact line is pinned, liquid evaporating from the edge is replenished by liquid from the interior of the drying droplet. Solute is carried out to the edge as a result of the outward flow, and a ring-shaped pile up of materials is formed. In some other cases, material piles up in the droplet center, or both can occur at the same time. In order to achieve a uniform film across the pixel, the drying process needs to be well controlled. Parameters affecting the final film profile include surface energy of the substrate, surface tension of the ink, solid content, solvent evaporation rate, drying condition (such as vapor pressure, drying temperature, air flow), drying time, etc. For example, Shimoda et al from Epson-Seiko [58] observed that by varying the printing speed from 5 mm/s to 0.5 mm/s and thus changing the drying condition, more solute was deposited near the edge, rather than in the center.

Many efforts have been taken by various groups, in order to optimize the deposited film uniformity. Cambridge Display Technology used a high-boiling-point solvent to minimize the evaporation rate to separate the drying process from the printing process. Rather flat profiles have been achieved by controlling the drying process parameters but the details of the optimization process are not given in their paper [4, 11]. Lee et al at Samsung were able to achieve flat profiles in the center by optimizing the ink properties [44]. While many works have been demonstrated in the literature, these reports have left out the processing details. Exactly how to achieve a flat profile remains generally unknown.

In our work, we have used several different approaches to optimize the wet-deposited film uniformity: a co-solvent approach, a surfactant approach, and solvent vapor annealing. Our experimental results for each method are given below.

5.3 Co-solvent Approach for a Uniform Profile

A co-solvent (a mixture of two solvents or more) approach has been utilized to tune the distribution of solute during solvent evaporation process [3, 16]. de Gans and Schubert [16] observed that by using 20 wt% of acetophenone and 80 wt% ethyl acetate, the shape of the deposited polystyrene films changed to a cylindrical shape, from the original ring shape when ethyl acetate only is used. In another work by Arias [3], introducing 20% of acetone in the water solution changes the deposited Ag lines from an edge-concentrating shape to a more distributed one. Although an analytical description of the drying process with co-solvent is not available, the idea behind the introduction of a second solvent is simple. Usually one solvent is chosen to be volatile and the other to be less volatile. During evaporation process, the solvent composition at the edge of the contact line will shift to a composition rich in less-volatile solvent due to the increased evaporation rate at the edge. The resulting composition gradient and surface tension gradient may cause a Marangoni flow from regions with low to high surface tension. This Marangoni flow occurs in addition to the outward flow caused by the coffee ring effect and may homogenize the final solute distribution [3, 16].

In our experiments, we have studied the effects of different pairs of co-solvents on the profile of deposited films, including chlorobenzene-chloroform, dichlorobenzene-chlorobenzene, dichloroethane-xylene. Within the 3 different co-solvent pairs, noticeable improvement of the co-solvent on the final solute profile is only observed with the dichlorobenzene-chlorobenzene pair, and the results are discussed below.

Dichlorobenzene-chlorobenzene co-solvents are prepared at different compositions, with dichlorobenzene varies between 10–50 vol%. For simplicity, only PVK is dissolved as the solute, with a concentration of 13.3 mg/ml. Two different substrates are used to study the effect of co-solvent approach on profile. The first substrate is a flat silicon wafer selectively-coated with PFOTS layers, except for an array of

circular pads with a diameter of 320 μm (same as the printing plate shown in Figure 4.6). Another substrate used is similar to the first substrate, except that the uncoated silicon is etched to a depth of about 700 nm and forms well-shaped structures, similar to the device structures shown in Figure 4.17. For simplicity, the substrates are dip-coated with PVK in co-solvent solution and solvents are allowed to dry in a solvent hood. The lab environment is not well controlled, such as the air flow, room temperature, and humidity. However, results obtained from multiple measurements show good consistency, which assured the validity of our experiments.

Figure 5.1 shows the results of dichlorobenzene-chlorobenzene co-solvent on PVK film deposited on a flat substrate with selective wettability. Six different dichlorobenzene-chlorobenzene co-solvents, with dichlorobenzene varying from 10% to 50% are prepared. The PVK concentration remains the same for all six solutions at 13.3 mg/ml. After the dip-coating, the PVK solution selectively wets the substrate and forms an array of droplets, each with a diameter of 320 μm defined by the surface energy pattern of the substrate. After drying, circular pads of PVK films are obtained. Typical optical micrographs of the dried PVK film are shown in Figure 5.1 for each of the co-solvent composition. As shown on Figure 5.1, PVK films form a ring-shaped pattern in each case, which is caused by the "coffee ring" effect as discussed earlier [18]. The introduction of the second solvent is not able to prevent the formation of the coffee rings. However, it does have significant effect on the solute distribution on the rest of the pattern other than the edge. In particular, PVK films deposited with 15% of dichlorobenzene shown on Figure 5.1b seems to have the best uniformity of contrast.

The effect of co-solvent on profile uniformity is better presented by surface profile scans. As given in Figure 5.2, one-dimensional surface profile scans are performed on the pixels shown on Figure 5.1 and compared to each other. From Figure 5.2, we can clearly see that by introducing dichlorobenzene in chlorobenzene solvent, different profiles are achieved. In particular, the profiles dramatically change in the center

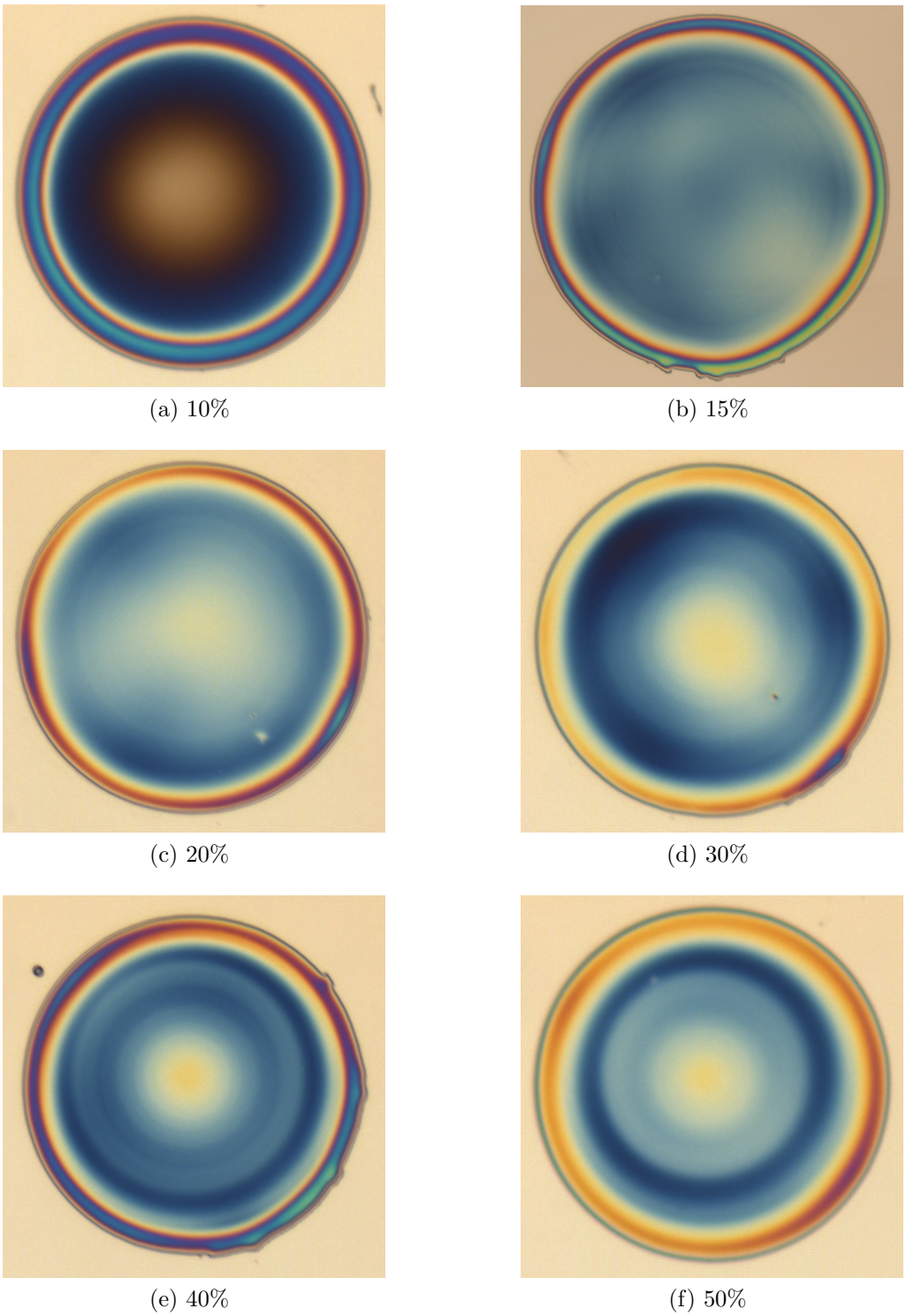

(a) 10%

(b) 15%

(c) 20%

(d) 30%

(e) 40%

(f) 50%

Figure 5.1: Optical micrographs of the dried PVK films on flat substrate versus volume percent of dichlorobenzene in total solvent. Although coffee rings still exist in all six cases, the introduction of dichlorobenzene does change the profile for most of the pixel areas. In particular, the contrast of the deposited PVK film with 15% dichlorobenzene seems to have the best uniformity.

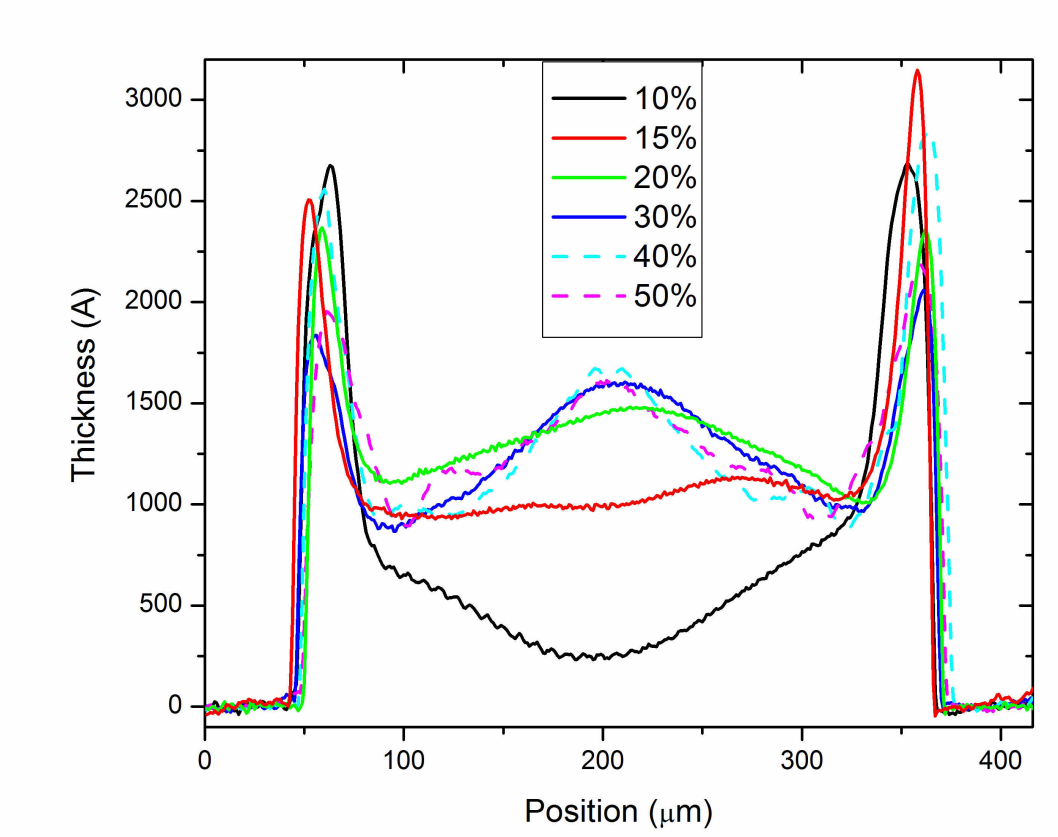

Figure 5.2: Profile scans of PVK films deposited on a flat substrate at various percentage of dichlorobenzene in chlorobenzene solvent, corresponding to Figure 5.1. The best profile is achieved with about 15% of dichlorobenzene.

regions of the pixel. By adding about 15% of dichlorobenzene in the solvent, we can achieve an almost flat profile for most of the circular pad, except the "coffee-ring" edge. A 3D profile scan of the PVK film deposited with 15% dichlorobenzene (Figure 5.1b) is given as Figure 5.3, which confirms the thickness uniformity of the deposited film.

The other substrate type used for our study contained wells. The substrate is made from silicon wafers with wells (diameter 300 μm) etched into the silicon substrate by RIE to a depth of 700 nm. The top surface of the silicon wafer is coated with PFOTS layer, resulting a non-wetting property. PVK in dichlorobenzene-chlorobenzene solutions with various solvent compositions are used as the ink for dip-coating. After

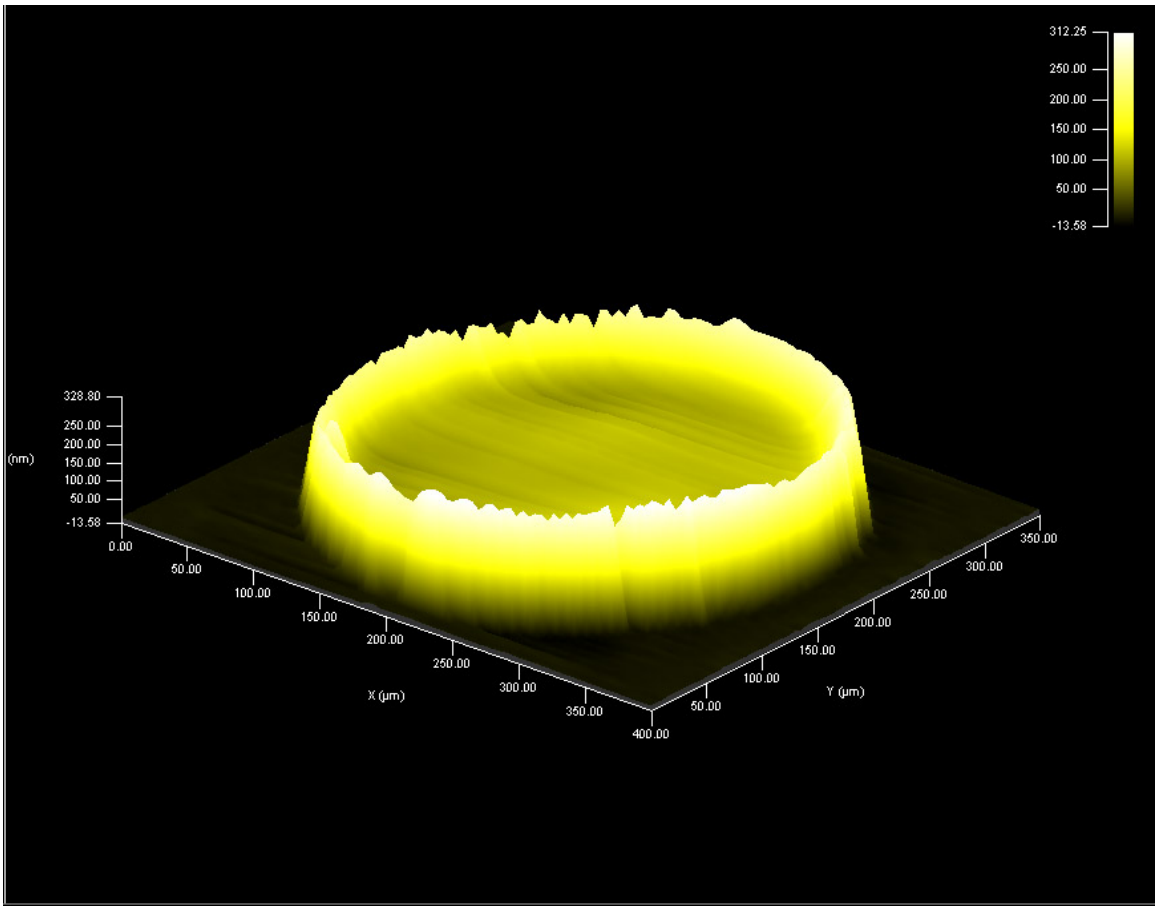

Figure 5.3: 3D profile of PVK film deposited with 15% dichlorobenzene in chlorobenzene solvent, corresponding to Figure 5.1b. The profile is quite uniform in the center, but the "coffee ring" is still present.

drying of the droplets, PVK films deposited in the wells are measured with a surface profiler. Figure 5.4 is the profile scan of the well-shaped substrate being used (first sub-figure), and profiles of deposited PVK films in the well at different solutions with varying dichlorobenzene percent. Similar to results on the flat substrate shown on Figure 5.2, the introduction of dichlorobenzene component in the chlorobenzene solvent has a significant effect on the film thickness. In particular, by adding 15% of dichlorobenzene to chlorobenzene, we can achieve an almost flat profile for most of the pixel area. Again, we are not able to prevent the formation of the coffee-rings, which only occupy the pixel periphery and are small in area compared with the whole pixel area.

While we had a good result with the dichlorobenzene-chlorobenzene pair, we didn't see similar results with other co-solvent pairs, for example the chloroform-chlorobenzene pair. Profiles of dried PVK films from dip-coating with the use of chloroform-chlorobenzene co-solvent are shown in Figure 5.5. The percentages of chloroform in the solvent are marked in each case. As shown in Figure 5.5, we are not able to flatten the profile of the PVK film by using the chloroform-chlorobenzene co-solvent pair.

Note that the two substrates used for experiments shown in Figure 5.4 and Figure 5.5 are slightly different. As shown in Figure 5.5, PVK was deposited to an area ($320\mu m$) that is larger than the well diameter ($300\mu m$). This is because the PFOTS layer used to confine the droplets is patterned by a separate photolithography step after the well formation, and the PFOTS pattern is not aligned to the well bank. The substrate used in Figure 5.4, however, was made by a self-aligned approach. In this approach, a blanket layer of PFOTS is first coated on the silicon surface. Then both the PFOTS layer and the silicon substrate are patterned by a single photolithography and RIE etch step. As a result, the PFOTS layer left is self-aligned to the well edges. One challenge of this procedure is to spin coat the photoresist on the PFOTS-coated

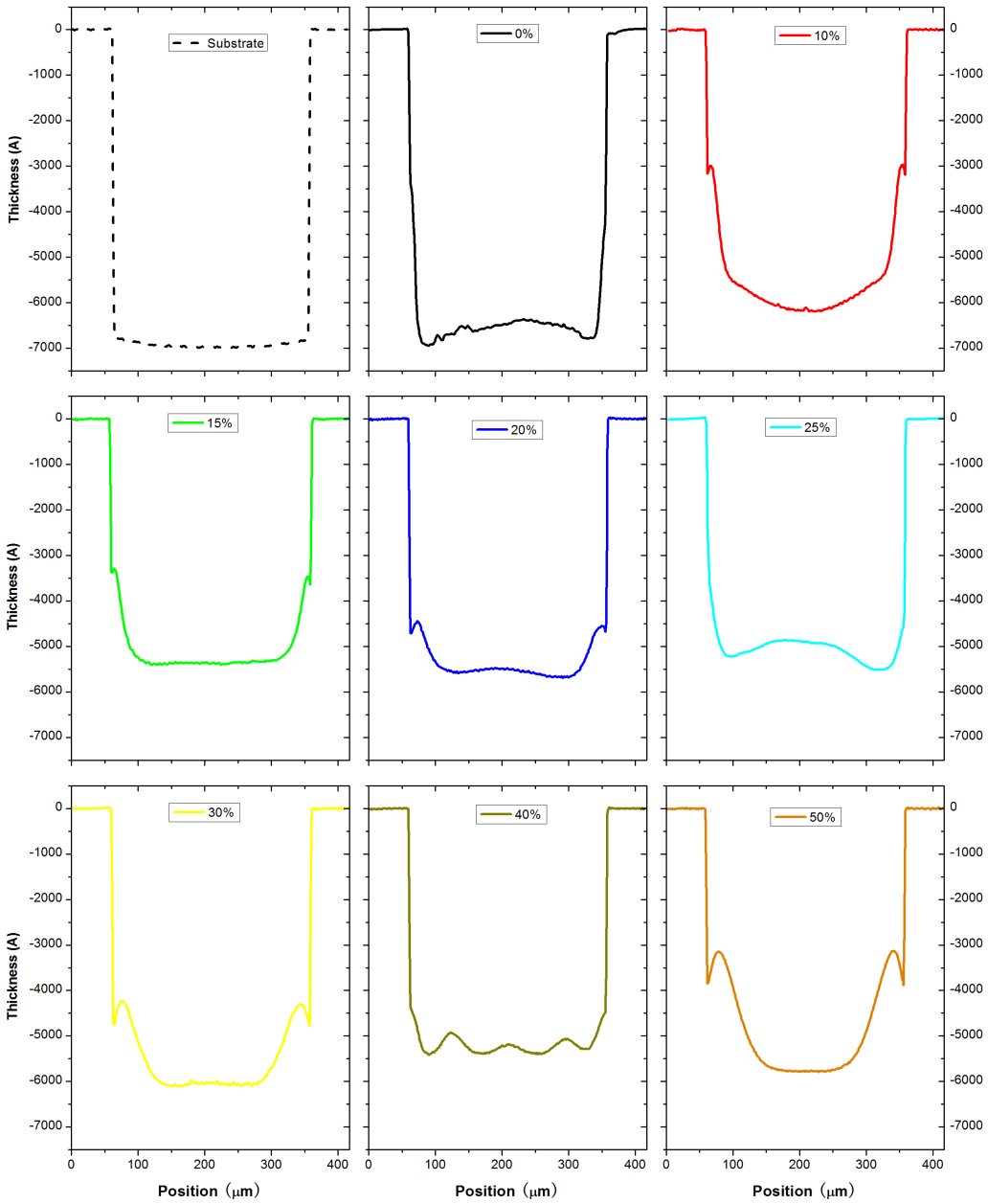

Figure 5.4: Typical profile of PVK film deposited into a well vs. the percentage of dichlorobenzene in chlorobenzene solvent. The first sub-figure shows the well-shaped substrate being used for all experiments. The best profile of the deposited film is achieved at about 15% of dichlorobenzene in chlorobenzene.

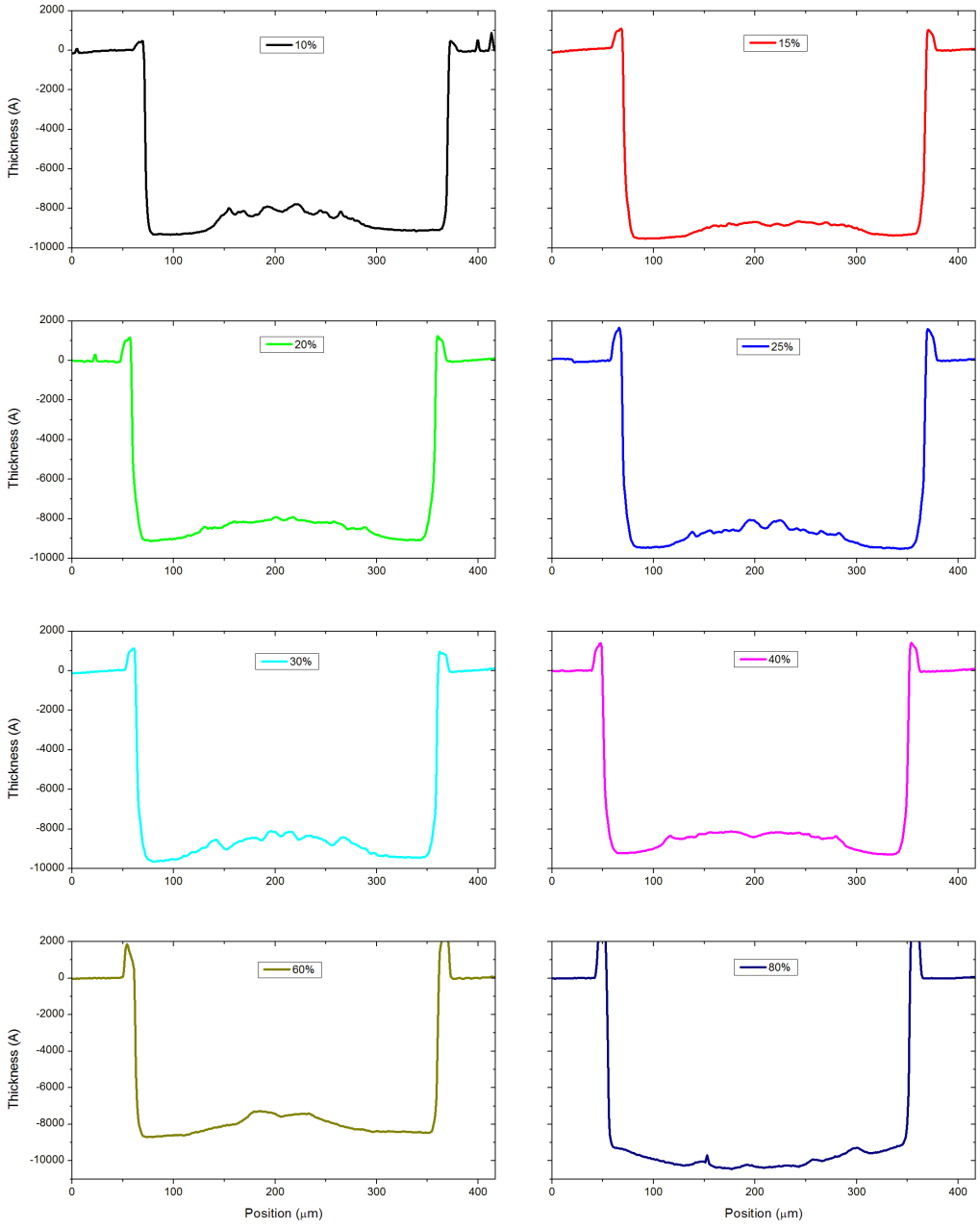

Figure 5.5: Typical profile of PVK film deposited into a well vs. the percentage of chloroform in chlorobenzene solvent. It is difficult to achieve a flat profile.

Table 5.1: Key properties of several solvents at $25°C$

Solvent	Boiling point($°C$)	Vapor pressure (KPa)	Surface tension (mN/m)
Dichlorobenzene	180	0.18	35.43
Chlorobenzene	132	1.6	32.99
Chloroform	61	26.2	26.67

silicon substrate, which is non-sticky. We found out that a slow ramp up of the spinning process (for example, ramp up to 500 rpm with a rate of 100 rpm/s for 5 seconds, then to the final spinning speed with a rate of 1000 rpm/s) solves the problem quite well.

It is not clear why the addition of about 15% dichlorobenzene in the solvent of chlorobenzene improves the profile of printed PVK films, while the addition of chloroform did not result in similar improvements. An intuitive explanation to the question can't be generated by comparing the key properties of the solvent being used, as shown in Table 5.1. For example, one way of reasoning is to compare the vapor pressure and surface tension of the two solvents used in a co-solvent system [16]. In the case of dichlorobenzene-chlorobenzene system, the dichlorobenzene has a slow evaporation rate and thus will accumulate at the droplet contact line during the drying process. Since dichlorobenzene has a higher surface tension than chlorobenzene, the surface tension gradient will tend to pull the liquid from the droplet center to the contact line. In the case of chlorobenzene-chloroform, chlorobenzene is the slow-evaporation-rate component and will accumulate at the contact line. Since chlorobenzene has a higher surface tension than chloroform, the surface tension gradient also pulls the droplet from the center to the contact line. So this similarity of the two different co-solvent system could not explain the difference they have on the final profile of the printed PVK films. One possible factor might related to the chemical similarity between dichlorobenzene and chlorobenzene.

In a short summary, we are able to tune the profile of printed PVK films by the use of a dichlorobenzene-chlorobenzene co-solvent pair. However, other co-solvent

pairs did not result in similar improvement in the profile of PVK films. We don't have an intuitive answer to the question of how exactly the use of dichlorobenzene-chlorobenzene co-solvent can flatten the profile of printed PVK films, and why other co-solvent pairs did not work the same way. Further, we have not yet tested the effect of the use of dichlorobenzene solvent on the device performance due to time limit. Instead we explored the surfactant approach that will be discussed in the next section.

5.4 Surfactant Approach for a Uniform Profile

In addition to the co-solvent approach discussed in the last section, we have also used a surfactant approach to optimize the profile of wet-printed films. Surfactants are usually organic compounds that are amphiphilic, which means that they contain both hydrophobic and hydrophilic groups. Surfactant reduces the surface tension of water or other liquids, such as paints and other coating materials, so that it helps to achieve a better wetting, spreading or film uniformity in the final dried layer.

Truskett et al [63] studied the effect of surfactant at different concentrations on the pattern formed by dried microspheres. The use of surfactant can change the flow field within the drop, by either changing the stress conditions or by changing the local evaporation rate in the vicinity of the contact line. Truskett found out that by adding a surfactant, pentadecanoic acid (PDA), to an aqueous suspension containing polystyrene microspheres, it is possible to get different patterns of the dried particles. In particular, in one of their observed phases no coffee ring is formed and the particles are deposited (although unevenly) everywhere under the drop [63]. The results indicate that the surfactant accumulates near the contact line, which is sufficiently pronounced to retard evaporation near the contact line relative to the rest of the drop surface [63]. This would eliminate the outward flow that caused the coffee

ring otherwise.

Inspired by earlier work with surfactants, we also studied the usage of surfactants to optimize the profile of our wet-deposited light-emitting layers.

5.4.1 BASF Pluronic Surfactant

The first surfactant that we tested is Pluronic L62 (purchased from BASF). PVK in chlorobenzene solution is used as the ink, with a concentration of 13.3 mg/ml. Surfactant L62 is added to the solution at 0.01%, 0.05% and 0.1% (volume ratio to chlorobenzene). The silicon wafers with wells etched in them mentioned in Section 5.3 are used as the substrate. Three different substrates are made, with well depths at 250 nm, 410 nm and 700 nm, respectively, to study the possible effect of well depth (and well bank) on the final profiles. Dip-coating is again used to coat the substrate with the PVK solution, and the dried PVK film profile is then measured. The results are shown in Figure 5.6. Three profile scans are given in each of the sub-figures, corresponding to the three substrates with different well-depth. The position of the well-bottom of each substrate is illustrated by dashed lines. Figure 5.6a shows the original profiles when no surfactant is added to the solution. With the addition of L62 surfactant in the solution, the profiles become more and more flat. With L62 at 0.1%, the PVK film is almost flat, as shown in Figure 5.6d.

It is of vital importance to study the effect of surfactant on the device performance. For that purpose, PVK+PBD+C6 mixture solutions with 0.05% L62 and without L62 are prepared. Regular OLEDs with spin-coated PVK+PBD+C6 layer, as outlined in Chapter 3 are fabricated and tested. The device curves are shown in Figure 5.7. Control devices without L62 surfactant are shown in solid lines and devices with surfactant are in dashed lines. As shown on the I-V curves in Figure 5.7a, there is a 4–10 volts increase of the driving voltage due to the addition of L62 in the solution at 0.05%. A huge decrease in the light emission is also observed with the addition of

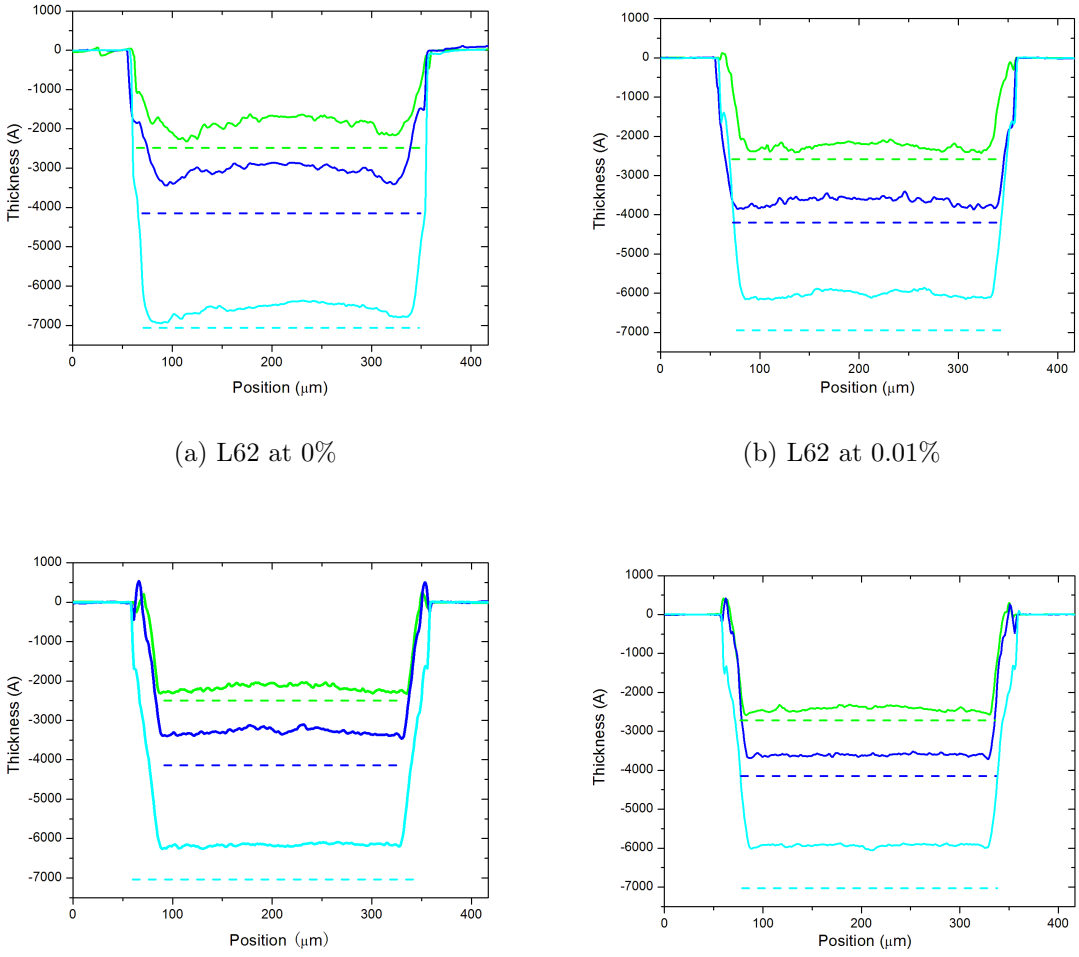

(a) L62 at 0%

(b) L62 at 0.01%

(c) L62 at 0.05%

(d) L62 at 0.1%

Figure 5.6: Profile of deposited PVK films (solid lines) versus L62 concentration in the solution. Three different substrates with well depth at 250 nm, 410 nm, 700 nm are used for the study and the profile of the wells are illustrated by dashed lines. PVK profiles are almost flat with 0.1 vol% of L62 added to the solution.

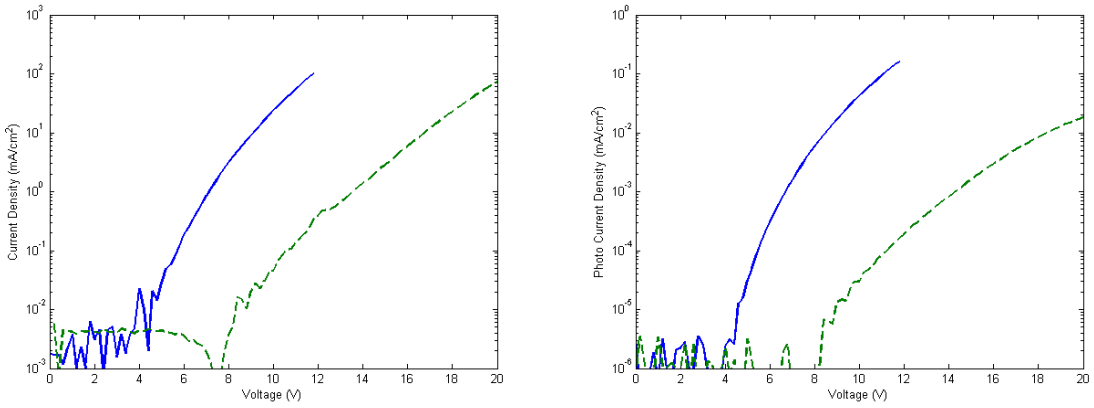

(a) OLED current vs. applied voltage (b) Collected photocurrent vs. applied voltage

Figure 5.7: Device curves of OLEDs without surfactant (solid line) and with L62 surfactant at 0.05% (dashed line) added to the solution. PVK+PBD+C6 is used as the light-emitting layer. The addition of small amount of L62 surfactant caused significant degradation to the OLED device performance.

a small amount L62 surfactant in the solution, as can be seen from Figure 5.7b.

In summary, the use of L62 surfactant can successfully flatten the wet-deposited PVK films. However, the addition of L62 surfactant to the solution degrades the final device performance, so that the use of L62 is not acceptable.

5.4.2 3M Fluoro-Surfactant

Since the L62 surfactant has a severe negative effect on the prepared device performance, we seek another surfactant that can flatten the PVK profile at lower concentrations. We came across a new type of surfactant, Novec Fluorosurfactant from 3M, which was claimed to be very efficient. Table 5.2 compares the effect of surface tension reduction by L62 and 3M Novec FC-4432. By adding 0.1% of L62, the surface tension of water decreased from 72 to 43 mN/m. By using FC-4432 at the same concentration, however, the water surface tension was lowered to only 21 mN/m. This comparison clearly shows that FC-4432 is more effective and efficient than L62 and is a good candidate to be studied.

Table 5.2: Comparison of surfactant on the effect of reducing surface tension of water

Surfactant	Concentration in water	Surface Tension (mN/m)
None	(pure water)	72
BASF Pluronic L62	0.1%	43
3M Novec FC-4432	0.1%	21

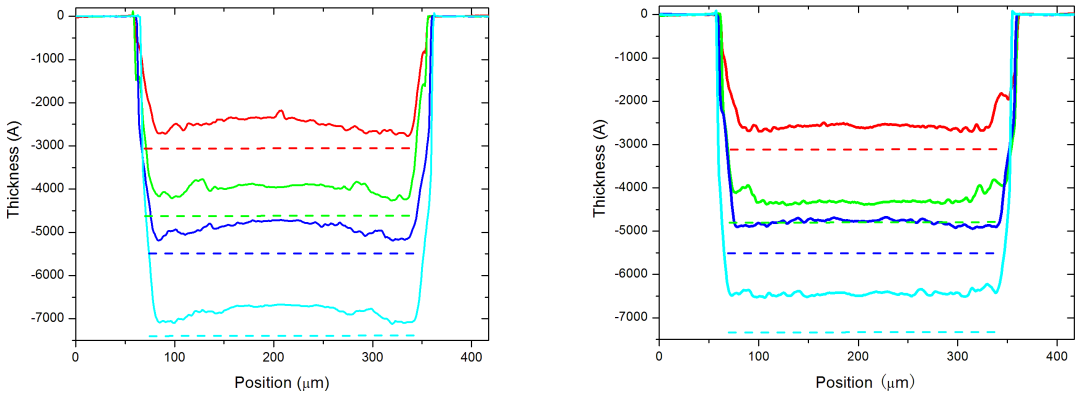

(a) FC-4432 at 0.0009 wt%

(b) FC-4432 at 0.0045 wt%

Figure 5.8: Profiles of deposited PVK films (solid lines) with the addition of FC-4432 surfactant. Four substrates with different well depth (illustrated with dashed lines) are used for the study. PVK profiles are almost flat with 0.0045 wt% of FC-4432 in the solution.

FC-4432 is added to the PVK in chlorobenzene at two different concentrations, 1×10^{-5} g/ml (0.0009 wt%) and 5×10^{-5} g/ml (0.0045 wt%). Dip-coating is again used to deposit PVK layers on well-shaped silicon substrates, with different well depths. The results are shown in Figure 5.8. Four profile scans are given in each of the sub-figures, corresponding to four different well-depth. The position of the well bottom for each substrate is illustrated with a dashed line. Notice that the addition of FC-4432 surfactant to the solution greatly improves the uniformity of the film profiles, and an almost flat profile is achieved in the center of the well with FC-4432 at only 0.0045 wt%, despite the fact that coffee rings still exist. Compared with the results of the L62 surfactant, the required amount of surfactant to achieve a flattened profile has been greatly reduced.

In order to better illustrate the importance of thickness uniformity, OLED pixels are fabricated to study the electroluminescence properties. The device structure is shown in Figure 5.9a. ITO-coated glass is used as the substrate and a thin layer of SiN_x is deposited on top of the ITO layer. The top surface of the SiN_x is coated with PFOTS so that it can de-wet the PVK in chlorobenzene solution. 300 μm-diameter wells are etched into the SiN_x layer which also define the active area for each OLED pixel. PVK layers are deposited by dip-coating of the PVK solution, either without the addition of surfactant (control device) or with FC-4432 at 0.0045 wt%. Profiles of the deposited PVK films are shown in Figure 5.9b, together with the well profile. The PVK film deposited without surfactant is uneven while the surfactant optimized PVK film is rather uniform, especially in the center region. Finally, a Mg:Ag cathode is deposited on top of the PVK film to finish the device fabrication. Due to the small dimension of the pixels (300 μm), a reverse optical microscope[1] is used to capture the pixel micrographs under electroluminescence. Figure 5.9c is an electroluminescent micrograph of a pixel from devices containing un-optimized PVK layers. Due to the thickness variation, the light emission is not uniform from the whole pixel area. Figure 5.9d is an electroluminescent image of pixel from optimized devices. The light emission uniformity has been greatly improved, as a direct result of the improved PVK layer thickness. Notice that close to the pixel edge, denoted by a white circle line, the coffee ring effect caused PVK to pile up, which further resulted in the reduction in light emission. The dark region, however, is small compared to the whole area of the pixel.

Although the profile after optimization sees great improvement in film uniformity, small variations of the film thickness still exist. The same pixel shown on Figure 5.9d is also surface scanned by AFM, shown as an overlay on the electroluminescent image, as in Figure 5.10. We have reversed the regular AFM contrast so that thin areas are

[1]The OLEDs are bottom emitting devices so the microscope lens needs to be located underneath the OLED pixel and looking upwards.

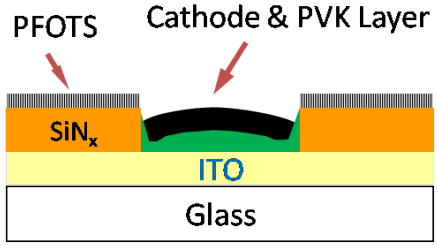

(a)

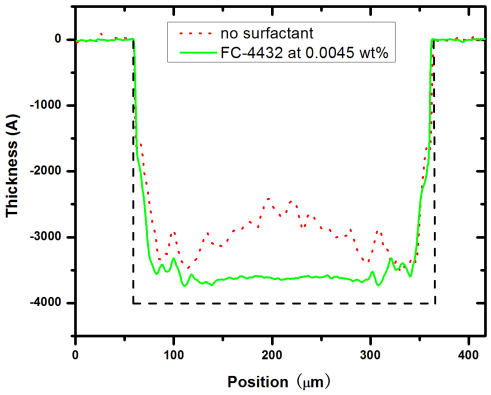

(b)

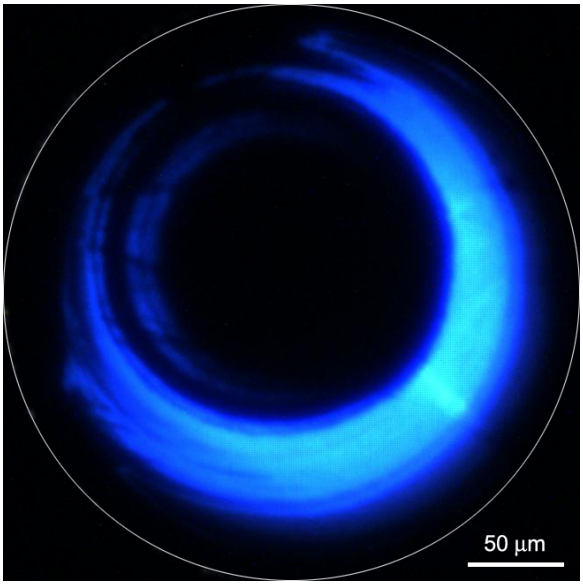

(c)

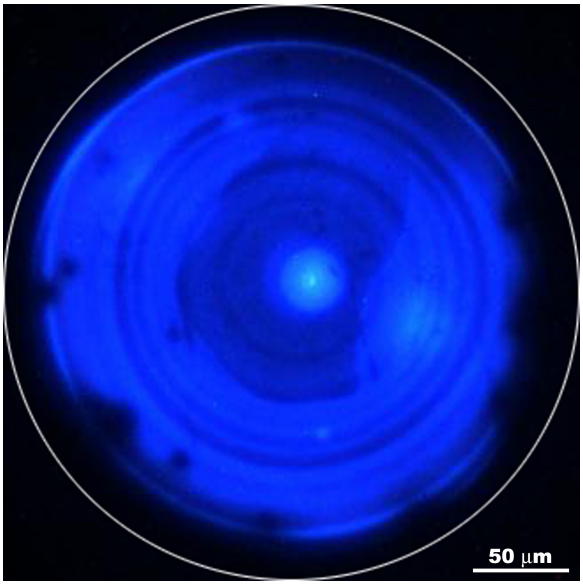

(d)

Figure 5.9: Effect of profile on electroluminescence uniformity. (a) Schematic of the device structure. (b) Typical profiles without surfactant and with FC-4432 at 0.0045 wt%. Dashed lines shows the well profile. (c) Electroluminescent micrograph of a 300 μm-diameter pixel with PVK layer deposited without profile optimization. (d) Electroluminescent micrograph of a 300 μm-diameter pixel with optimized PVK layer profile. White circles denote the pixel edges defined by the well opening.

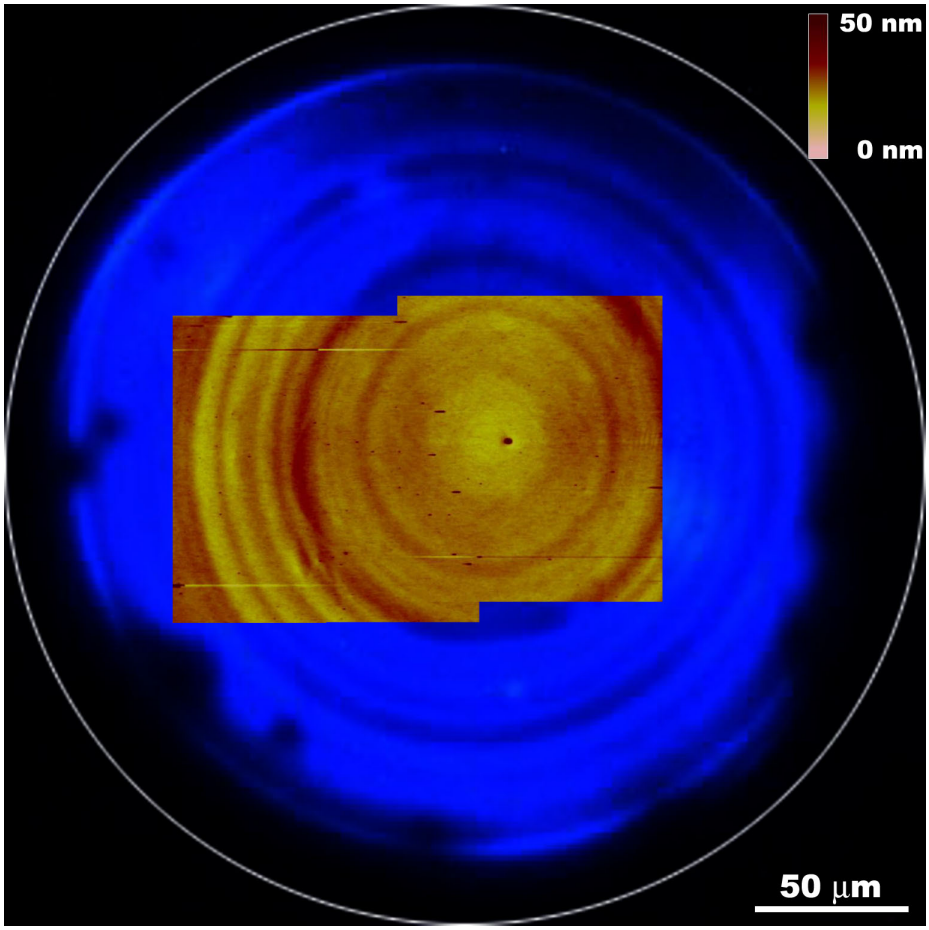

Figure 5.10: AFM surface area scan in overlay with the electroluminescent image. The two images have a great match of contrast with each other, which indicates that thick films of the light-emitting layers resulted in dimmed light emission.

shown with bright contrast and thick areas are shown with dark contrast. A close exam of the overlay image indicates that there is a great match of contrast patterns between the AFM scan and the electroluminescence image, i.e., dark circular patterns (thick film) found on the AFM pattern match with dark circular patterns (dimmed light output) on the electroluminescence image. The results clearly demonstrate that the uniformity of the OLED light emission is controlled by the thickness of the light emitting layer which further confirms the importance of profile optimization.

Similar to L62, we also studied the effect of the FC-4432 surfactant on device performance. FC-4432 is added to the regular PVK+PBD+C6 solutions at a concentration of 0.0045 wt%. Regular OLEDs with spin coated PVK+PBD+C6 layer as the

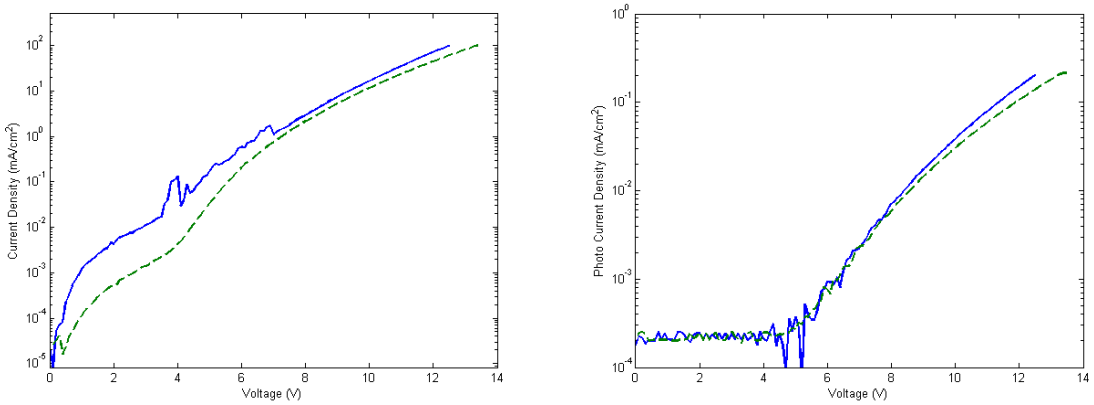

(a) OLED current vs. applied voltage (b) Collected photocurrent vs. applied voltage

Figure 5.11: Device curves of OLEDs without surfactant (solid line) and with the addition of FC-4432 surfactant at 0.0045 wt% (dashed line). PVK + PBD + C6 is used as the light-emitting layer. Only little changes on the curves are seen.

light emitting layer are fabricated and tested. The device curves are shown in Figure 5.11. Control devices without the surfactant are shown as solid lines. As shown on the I-V curves (Figure 5.11a) and on the photocurrent curves (Figure 5.11b), only little changes on the curves are seen with the addition of the FC-4432 surfactant. We attribute this result to the fact that a small amount of the surfactant does not change the optical or electrical properties of the printed film. As a conclusion, FC-4432 surfactant can be used to flatten the PVK profile, which has little negative effect on the device performance.

5.4.3 Unsolved Issues Related to Surfactant Approach

The effect of surfactant on the improvement of deposited film profiles has been summarized so far in the last two sections. We note, however, that the improvement has only been observed on single-solute (PVK) solutions. Solutions with multiple solutes seem to be more complex and require extra work to be optimized.

For example, although L62 has been found effective in flattening the profile of deposited PVK films, we were not able to get a flat profile when PVK+PBD+C6 is

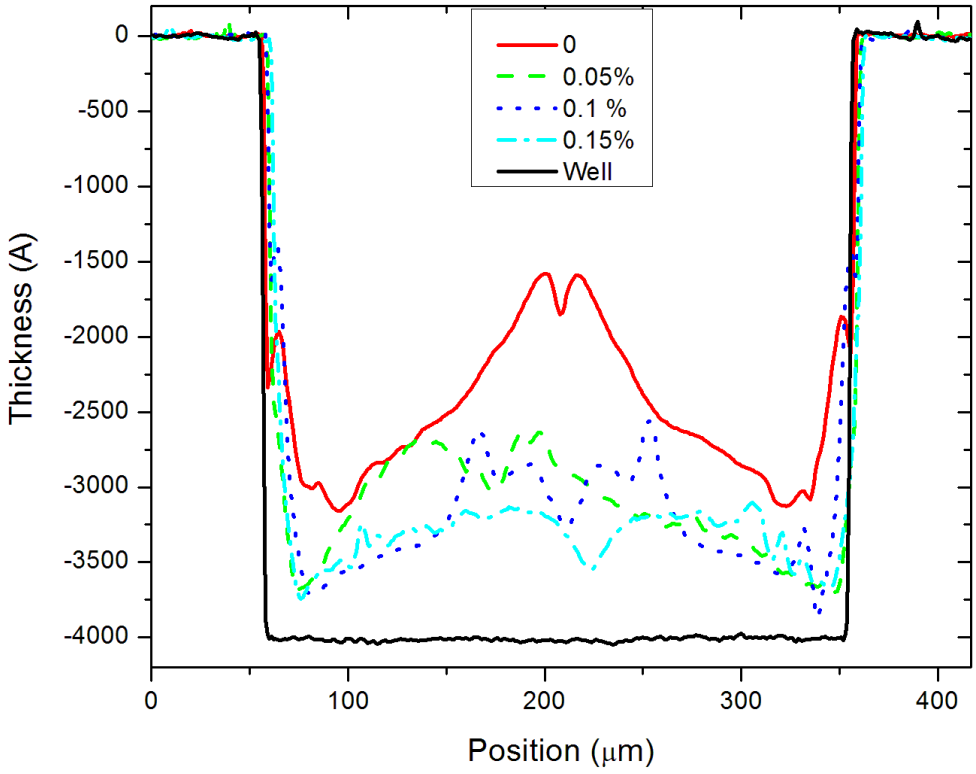

Figure 5.12: The profiles of PVK+PBD+C6 film vs the concentrations of L62 in the solution. The use of L62 does not flatten the profile of the mixture.

used as a mixture. Figure 5.12 shows the results of deposited PVK+PBD+C6 layers onto a 400 nm-depth well made from silicon wafer by dip-coating. By adding L62 surfactant at either 0.05%, 0.1% or 0.15%, the deposited PVK+PBD+C6 film is still very rough. Further, adding more L62 to the solution does not improve the profile uniformity either.

For FC-4432, results are similar. Figure 5.13 shows the effect of FC-4432 on the profile when multiple-solute solutions are used. FC-4432 are added at 0.0045 wt% to solutions containing (a)PVK+PBD+C6 (b)PVK+PBD (c)PVK+C6. A composition ratio of PVK:PBD:C6=100:40:0.3 is used, which is the same composition used for our green OLEDs. As can be seen from Figure 5.13, FC-4432 does not improve the

profile in all three cases. In particular, the result shown in Figure 5.13c is surprising, since all other parameters are kept the same compared to the results shown on Figure 5.9b, except that here 0.3 wt% of C6 is mixed with PVK. The strikingly different outcome from Figure 5.9b and Figure 5.13c suggest that even a very small amount of a second solute in the solution makes the system very complex, and thus difficult to be optimized.

5.4.4 Solvent Vapor Annealing

The deposited PVK films after surfactant optimization are almost flat in the center part of the pixels. However, small thickness variations can still be observed on the optimized profiles, as shown in Figure 5.10. A solvent-vapor-annealing method has been utilized to further smooth the profiles [2], since a solvent-vapor can depress the effective glass transition temperature of the polymer.

The PVK films resulting from our FC-4432 surfactant optimization is further treated with saturated chlorobenzene solvent vapor in a closed beaker with extra solvent. The substrate is removed from the solvent vapor after some period of time and exposed to air and allowed to dry. Some results from the solvent vapor annealing are shown in Figure 5.14. Figure 5.14a and Figure 5.14b are optical micrographs of the PVK film before and after the annealing for 2 hours. PVK thickness profiles before and after the annealing are given in Figure 5.14c. We can see that after the annealing, the PVK film is very smooth and the coffee rings have disappeared. However, the once-flat profile in the center of the pixel is not flat anymore. Instead, the PVK film profile curves out in a sphere shape, which is not preferred. Further studies are needed to explorer the possibility of retaining the large scale flat profiles while smoothing out any small-scale thickness variations.

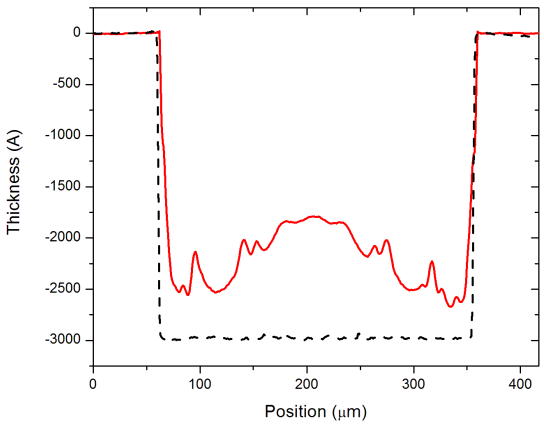

(a) PVK+PBD+C6

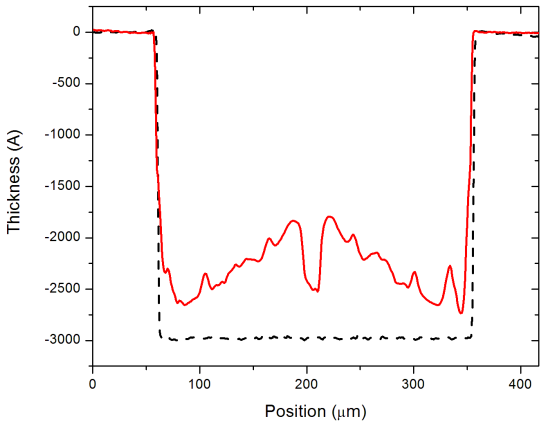

(b) PVK+PBD

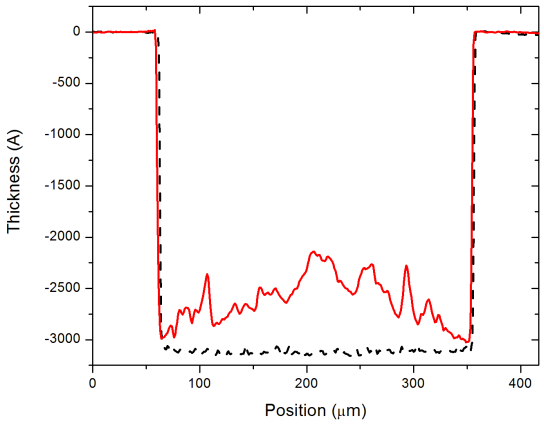

(c) PVK+C6

Figure 5.13: The effect of FC-4432 at 0.0045 wt% on the profiles of mixtures. A composition ratio of PVK:PBD:C6=100:40:0.3 is used. The well profile is given as dashed lines.

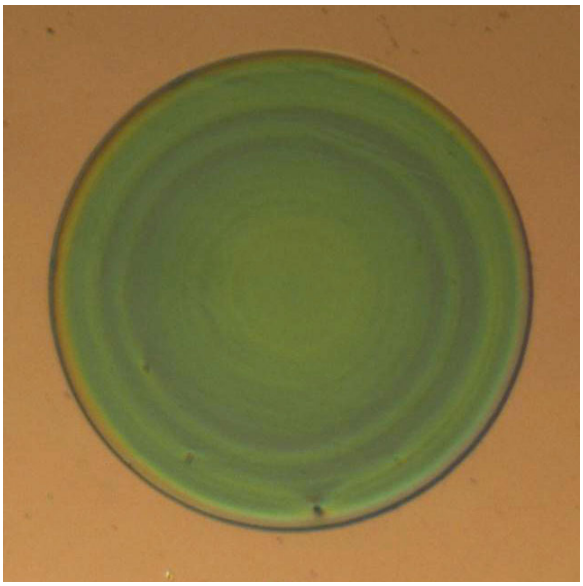

(a) Before annealing

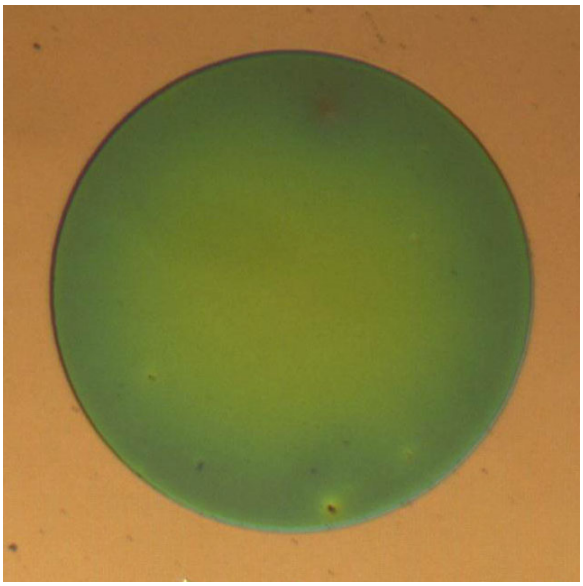

(b) After annealing

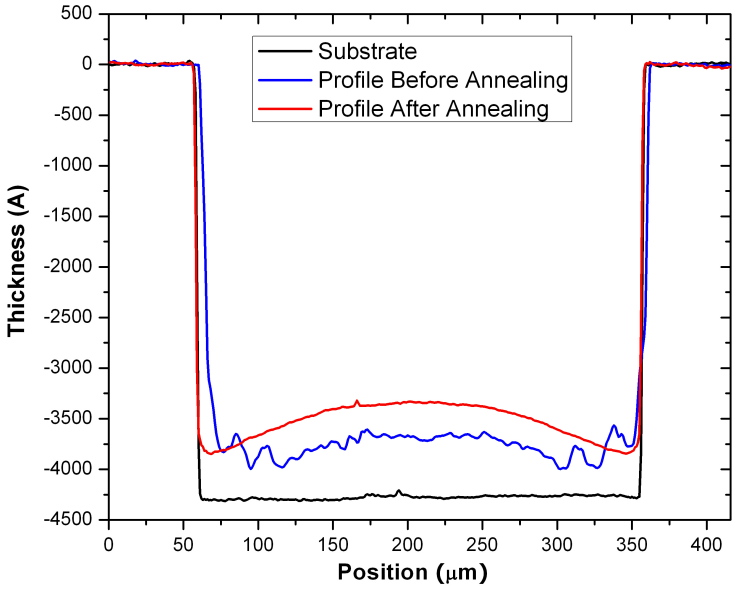

(c) Profiles

Figure 5.14: Effect of solvent vapor annealing on profiles.

5.5 Droplet Profile Study

In order to study the effect of surfactant on the profiles of deposited films, the droplet shape during solvent evaporation process has been investigated. The most direct method to observe the droplet profile vs. time is to directly observe its profile by imaging from the side of the drop, parallel to the surface. This is straightforward when the droplet height is on the order of tens or hundreds of microns. For typical wetting angles, this requires a lateral droplet size on the order of at 1 mm or more, which is much larger than the size of a typical OLED pixel. Therefore in this study we used interferometry to observe the droplet profile in real time [30, 64]. This method has been used before to study droplet drying dynamics for droplets on the size scale of a few hundred microns in size or larger [30]. In this work, we use the method to measure droplets with dissolved polymer.

The diagram of the laser interferometer is shown schematically in Figure 5.15 and the setup used in our lab is shown in Figure 5.16. The interferometer operates by the interference of reflection of a normal laser beam from the liquid-air interface of the droplet and the reflection from the liquid-substrate interface (Figure 5.15). Bright fringes occur at every $\lambda/2n$ increase in depth of the droplet, where n is the refractive index of the liquid. We used chlorobenzene (n = 1.52) and trichlorobenzene (n = 1.57) solvents. For the laser beam (He-Ne, $\lambda = 632.8nm$), a rotational diffuser is used to reduce speckle effect (Figure 5.16b). The height difference of the surface of the droplet between two neighboring fringes are then about 0.2 μm for both cases.

The substrates used for the printing were ITO-coated glass, with a 100-nm thick SiN_x layer deposited on top of the ITO layer. The top surface of the SiN_x is coated with PFOTS so that it can de-wet the printed droplets. 300 μm-diameter wells are etched into the SiN_x layer. Droplets on the surface were printed by dip-coating the substrate into the solvent (or polymer solution) and removing them at a rate of $\sim$5 mm/s. This process left solvent droplets in the surface inside all of the PFOTS-free

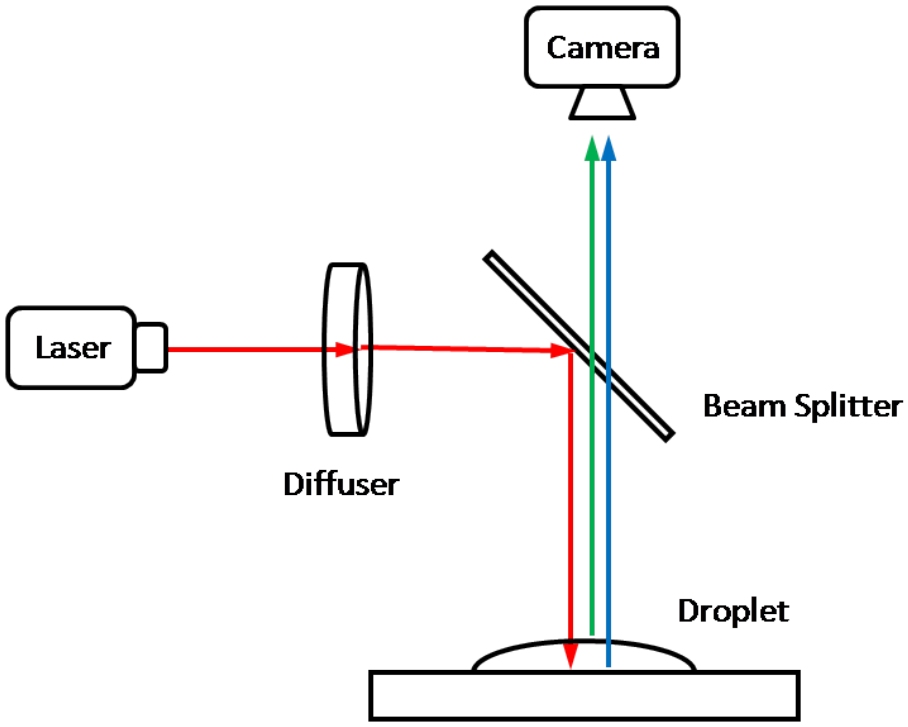

Figure 5.15: Schematic diagram of the laser interferometer used to study the evolution of droplet profiles during evaporation.

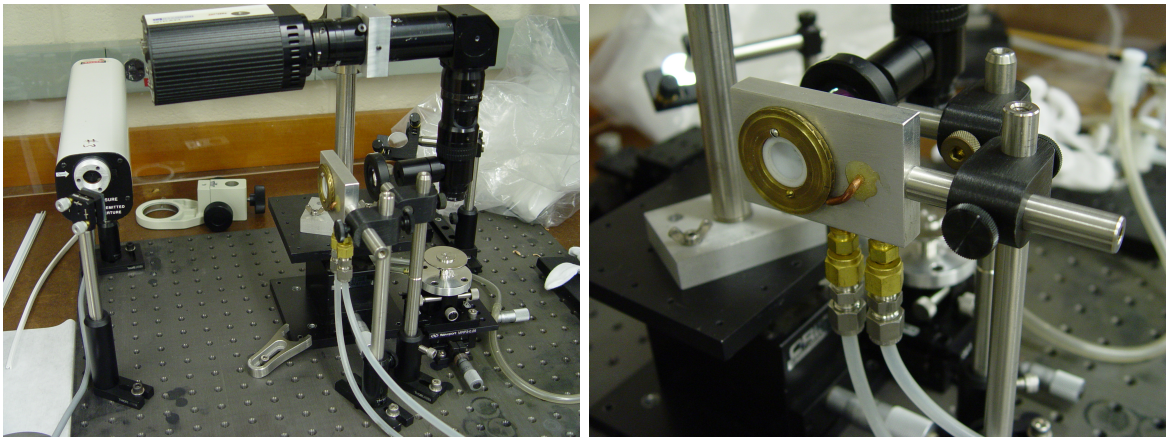

(a) Overall setup (b) Rotational diffuser

Figure 5.16: Laser interferometer setup used for droplet profile study.

regions. The sample was then immediately placed into the interferometer.

Figure 5.17 shows typical images of interference ring patterns captured with pure trichlorobenzene droplet. As the solvent evaporates, a series of frames are captured with a CCD camera. Five frames from the sequence are shown in Figure 5.17. Rings are observed to move inwards and disappear in the center as solvent evaporates and the droplet height decreases. From the captured ring patterns, we can regenerate the droplet height profile. First the intensity of the ring pattern along a line through the center is measured. For example, the line scan of Figure 5.17c is shown in Figure 5.18. From Figure 5.18 the position of peaks and valleys can be found. As discussed earlier, the height difference from neighboring ring peaks (or valleys) is about 0.2 μm. Assuming the profile height decreases from center to edge, we can plot a relative height profile of the droplet according to the captured ring pattern.

However, the absolute height of the droplet is still unknown. Since small droplets normally follow spherical shapes due to surface tension, we can fit the relative height profiles to spherical curves and the absolute height can be find from the fitting parameter. Since in our case the droplet diameter is known or can be directly measured, the only parameter used for the fitting is the absolute height of the droplet in center. The best curve fitting is found with the method of least squares.

Figure 5.19 is an example of the droplet profile evolution during solvent evaporation. The droplet is 300 μm in diameter and contains only trichlorobenzene. The five frames of the ring patterns shown in Figure 5.17 were analyzed and their respective height profile were calculated and fitted to spherical curves (solid lines). The time of the five frames are 0, 30, 60, 80, 104 Sec, with their height profiles shown in the figure from top to bottom, respectively. The third curve from top and its data points are calculated from the line scan shown in Figure 5.18. Notice that in the 5th frame (the bottom curve) the droplet shrank to a smaller size due to solvent evaporation and contact line unpinning. From Figure 5.19 we can see that the data points all fit

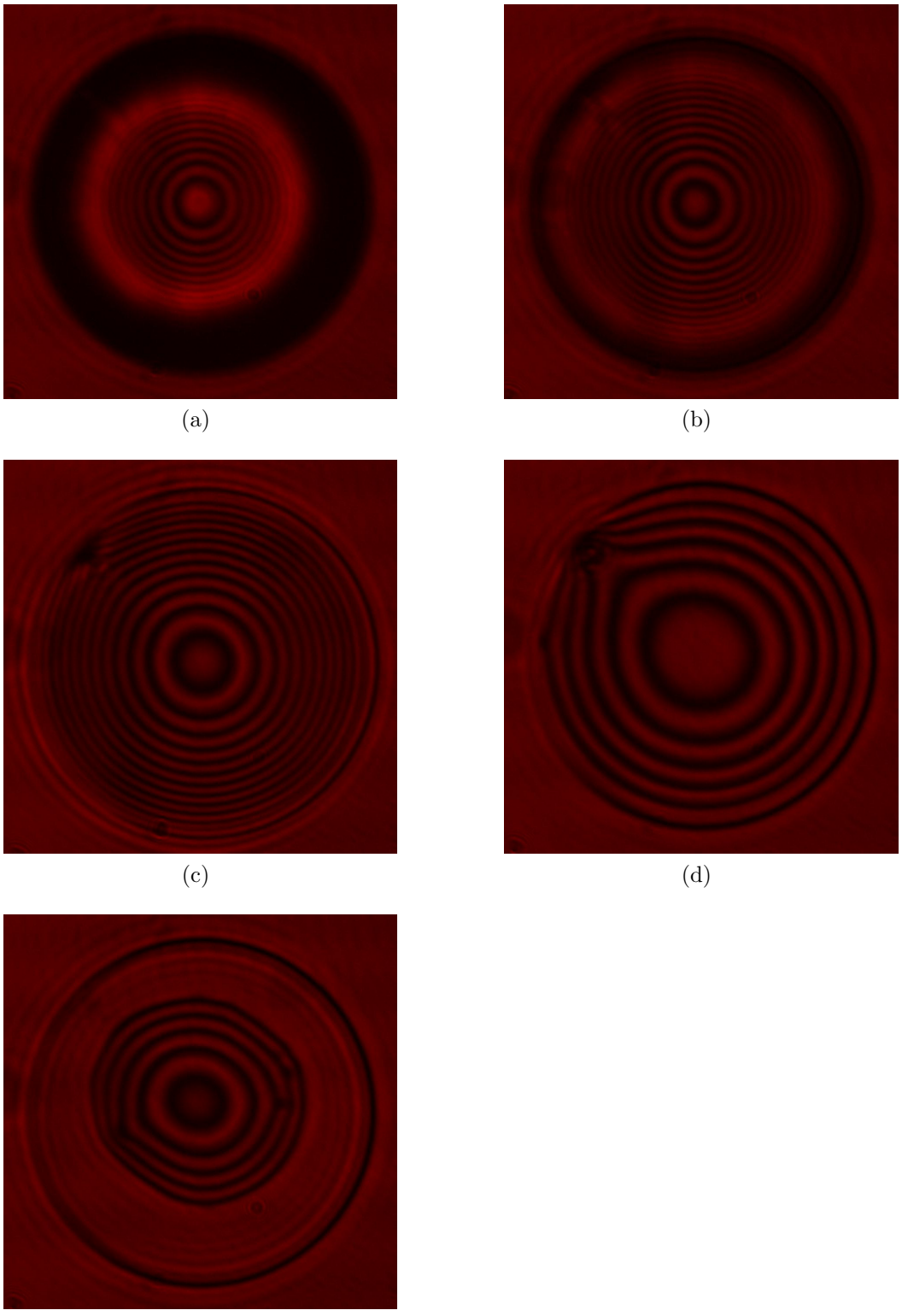

(a) (b) (c) (d) (e)

Figure 5.17: Five frames of the captured interference patterns from a trichlorobenzene droplet. Initial droplet diameter is 300 μm.

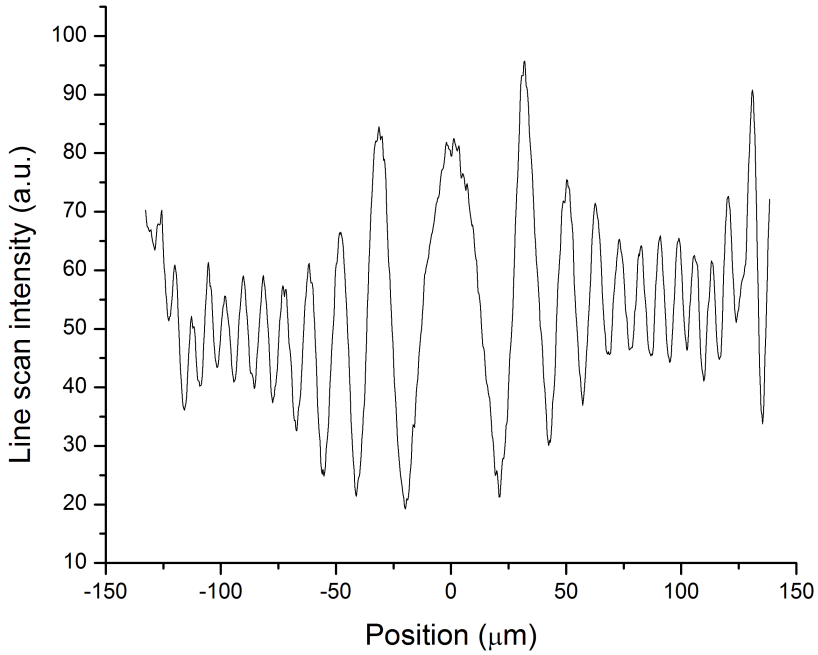

Figure 5.18: Line scan of the ring pattern shown in Figure 5.17c. The positions of peaks and valleys can be found.

well with spherical curves. From the fitting results, the volume of the droplet at each frame can also be calculated, as shown in Figure 5.20.

While trichlorobenzene has a low evaporation rate and the droplet lifetime is long, chlorobenzene is a volatile solvent. A chlorobenzene droplet with an initial diameter of 300 μm dries completely in about three seconds, while trichlorobenzene droplet takes about two minutes. In order to capture enough frames during the droplet lifetime, streampix software package (from Norpix.com) was used, which has a high-frame-rate capability. A minimum interval of about 0.1 second was achieved.

Figure 5.21 shows five frames of the ring pattern from a chlorobenzene droplet. Figure 5.22 is an example of the droplet profile evolution during solvent evaporation. The initial diameter of the chlorobenzene droplet is 300 μm. The five frames of the ring patterns shown in Figure 5.21 were analyzed and their respective height profile were calculated and fitted to spherical curves (solid lines). The time of the five frames

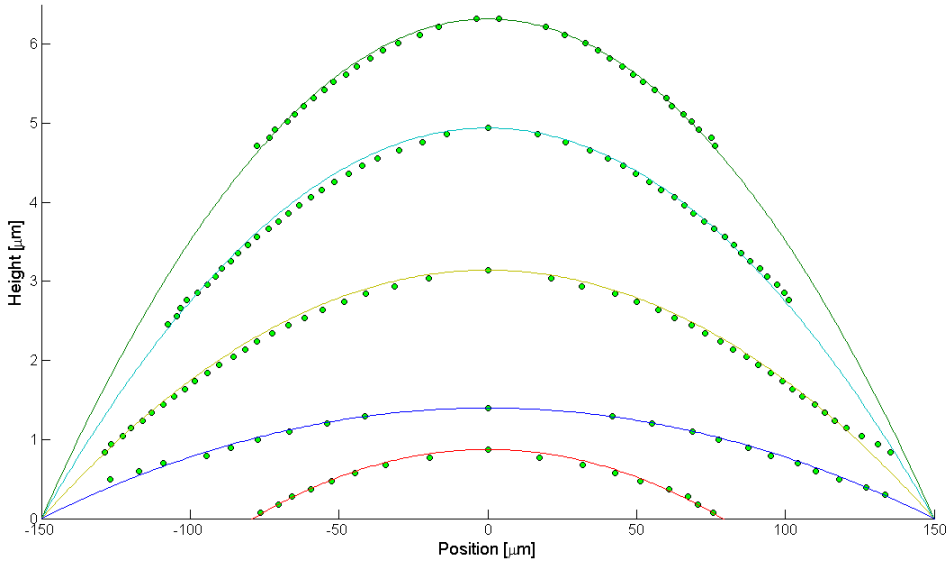

Figure 5.19: Regenerated droplet profiles with spherical curve fitting of a trichlorobenzene droplet.

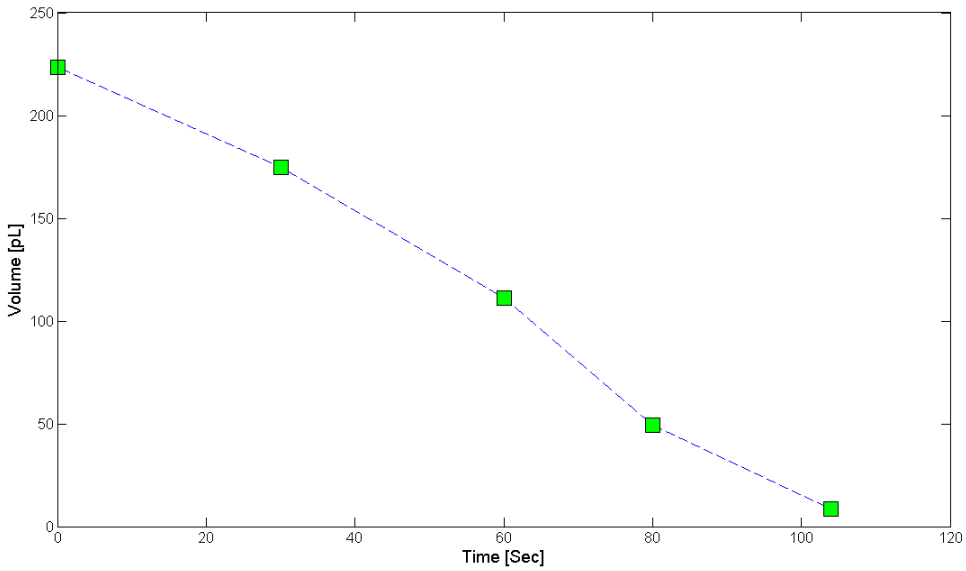

Figure 5.20: The droplet volume vs. time during solvent evaporation of a trichlorobenzene droplet.

are at 0, 92, 284, 474, 760 mSec, with their height profiles shown in the figure from top to bottom, respectively. Notice that in the 5th frame (the bottom curve) the droplet shrank to a smaller size due to solvent evaporation and contact line unpinning. From Figure 5.22 we can see that the data points all fit well with spherical curves. Figure 5.23 shows the volume of the droplet vs. time, calculated from the fitting results of the chlorobenzene droplet (another curve is from a 0.1% PVK in chlorobenzene droplet, to be discussed later).

We now added polymer PVK to the printed droplets. Similar results were found when PVK was added to chlorobenzene at 0.1%. Figure 5.24 shows six frames of the ring patterns captured from a 0.1% PVK in chlorobenzene droplet. The corresponding droplet profiles are shown in Figure 5.25. The frames were captured at time 0, 103, 197, 292, 480 and 781 mSec for curves from top to bottom in Figure 5.25. Notice that the top four profiles follow spherical shapes pretty well and their fitting curves are shown in solid lines. The bottom curve, however, deviates from a spherical shape and no spherical fitting has been applied. The absolute height of the bottom curve is arbitrary as shown in the Figure. The corresponding droplet volume vs. time curve is shown in Figure 5.23 for the five fitted profiles.

Similar results were observed when PVK is added to trichlorobenzene at 1%. Figure 5.26 shows six frames of the ring patterns captured from a 1% PVK in trichlorobenzene droplet. The time stamp for each frame is 0, 1.0, 3.5, 11.4, 15.5 and 17.4 Sec. The corresponding droplet profiles regenerated are shown in Figure 5.27. Notice that the droplet initially follows a spherical shape well, as shown in the top three profiles and their spherical shape fitting curves. With the evaporation of the trichlorobenzene, the droplet shape deviates from the spherical shape, as shown in the bottom three curves. No fitting was applied for the bottom three curves, and their absolute heights remain unknown. The corresponding droplet volume vs. time curve is shown in Figure 5.28 only for the fitted curves.

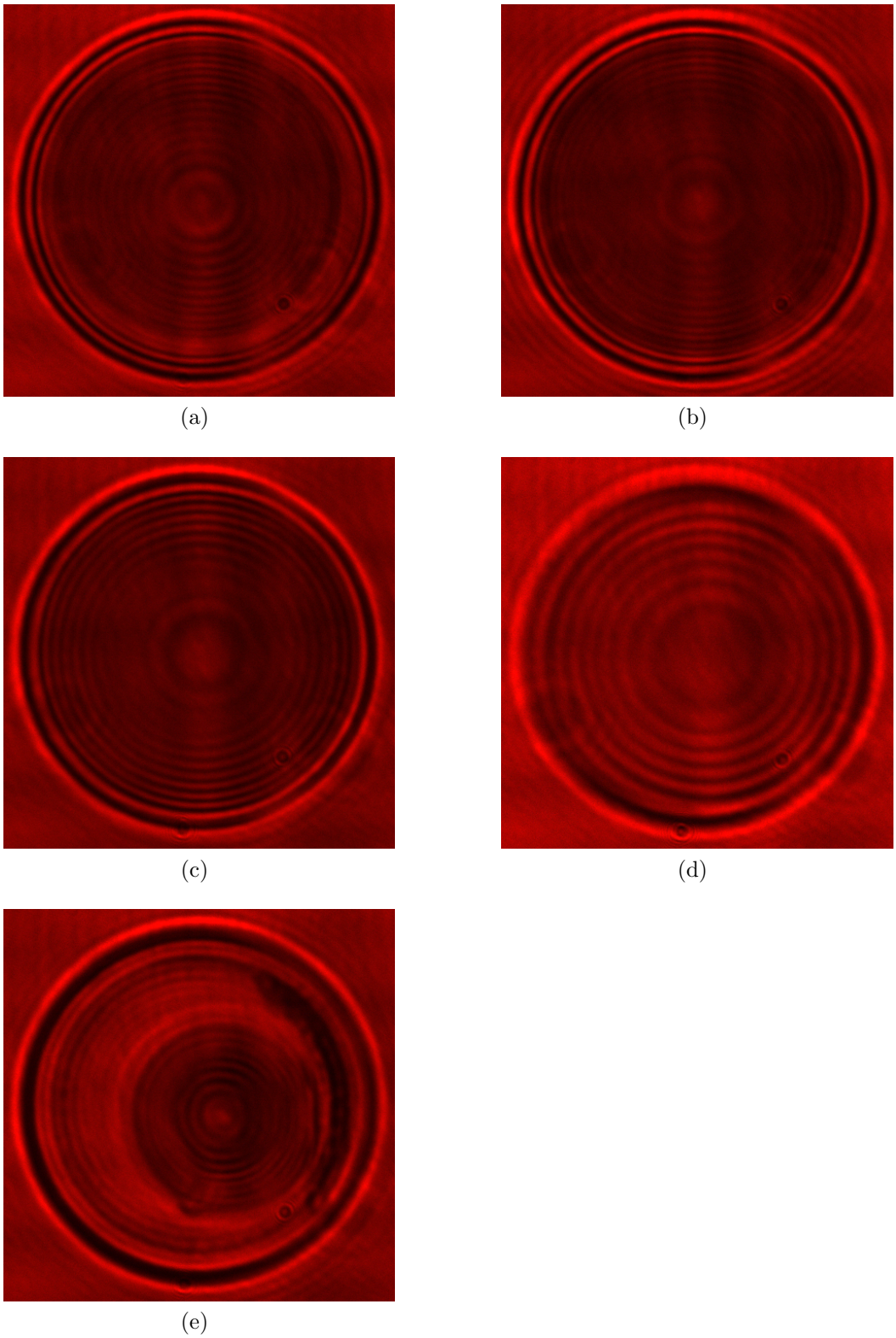

(a) (b) (c) (d) (e)

Figure 5.21: Five frames of the captured interference patterns from a chlorobenzene droplet. Initial droplet diameter is 300 μm.

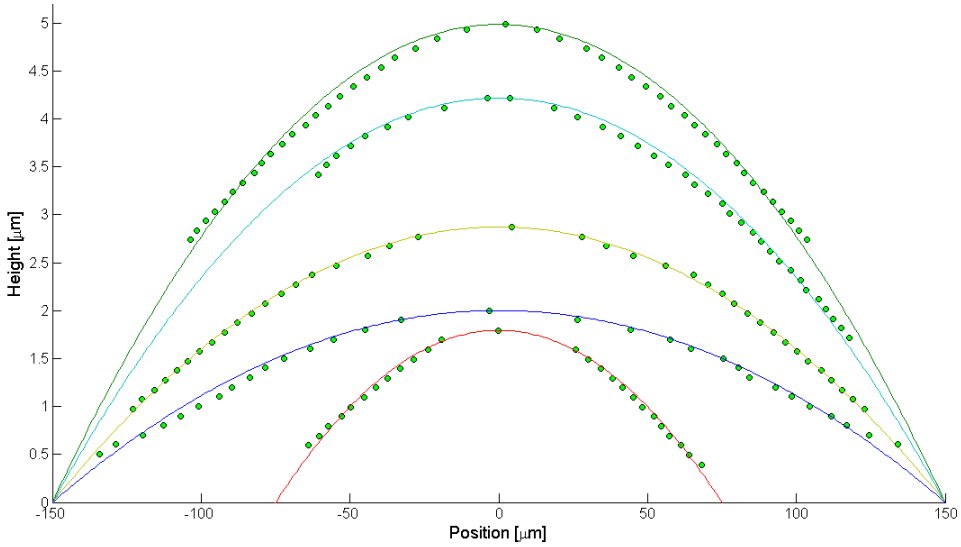

Figure 5.22: Regenerated droplet profiles with spherical curve fitting of a chlorobenzene droplet.

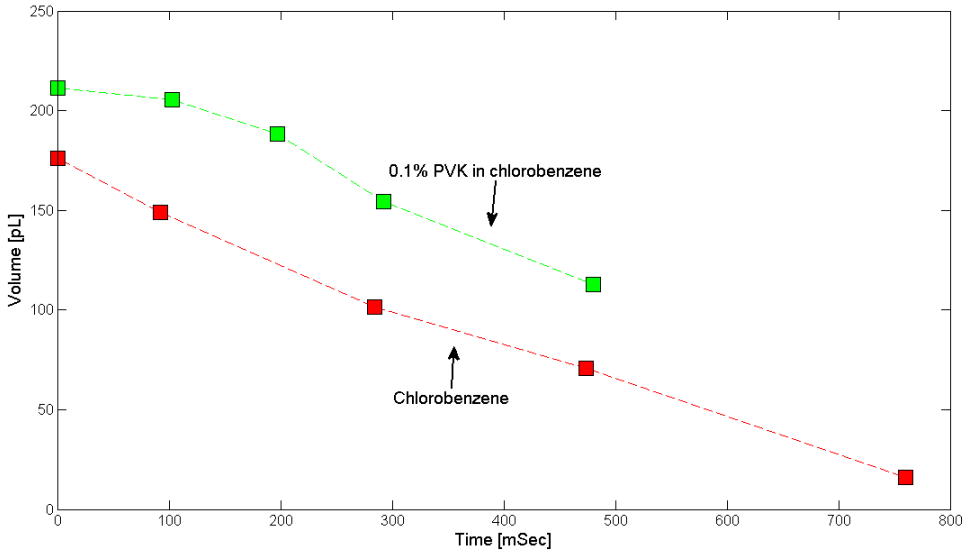

Figure 5.23: The droplet volume vs. time during solvent evaporation of a chlorobenzene droplet, and of a 0.1% PVK in chlorobenzene droplet.

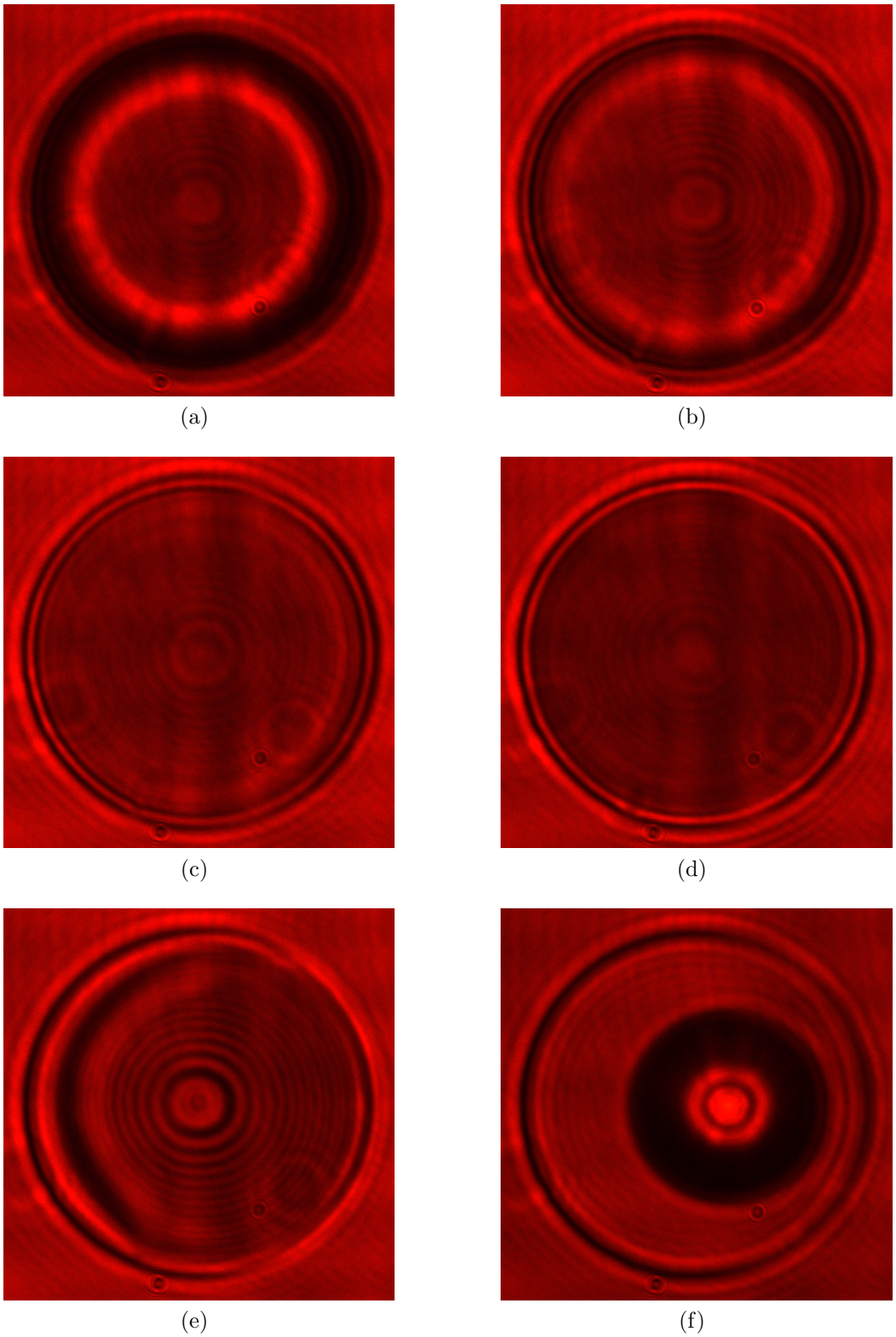

(a) (b) (c) (d) (e) (f)

Figure 5.24: Six frames of the captured interference patterns from a 0.1% PVK in chlorobenzene droplet. Initial droplet diameter is 300 μm.

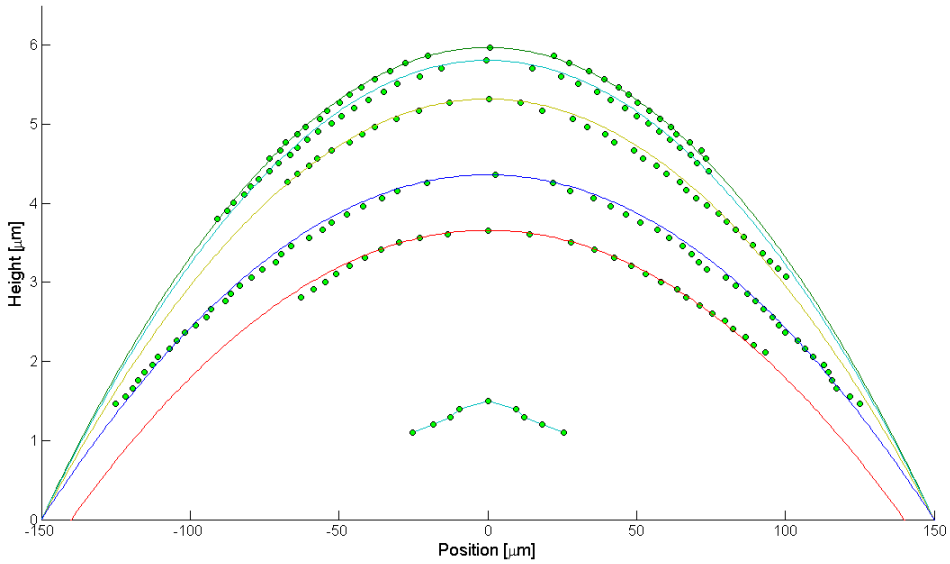

Figure 5.25: Regenerated droplet profiles with spherical curve fitting of a 0.1% PVK in chlorobenzene droplet. The bottom curve deviates from a spherical shape so no fitting was applied and the absolute height of the droplet is unknown.

Following a similar procedure, we have studied the profile evolution of droplets from our regular solution, i.e., 1% PVK in chlorobenzene (ring patterns shown in Figure 5.29, regenerated profile curves shown in Figure 5.30) and 1% PVK in chlorobenzene with FC-4432 surfactant at 0.0045 wt% (Figure 5.31, Figure 5.32). Notice that in both Figure 5.30 and Figure 5.32 only the relative height profiles are shown. For both cases, four different height profiles are shown, each from a different frame. The frame numbers are given in the figures. Each curve is vertically offset from the next one by $1\mu m$ to avoid overlapping. We can see that these profiles do not follow spherical shapes, and thus the fitting process discussed earlier can not be applied and the absolute heights of the droplet remain unknown. Note that in both cases, the regenerated profiles all resemble the shape of a "Mexican hat".

In summary, the droplet profiles for trichlorobenzene or chlorobenzene solvent are spherical in shape, while for 1% PVK in chlorobenzene the profiles resemble the shape of a "Mexican hat". When PVK is added to chlorobenzene solvent at only 0.1% or

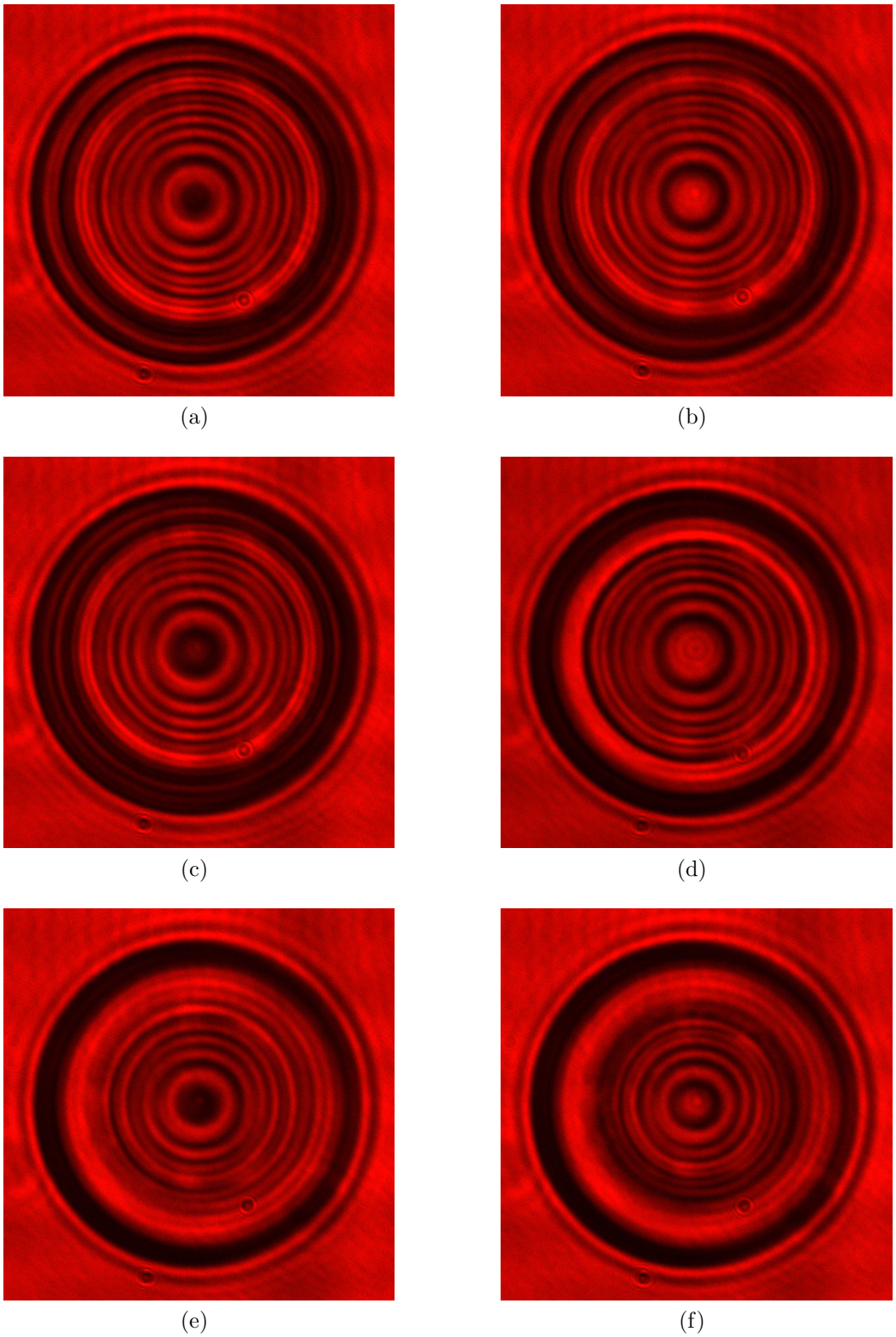

(a) (b) (c) (d) (e) (f)

Figure 5.26: Six frames of the captured interference patterns from a 1% PVK in trichlorobenzene droplet. Droplet diameter is 300 μm.

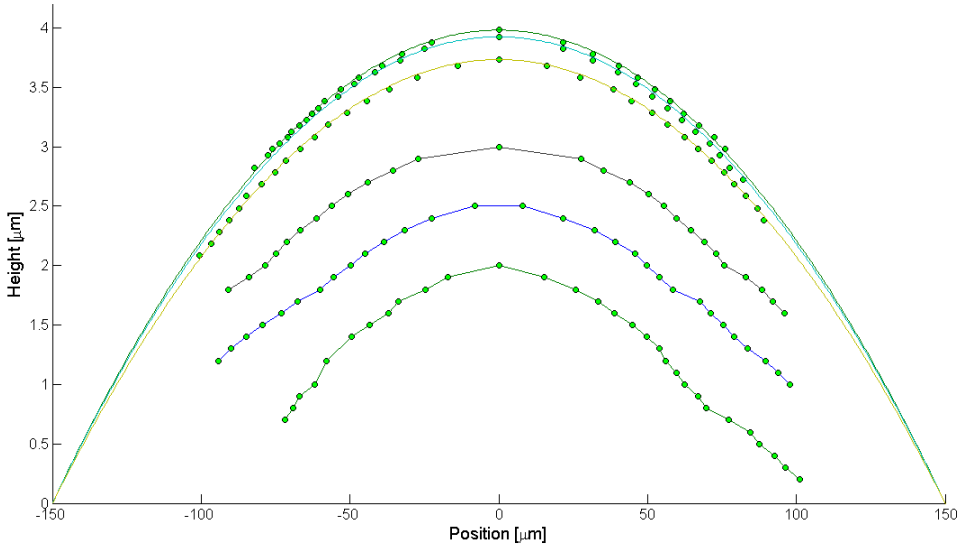

Figure 5.27: Regenerated droplet profiles with spherical curve fitting of a 1% PVK in trichlorobenzene droplet. The bottom three curves have not been fitted and their absolute heights are unknown.

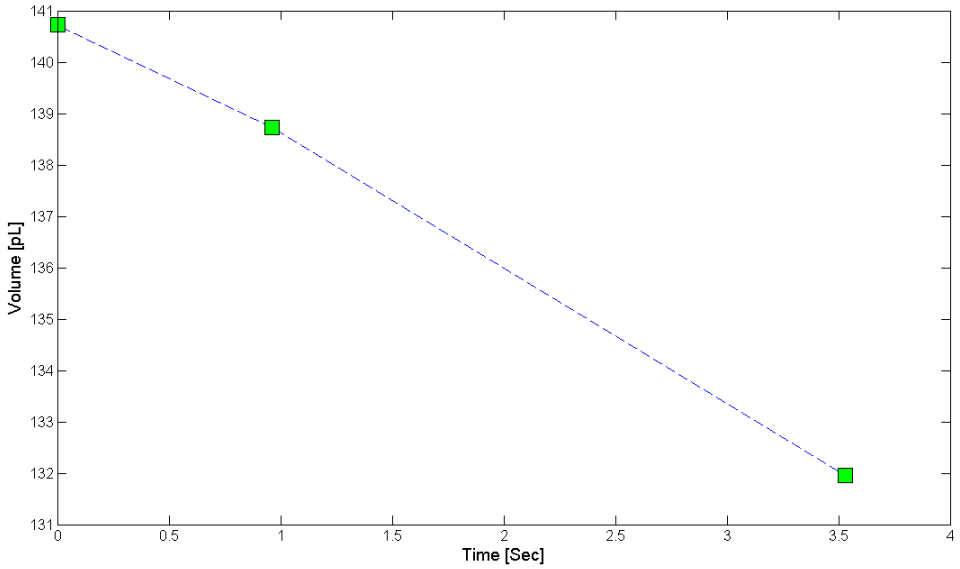

Figure 5.28: The droplet volume vs. time during solvent evaporation of a 1% PVK in trichlorobenzene droplet.

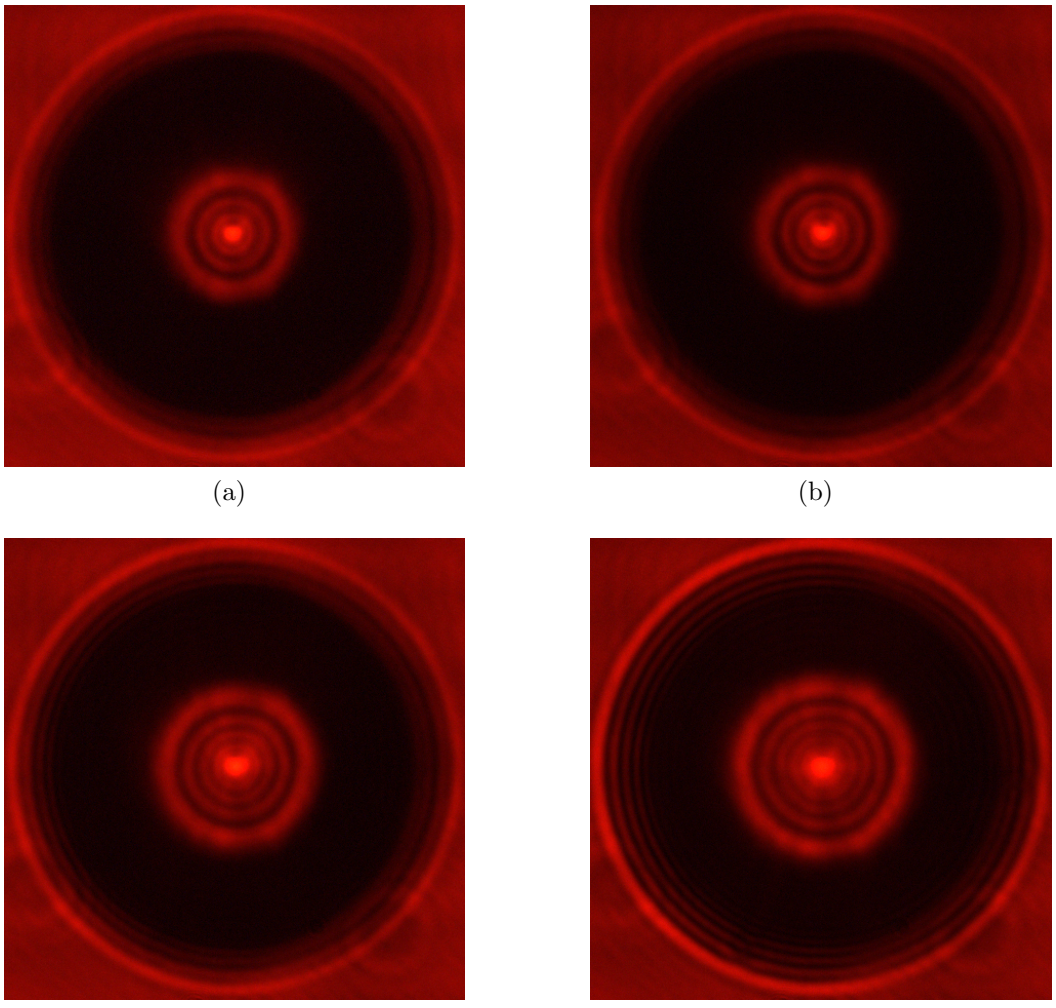

(a) (b)

(c) (d)

Figure 5.29: Four frames of the captured interference patterns from a 1% PVK in chlorobenzene droplet. Initial droplet diameter is 300 μm.

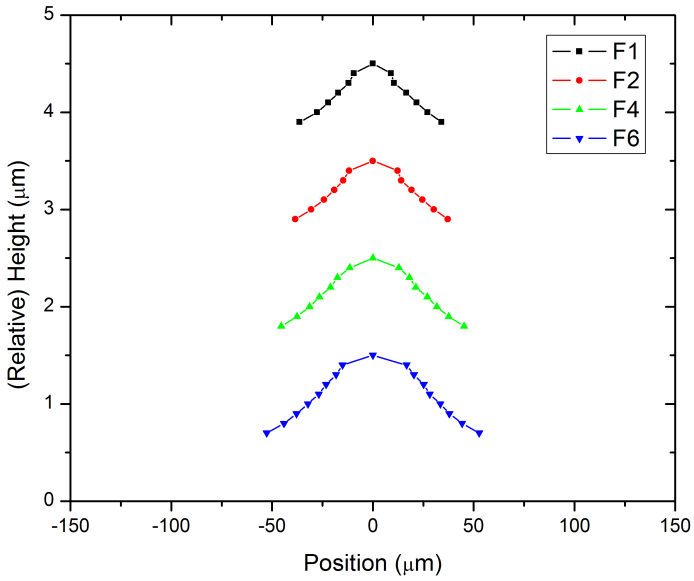

Figure 5.30: Droplet shape evolution: 1% PVK in chlorobenzene. F1, F2, F4 and F6 are frame numbers. The droplet has a diameter of 300 μm. Each curve is vertically offset from the next one by 1 μm.

when 1% PVK is added to trichlorobenzene solvent, the initial droplet profiles are still spherical in shape. However, as the droplet dries out, the droplet profiles starts to deviate from spherical shapes. Two different factors might contribute to the formation of non-spherical-shaped droplets.

First, the non-spherical shape might be a result of long recovery time which caused a non-equilibrium state. Droplets will usually maintain spherical shape controlled by the surface tension in equilibrium state, which is the lowest energy state. In the case of contact line pinning and during solvent evaporation, a higher vapor flux is located at the droplet edge and more solvent is lost at the contact line. As a result, liquid will move outwards to replenish and try to maintain the spherical shape [18]. The results of Figure 5.19 and Figure 5.22 suggest that trichlorobenzene or chlorobenzene solvents are able to move quickly to maintain their spherical shapes. In contrast, the solution of 1% PVK in chlorobenzene (with or without surfactant) has a high viscosity due to

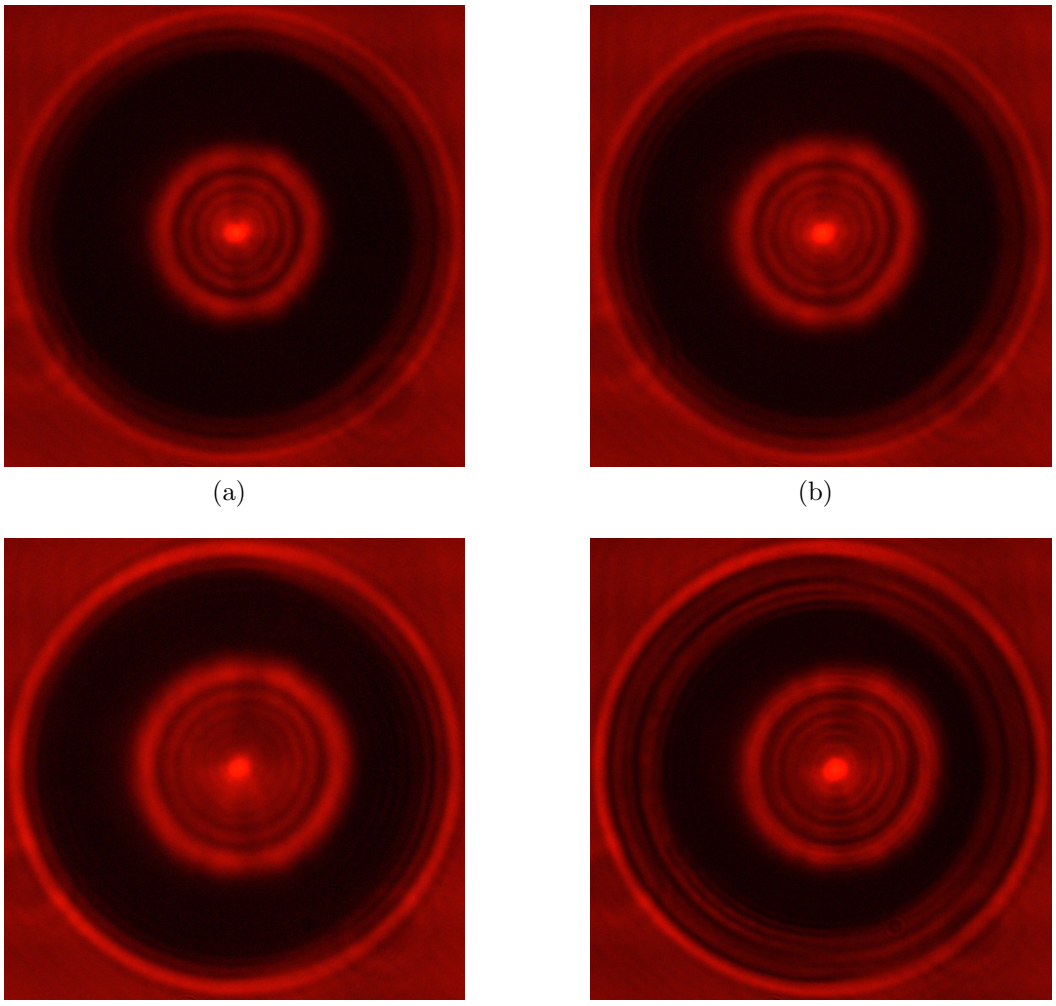

(a) (b)

(c) (d)

Figure 5.31: Four frames of the captured interference patterns from a 1% PVK in chlorobenzene droplet with 0.0045% FC-4432. Initial droplet diameter is 300 μm.

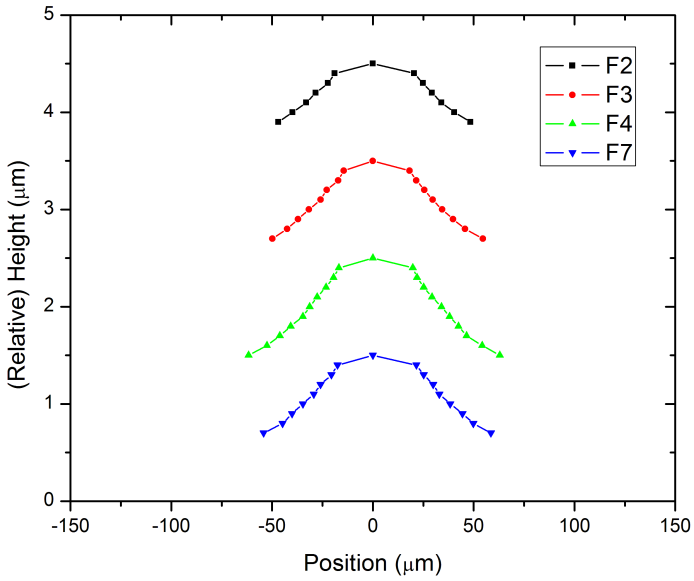

Figure 5.32: Droplet shape evolution: 1% PVK in chlorobenzene with 0.0045% FC-4432. F2, F3, F4 and F7 are frame numbers. The droplet has a diameter of 300 μm. Each curve is vertically offset from the next one by 1 μm.

the polymer chains. As a result the liquid from the center can not replenish the lost close to the contact line and a spherical shape can not be maintained. If we decrease the PVK concentration to 0.1%, the liquid viscosity is low enough to maintain its equilibrium shape at the early stage of the droplet lifetime (Figure 5.25). Late in the drying process, however, when the polymer concentration goes up, the viscosity of the droplet also goes up, preventing the droplet from maintaining its equilibrium state. In another case, where the PVK concentration is kept at 1% PVK while the solvent is replaced by trichlorobenzene, spherical shapes are again maintained at the early stage of drying, due to the low evaporation rate of the solvent, as shown in Figure 5.27. As the drying process proceeds, the polymer concentration also goes up, which leads to a non-spherical-shaped profiles.

Second, a polymer-rich crust layer might contributed to the formation of a "Mexican hat" profile. Similar phenomena were reported for a drying polymer solution

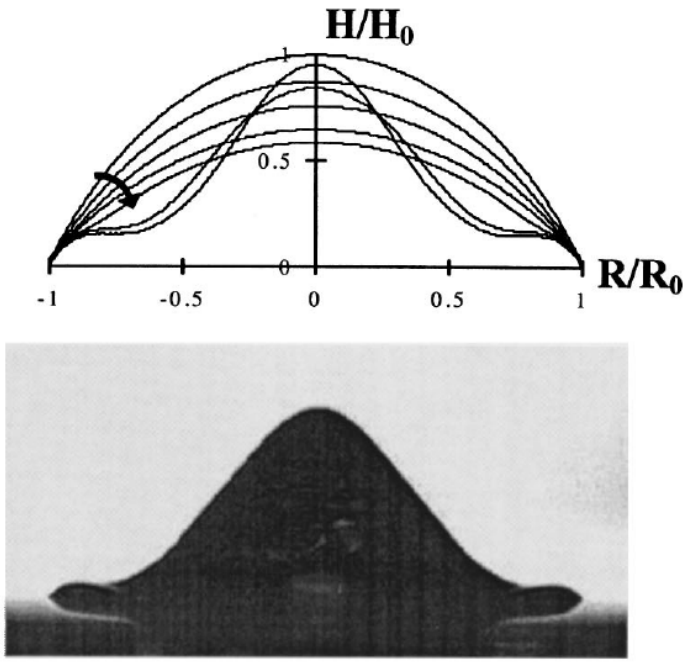

Figure 5.33: Top: Evolution of droplet profiles at different times during drying. Bottom: Side view of the drop with a typical "Mexican hat" shape. From Ref. [52].

droplet, as shown in Figure 5.33 [22, 52]. The occurrence of the "Mexican hat" shape can be explained in the following way [22, 24, 52]: due to the quick lost of solvent in the outer layer during drying, polymer accumulate, especially in the outer layer of the droplet. Thus a skin layer is formed, although it does not block the evaporation. This skin layer is glassy and will deform as the droplet volume decreases, leading to the formation of a "Mexican hat" shape in some unstable case. In the case of 0.1% PVK in chlorobenzene (Figure 5.25), the droplet follows a spherical shape pretty well until late in the drying process, which can be attributed to its low polymer concentration. While for 1% PVK in trichlorobenzene (Figure 5.27), the droplet starts to deviate from the spherical shape also late in the drying process, since the polymer accumulation is depressed due to the low evaporation rate of trichlorobenzene.

The only difference between Figure 5.30 and Figure 5.32 is the use of FC-4432 surfactant. No significant difference can be noticed from the profile curves shown on Figure 5.30 and Figure 5.32. So we are unable to relate the droplet profile evolution

to the effect of surfactant on the thickness uniformity of the final deposited films. Since many other factors can contribute to the complexity of the droplet drying process, such as non-uniform evaporation, surface tension driven flow (Marangoni flow), convection within the droplet, and redistribution of solutes, a more detailed study is required to understand the exact effect of the surfactant on the dried film profile. Our findings presented here suggest that the droplet is not in its equilibrium state and this issue needs to be considered when performing such a study.

5.6 Summary

In summary, we have shown in this chapter that by the co-solvent or the surfactant approaches, it is possible to flatten the wet-deposited PVK films, especially in the center part of the pixel area. Coffee rings are still observed on the edge even after our optimization, but they only occupy small regions of the total area. The use of L62 surfactant severely degrades OLED performance, while the use of a more effective surfactant, the FC-4432 from 3M, flattens the PVK profile at very low concentrations. The use of the FC-4432 is found out to be safe for device applications. A further treatment of the PVK film under solvent vapor annealing resulted in a very smooth profile, however, the profile curves up as a side effect. As a conclusion, it is very difficult to achieve flat and smooth films from wet printing, compared to the film quality of a spin-coated film. In the next chapter, a dry printing method will be introduced, which has superior film uniformity compared to films deposited from wet processing methods, such as the LAMP method or ink-jet printing.

Chapter 6

Transfer Printing

6.1 Overview

Both ink-jet printing and our LAMP method are based on solution processing. As discussed in Chapter 5, one problem related to wet processing techniques is that the printed films are usually non-uniform. In order to achieve a flat profile, special attention is given to the modification of ink formulation, substrate structure and surface energy and evaporation conditions, etc. Even so, the optimized films are usually inferior in uniformity to films prepared by dry printing methods. If the film uniformity can't be solved completely in a low-cost manner, then in some high profile application, it may become necessary to fabricate OLED displays by a dry printing method. In this chapter a transfer printing method will be introduced, which can print organic films with very uniform thickness.

The information in this chapter was presented in Ref. [37–39].

6.2 Concept of Transfer Printing

The concept of transfer printing utilized in this work is illustrated in Figure 6.1: (a) A thin polydimethyl siloxane (PDMS) layer is spin-coated on a hard substrate as a soft backing layer. Polymers to be patterned are formed as a thin layer on top of the

PDMS layer, usually by spin-coating. A hard stamp is fabricated by conventional photolithography patterning followed by dry etching. (b) The hard stamp is pressed against the polymer film at elevated temperature to break the polymer film at its feature edges when the PDMS deforms. When the stamp is withdrawn, its raised features pick up the corresponding portions of the polymer layer. As a result, two patterned layers are formed, one at the stamp surface, another at the PDMS side. These two patterns are complementary to each other and can be referred to as "positive pattern" and "negative pattern", respectively.[1] Either of them can be further transferred onto a device plate for usage. In the first case shown in (c) the pattern picked up by the stamp is used, and by another transfer printing step is deposited onto a target substrate. Similarly, the pattern left on the PDMS side can also be utilized and deposited onto a target substrate, as shown in (d). This patterning method was first introduced by Kong et al. [43] for the printing of non-active polymer films such as polymethyl methacrylate (PMMA).

6.3 Transfer Printing

Based on the work of Kong et al. [43], we developed a similar method for active light-emitting polymer patterning for full-color OLED display applications, which we refer to as "Transfer Printing".

Figure 6.2 presents the procedures of our transfer printing patterning technique. The process begins with the fabrication of a hard stamp [Figure 6.2a], where the raised features correspond to the final regions without the polymer on the final device plate. A silicon wafer is used for the hard stamp, and conventional lithography and dry etching are used to make it. In this work, rectangular patterns of two dimensions ($12\mu m \times 40\mu m, 24\mu m \times 80\mu m$) are etched into the stamp to a depth of ∼700 nm.

[1] In our experiments, one of the two patterns always contains an array of pixels, in squares, rectangles or circular shapes, and is referred to as the "positive pattern". The complementary pattern formed is a continuous film with openings, and is referred to as the "negative pattern".

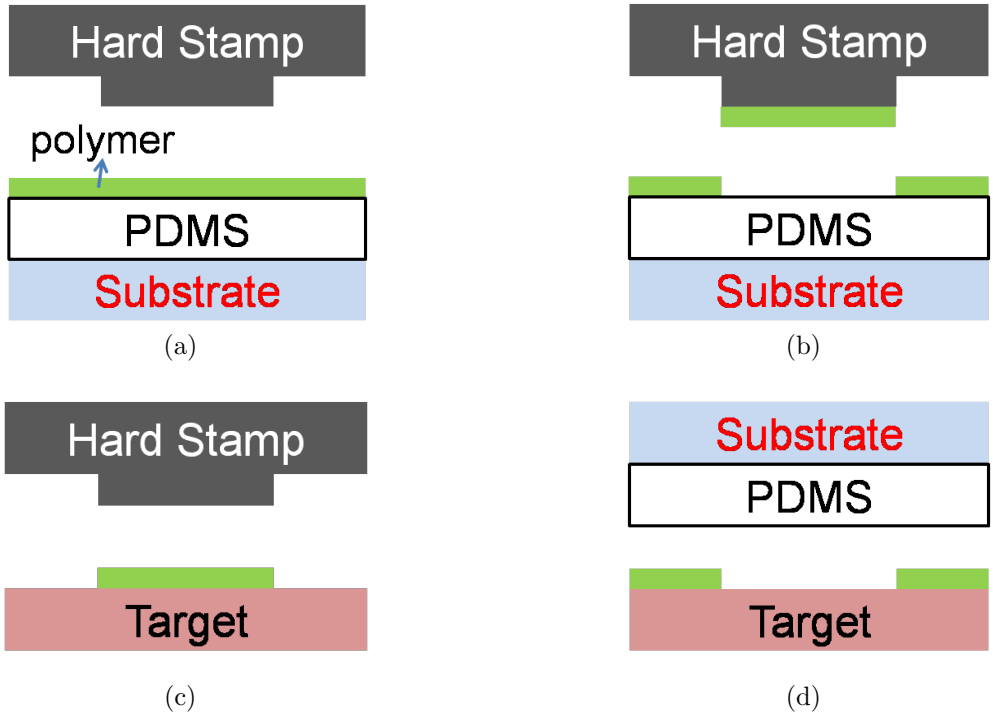

Figure 6.1: Basic patterning principle used in the transfer printing process. (a) Polymer film to be patterned is formed on top of a soft PDMS layer. (b) The hard stamp is pressed against the polymer film at elevated temperature to break the polymer film at protrusion edges. When the stamp is withdrawn, its raised features pick up the corresponding portions of the polymer layer. As a result, two patterned layers are formed, one on the stamp surface, another on the PDMS. (c) The polymer pattern on the stamp side in step (b) is transfer printed onto a target substrate. (d) The polymer pattern left on the PDMS side in step (b) is transfer printed onto a target substrate.

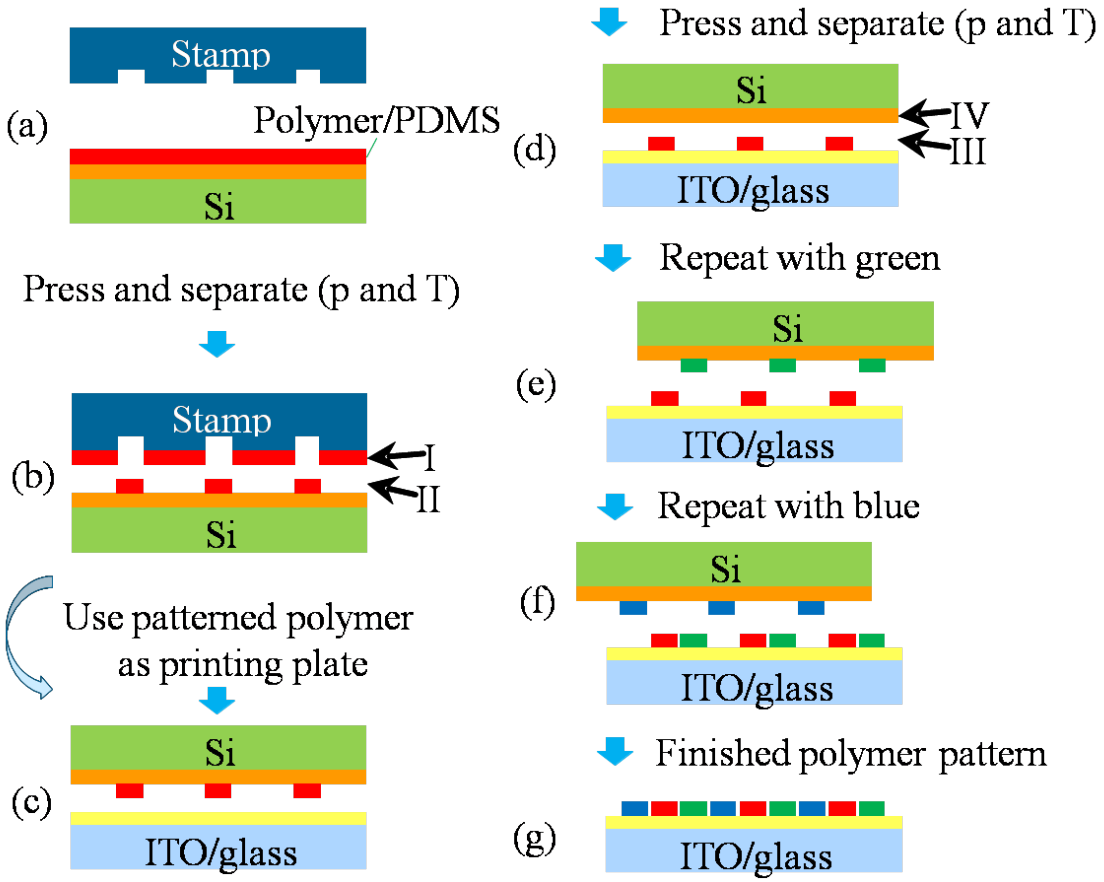

Figure 6.2: Schematic diagram of the transfer printing method for full-color OLED patterning.

A second flat plate, also silicon for convenience, is coated with a PDMS layer and used as a backing layer for the active polymer layer to be patterned. The PDMS is spin-coated from a PDMS prepolymer which is a mixture of Sylgard 184 and its hardener (from Dow Corning) dissolved into cyclohexane solvent (in some early results, toluene was used). The ratio is 10 grams of the Sylgard 184 and 1 gram of the hardener in 100 ml cyclohexane. PDMS is spin-coated onto a silicon wafer at 2500 rpm with a ramp of 1000 rpm/s for 40 seconds. The PDMS prepolymer solution is syringe-filtered with 0.1 μm filter before use. The PDMS film is then baked at $150°C$ for 2 hour on a hotplate in air for cross-linking. The PDMS film is about 1.2 μm in thickness after baking.

The control of surface energies for transfer printing is critical. The PDMS surface is hydrophobic as prepared and it is not able to be coated by spin-coating with a polar solution (such as our PVK+PBD+dye in chlorobenzene solution). A short oxygen plasma treatment of the PDMS surface, however, will render it hydrophilic so that spin-coating of the light-emitting polymer mixture is possible. In our transfer printing experiments, the oxygen plasma takes about 5–15 seconds and is done in a reactive ion etcher (TePla M4L) at 80 watts and 250 mTorr.

For the active light-emitting organic layer, a mixture of PVK + PBD + dye is used, with its composition given in Section 3.2. Three different layers are prepared for each color, i.e., PVK + PBD + nile red for red, PVK + PBD + C6 for green and PVK + PBD + C47 for blue. Chlorobenzene is used as the solvent for the mixture (100 mg of PVK in 7.5 ml of chlorobenzene). The cosolution is spin-coated onto the PDMS-coated silicon substrate. A spin coating recipe of 2000 rpm for 50 seconds results in a film thickness of ∼70–90 nm.

The stamp is then pressed against the polymer film at elevated temperature of $50-150°C$ for 2–6 minutes at a pressure of 50–400 psi [Figure 6.2b]. For this step, we use a commercial nano-imprinter (Nanonex NX-2000) since it is readily available and

it can control both the pressure and temperature. Another advantage related to the choice of the nano-imprinter over other options (such as the use of weight to apply the pressure) is that in the nano-imprinter the pressure is applied through pressurized nitrogen gas so the pressure is uniform over the whole stamp area. Under pressure, the PDMS layer deforms and a large stress field is concentrated at the stamp feature edge (will be discussed in more detail in Section 6.5). As a result the polymer film breaks at the stamp feature edges. After the system cools down to $50°C$ the pressure is released and the stamp is carefully separated from the substrate with the help of a razor blade. Upon separation, polymer film in contact with the raised regions of the silicon stamp is removed by the stamp, while the rest of the polymer film is left on the PDMS surface. The successful transfer of the polymer layer to the stamp surface (where contact is achieved) is a direct result of the interface adhesion difference. That is, the adhesion between the polymer/PDMS is lower than that of polymer/stamp (clean silicon) since the PDMS surface energy state is believed to be able to revert back shortly after to its original state before the oxygen plasma treatment [43].

It is possible to use either of the patterned layers (the stamp or PDMS/Si substrate) for further printing, as shown in Figure 6.1c and Figure 6.1d. If the stamp side pattern is to be utilized, the stamp surface needs to be pre-treated beforehand to lower the stamp surface energy, so that the polymer on the protrusions of the stamp surface can be eventually transferred to a target device substrate (Figure 6.1c). However, the stamp surface energy still needs to be higher than the surface energy of the PDMS layer in order for the stamp to pick up the polymer layer in the first step. Careful tuning of the surface treatment is required for good transfer yield for both transfer steps. Kong et al. use a sequential treatment of the stamp with two different silanes, first with phenethyl-methyl-di-chlorosilane followed by n-octadecyl-methyl-di-chlorosilane [43]. In our work, we found out that a single silane treatment of the stamp surface in 20mM of Phenethylmethyldichlorosilane (PEDS) in anhydrous

dodecane for 10 minutes is sufficient to result in good transfer yield.

In this thesis, the majority of the experiments use the polymer pattern left on the PDMS surface (as shown in Figure 6.1d and also in Figure 6.2c), mainly due to two considerations. The first reason is that larger difference in surface energy is preferred to achieve a high transfer yield. The difference between the hydrophobic PDMS surface and the usually hydrophilic stamp or device substrate is large. On the other hand, if the stamp side pattern is used, the surface energy difference seen in each of the two transfer steps will be significantly smaller. The second consideration is that the soft PDMS layer allows a conformal contact to be more easily realized between the patterned polymer layer and the device substrate [Figure 6.2c], if any non-idealities (non-planar substrate, particles, etc) are present. In contrast, it is difficult to achieve intimate contact between two hard-hard substrates if the stamp side pattern is used for the second transfer.

As shown in Figure 6.2c, the patterned polymer layer left on the PDMS side is used for the next transfer printing step. For the fabrication of OLED devices, an ITO-coated glass substrate is used as the target plate. However, a silicon wafer and a glass substrate (without an ITO coating) have also been used throughout the thesis when electrical characterization of the device was not performed. By a second press and separate step (Figure 6.2d), the patterned polymer layer is transferred onto the target substrate. For the three different substrates used (acting as the device plate), an oxygen plasma treatment is performed before the transfer printing process to achieve a higher surface energy and thus a more successful transfer of the polymer layer. No significant differences are observed for the different substrates. For convenience, the same printing condition (temperature and pressure setting) is applied for the two transfer steps (Figure 6.2 b and d). Repeating steps (a)-(d) twice for the second (Figure 6.2e) and third (Figure 6.2f) color enables a R, G, B array required for a full-color OLED display to be successfully patterned. The finished R, G, B pattern

is illustrated in Figure 6.2g.

Multi-layer registration is required for the patterning of the second and third color on the same device plate. In our experiments, since the Nanonex nano-imprinter lacks alignment ability, multi-layer registration is achieved through the help of a photolithography mask aligner (Karl Suss MA6). An illustration of our work-around is shown is Figure 6.3. Whenever multi-layer patterning is done, only glass or ITO-glass substrate is used as the target substrate, since the ability to see through the substrate is required for the optical alignment. The transparent target wafer is held in the position used for a regular photo-mask on the aligner, while the PDMS/Si plate (with polymer pattern) is held in the substrate holder of the mask aligner. A magnetic stainless steel sheet (type 430 stainless steel sheet, 0.025" thick, from McMaster-Carr), with its dimension slightly smaller than the PDMS/Si substrate, is attached to the back of PDMS/Si substrate by wax. After the alignment is achieved on the contact mask aligner, and the glass target substrate and the PDMS/Si substrate are brought into contact. A small magnet (ultra-high-pull neodymium disc magnet, 3/4" diameter, 0.1" thick, 5.7 pull lbs, from McMaster-Carr) is then attached to the top of the glass target wafer, which will hold the two wafers fixed in position. At this moment, the vacuum holding the two wafers onto the mask aligner is removed (by manually disconnecting the vacuum hose leading to the mask holder) and the two wafers together with the magnet and stainless steel sheet are released. The stack is then transferred into the nano-imprinter for the actual transfer printing. Due to the design limitations of the nano-imprinter, the magnet needs to be carefully removed before the pressure can be applied, and a small relative movement between the two plates can easily occur. As a result, misalignment is often observed.

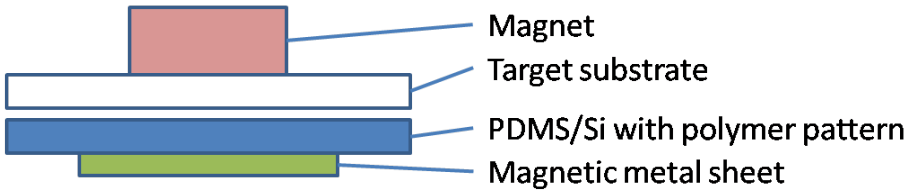

Figure 6.3: Schematic diagram of the work-around used for alignment purposes. The alignment is done with a mask aligner with the transparent target substrate acting as the mask. When alignment is done, a small magnet is attached to the top of the stack which will hold the two wafers together. The whole stack is then transferred into the nano-imprinter for the actual transfer printing process.

6.4 Transfer Printing PMMA

As a first step, PMMA polymer layers are patterned as a demonstration of the transfer printing method. PMMA powder is purchased from Aldrich with a molecular weight of $M_w = 15,000 g/mole$ and a glass transition temperature of $T_g = 105°C$. PMMA solutions are formed with 4 wt% in chlorobenzene. A spin recipe of 4,000 rpm for 40 seconds on silicon substrate results in a thin PMMA layer of about 100 nm in thickness. The silicon stamp has circular-shape protrusions with a diameter of $320\mu m$. The silicon stamp is immersed into a 20mM PEDS in anhydrous dodecane solution for 10 minutes for silane treatment in a glove box. After the first transfer printing step, patterns are formed on the stamp and on the PDMS. By further printing steps, both of the two patterns are separately deposited onto a silicon substrate, acting as the target substrate as a demonstration. The final PMMA patterns are shown in Figure 6.4, where Figure 6.4a corresponds to the "positive pattern" printed from the stamp side, and Figure 6.4b corresponds to the "negative pattern" printed from the PDMS side. The size of the circular pads in both images are $320\mu m$, which is defined by the features of the stamp. Surface profile scans on both the positive and negative patterns of PMMA films are given in Figure 6.5, which clearly reveals the fact that the two patterns are complementary to each other. A broad range of printing conditions can be used that results in good patterning and transfer yield. For the results shown

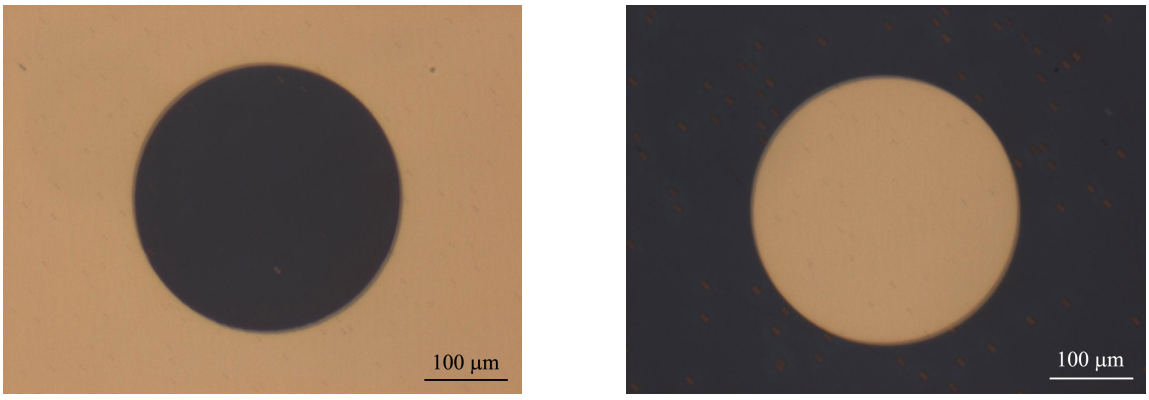

(a) (b)

Figure 6.4: PMMA patterns printed onto a silicon substrate after the second transfer step. The circular pads have a diameter of $320\mu m$, PMMA is shown in dark color and silicon is in light color. (a) PMMA film printed from the stamp surface. (b) PMMA film printed from the PDMS stamp side.

here a printing temperature of 110°C and a pressure of 450 psi with a holding period of 6 minutes is used.

As discussed earlier, if the pattern left on the stamp side from the first transfer step is utilized for the second transfer step, appropriate surface energy treatment of the stamp surface is required for a complete transfer. This surface energy reduction of the stamp surface can be achieved by silane treatment. If no special treatment is performed on the stamp surface, only partial transfer will occur due to surface energy similarity between the stamp and the target substrate. Figure 6.6 shows two examples of partially-transferred PMMA positive patterns from an untreated stamp. Instead of forming complete circular pads such as the one shown in Figure 6.4a, PMMA films form some arbitrary-shaped patterns due to a incomplete transfer.

As another demonstration of the transfer printing method, PMMA patterns with different features are formed and are shown in Figure 6.7. Four different features are demonstrated, i.e., arrays of circles of diameter $12\mu m$ (first row) and $24\mu m$ (second row) and arrays of rectangles of dimensions $12\mu m \times 40\mu m$ (third row) and $24\mu m \times 80\mu m$ (fourth row). Each row contains three images, where the first im-

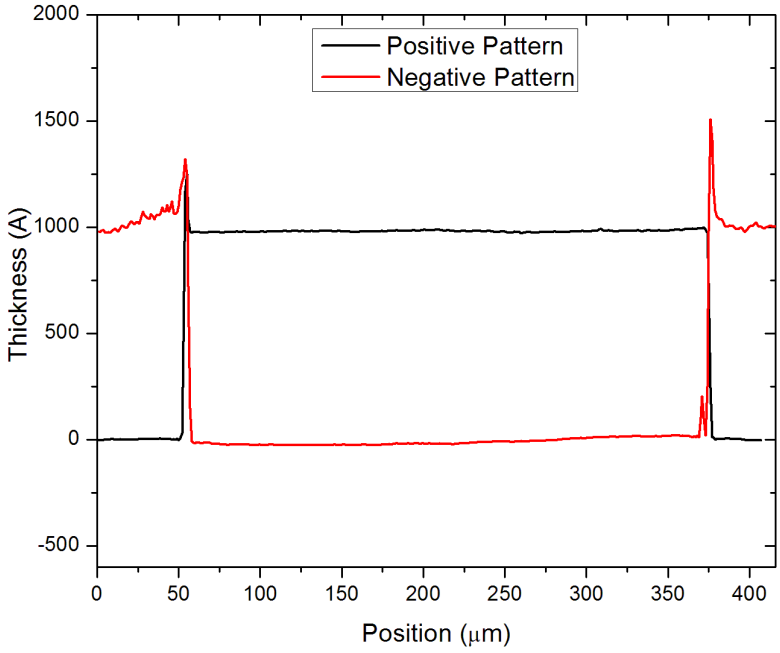

Figure 6.5: Surface profile scans of the two PMMA patterns shown in Figure 6.4, where positive pattern corresponds to Figure 6.4a and negative pattern corresponds to Figure 6.4b.

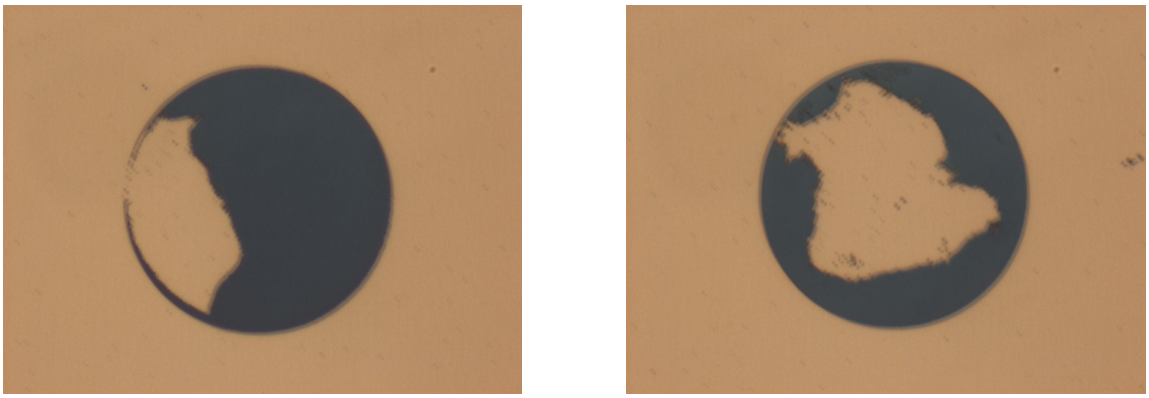

(a) (b)

Figure 6.6: Typical results of "bad-quality" patterns as a result of partial transfer. PMMA is shown in dark color and silicon substrate is in light color. The partial transfer of the PMMA film is caused by a surface energy similarity between the silicon stamp (without any silane-treatment) and the silicon substrate. The circular pads have a diameter of $320\mu m$.

age is the pattern formed on the stamp (negative pattern) and the second image is the pattern formed on PDMS layer and the third image is the second pattern after being transferred onto a silicon wafer.

6.5 Finite Element Analysis

Finite element analysis of a silicon stamp pressing onto a polymer-coated PDMS layer is performed with ANSYS. All layers are modeled as linear, isotropic, and elastic materials. PMMA is used as the polymer layer for demonstration. The stress distribution when other polymers are used instead of PMMA would be similar. The Young's modulus and Poisson's ratio for silicon, PMMA and PDMS are summarized in Table 6.1. The simulation results are shown in Figure 6.8. The sample geometry used is shown in Figure 6.8a, where the PMMA layer is 100 nm thick, the PDMS is 500 nm thick. The top edge of the silicon stamp is 2 μm in width. The silicon stamp protrusion is 300 nm in depth and 1 μm in width (so 50 % of the total silicon surface). The bottom edge of the PDMS is fixed to have no displacement. A normal pressure of 0.15 MPa (21 psi) is applied to the top edge of the silicon stamp. The mesh plot used for the simulation is shown in Figure 6.8b. The calculated deformed shape with the von Mises stress distribution is shown in Figure 6.8c. Clearly, the distribution of stresses is not uniform within the PMMA layer, with large stresses localized along the edges of the silicon stamp protrusions. Figure 6.8d shows a magnification of the region with localized stresses. The maximum stress is found to be linearly proportional to the applied pressure on the top edge of the stamp. When the localized stress exceeds the yield stress of the polymer layer, a local rupture of the polymer layer will occur.[2] If we replace the PMMA with another polymer (with different Young's modulus and Poisson's ratio), our simulation gives similar results.

[2]For simplicity in our discussion, we assume that polymer yield will lead to rupture. In fact, polymer yield is different than rupture and different polymers may rupture in different ways.

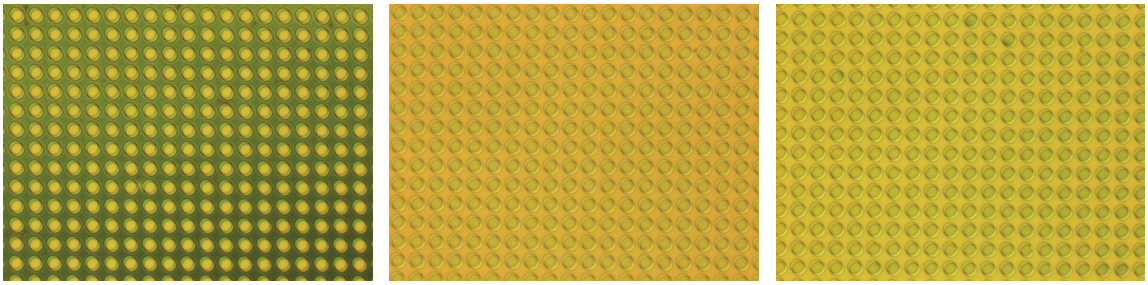

(a) on stamp, Dia. $12\mu m$ (b) on PDMS, Dia. $12\mu m$ (c) on silicon, Dia. $12\mu m$

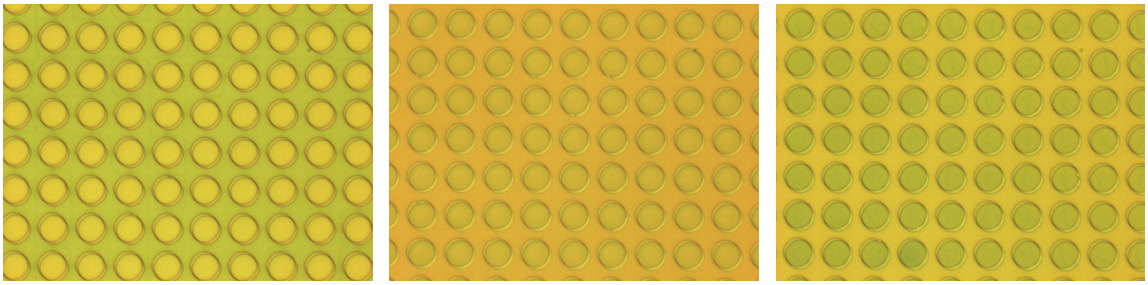

(d) on stamp, Dia. $24\mu m$ (e) on PDMS, Dia. $24\mu m$ (f) on silicon, Dia. $24\mu m$

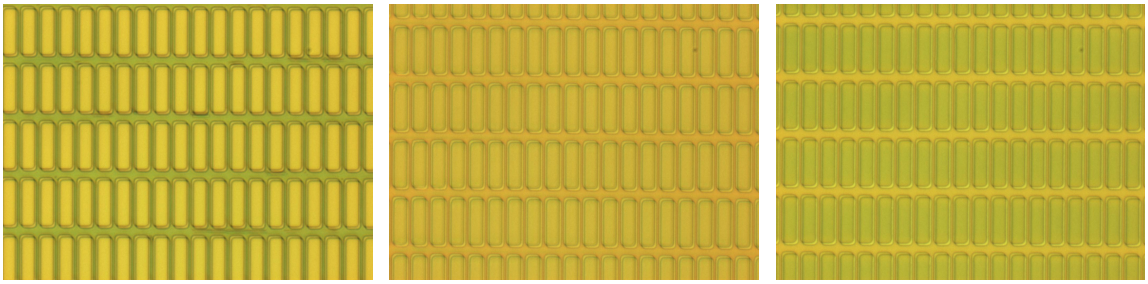

(g) on stamp, $12\mu m \times 40\mu m$ (h) on PDMS, $12\mu m \times 40\mu m$ (i) on silicon, $12\mu m \times 40\mu m$

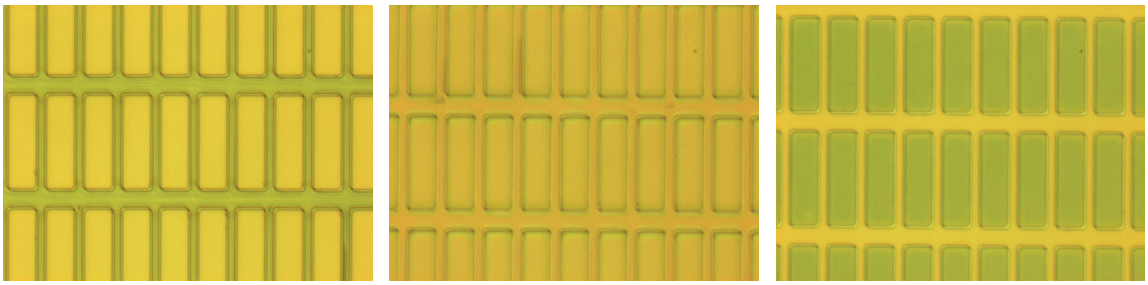

(j) on stamp, $24\mu m \times 80\mu m$ (k) on PDMS, $24\mu m \times 80\mu m$ (l) on silicon, $24\mu m \times 80\mu m$

Figure 6.7: Various PMMA patterns formed by transfer printing. Three images in each row belong to a series where the first image is the pattern formed on the stamp (negative pattern) and the second image is the pattern formed on the PDMS layer (positive) and the third image is the second pattern transferred from PDMS onto a silicon wafer (positive). Different rows of images have different features (shape or dimension).

Table 6.1: Material parameters used in finite element analysis [10, 43]

Material	Young's modulus	Poisson's ratio
Silicon	181 GPa	0.3
PMMA	900 MPa	0.499
PDMS	3 MPa	0.48

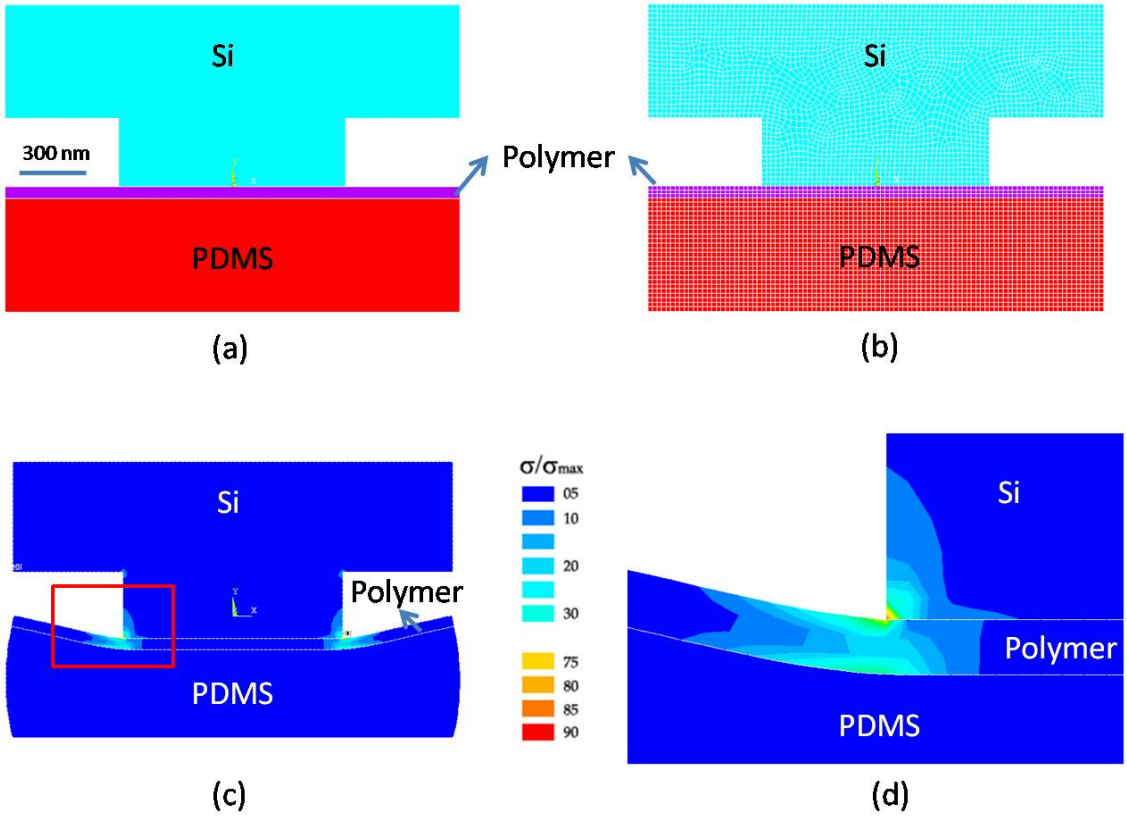

Figure 6.8: Finite element analysis results. (a) Model geometry, (b) Finite element mesh plot, (c) von Mises stress σ distribution, (d) A magnification of (c) showing the region marked with the square, where large stresses are localized.

6.6 Transfer Printing Light-Emitting Polymer

We then utilized the transfer printing procedure outlined in Section 6.3 and Figure 6.2 to pattern light-emitting polymers. First a single color subpixel array is demonstrated in Figure 6.9. The polymer layer to be patterned is the green light-emitting mixture PVK + PBD + C6 of about 75 nm in thickness, which is deposited on the PDMS surface by spin-coating. Micrographs shown on Figure 6.9a and Figure 6.9b were taken after the first transfer printing step, with Figure 6.9a taken on the stamp side and Figure 6.9b taken on the PDMS side. In Figure 6.9a the rectangular-shaped areas are the wells on the silicon stamp, which did not pick up polymer. The rest is coated with the polymer film that was picked up to the raised portion of the stamp during the transfer printing process. In Figure 6.9b the small rectangles shown are the polymer film and the background is the PDMS substrate. These two micrographs correspond to the two complementary patterns labeled as "I" and "II" in Figure 6.2 and are referred to as "negative" and "positive" patterns, respectively. By another transfer printing step, the positive pattern left on the PDMS is transferred onto a silicon substrate (acting as the target) and the final polymer array is shown in Figure 6.9c, which corresponds to the pattern labeled as "III" in Figure 6.2. After the second transfer step, the PDMS layer is clear of polymer residue as shown in Figure 6.9d, which corresponds to "IV" in Figure 6.2. The printing is done at $150°C$ and 400 psi for this particular experiment. Arrays with two different sizes, $12\mu m \times 40\mu m$ and $24\mu m \times 80\mu m$, are successfully patterned while only the latter is shown in the micrographs.

We then proceed to the patterning for a full-color display by repeating the previous transfer printing steps for the second and third colors as outlined in Figure 6.2. Since multi-layer alignment is required, we use a glass substrate to act as the target substrate and alignment is done with a mask aligner (Karl Suss MA6) aided with our work-around shown in Figure 6.3. Figure 6.10 shows two micrographs of transfer

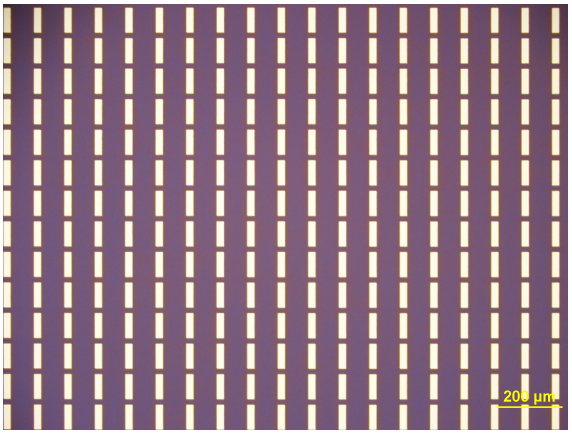

(a) Negative pattern on stamp

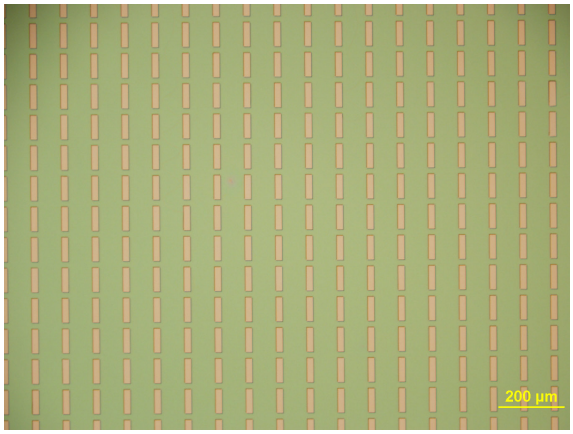

(b) Positive pattern on PDMS

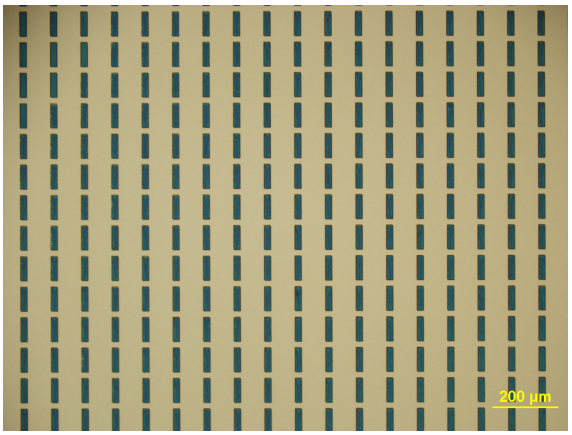

(c) Positive pattern transferred onto silicon

(d) PDMS layer surface after second transfer

Figure 6.9: Transfer printing method utilized to pattern PVK + PBD + C6 green light-emitting layer. Optical micrographs of the polymer patterns at different steps are shown. (a) Rectangular-shaped areas are recessed silicon stamp surface and the rest is polymer on the unetched (raised) area (refer to Figure 6.2 label "I"). (b) Polymer rectangle ($24\mu m \times 80\mu m$) array pattern left on the PDMS side (Figure 6.2 label "II"). (c) Polymer pattern shown in (b) is transferred onto a silicon target substrate by a second transfer step (Figure 6.2 label "III"). (d) Residue-free PDMS layer surface after the second transfer step (Figure 6.2 label "IV").

printed light-emitting polymer subpixel arrays. Figure 6.10a is an optical micrograph after the green and the red light-emitting subpixel arrays have been deposited by the transfer printing method. Figure 6.10b is an optical micrograph after all the three color (R, G, and B) subpixel arrays have been deposited. The mis-alignment of the third layer was caused by the relative movement of the two wafers after the alignment was done and when the small magnet was removed right before the printing step. The subpixels shown here have a size of $12\mu m \times 40\mu m$ and the full-color display have a pixel pitch of $48\mu m \times 48\mu m$, which translates to a color display resolution of 530 ppi (or 1590 ppi for a monochrome display). These results show that the transfer printing method has a super-high resolution capability, which is not easily achievable by other active organic patterning methods. Figure 6.11 shows two optical micrographs from the same experiments where a subpixel dimension of $24\mu m \times 80\mu m$ is used.[3]

As discussed in Chapter 5, uniform thickness of the light-emitting polymer is critical in order to achieve uniform light emission. In order to study the properties of the transfer printing technique related to layer thickness, surface profile scans are performed on transfer printed polymer layers, with a KLA-Tencor P-15 surface profiler. Multiple measurements are collected, and a typical scan is shown in Figure 6.12. Here the layer under study is a PVK+PBD+C6 layer that had been printed onto a silicon substrate with a printing condition of $90°C$ and 50 psi for both of the two printing steps. The thickness of the printed layer is 75 nm with a root-mean-square roughness of $\sim$1.2 nm calculated from multiple scans. This means that the transfer printed polymer layer have a very uniform thickness, mainly due to the fact that spin-coating was used for the initial layer formation. It also indicates that the transfer printing method does not significantly alter the polymer layer surface during process. The results shown here clearly demonstrate the superior properties of the

[3]Note that the results shown in Figure 6.10 and Figure 6.11 are not our best results with regard to the pattern qualities. We later optimized our printing process and better polymer patterns were printed. See Figure 6.13 for example.

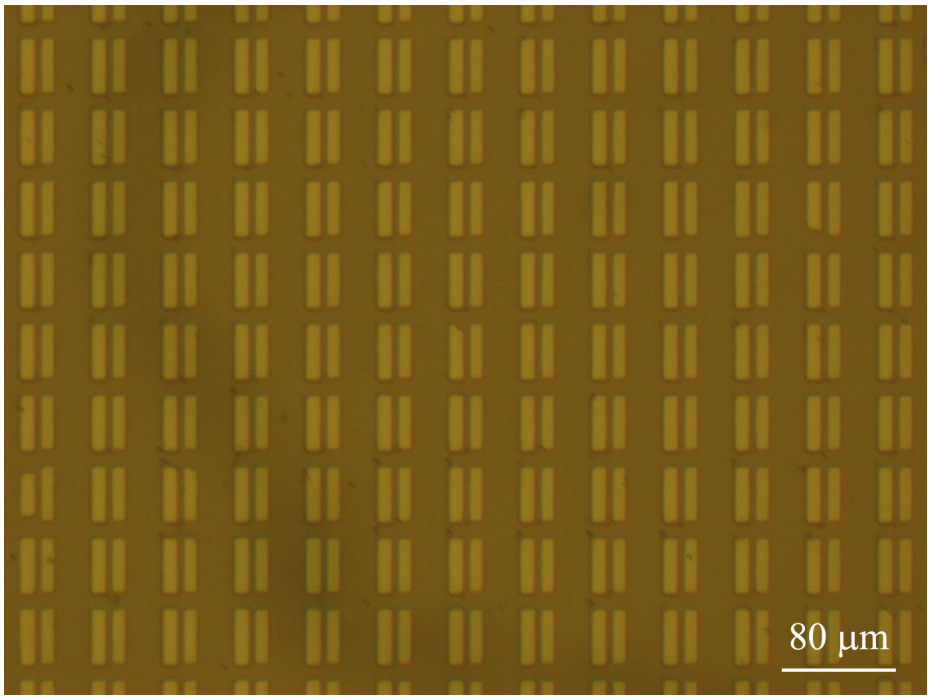

(a)

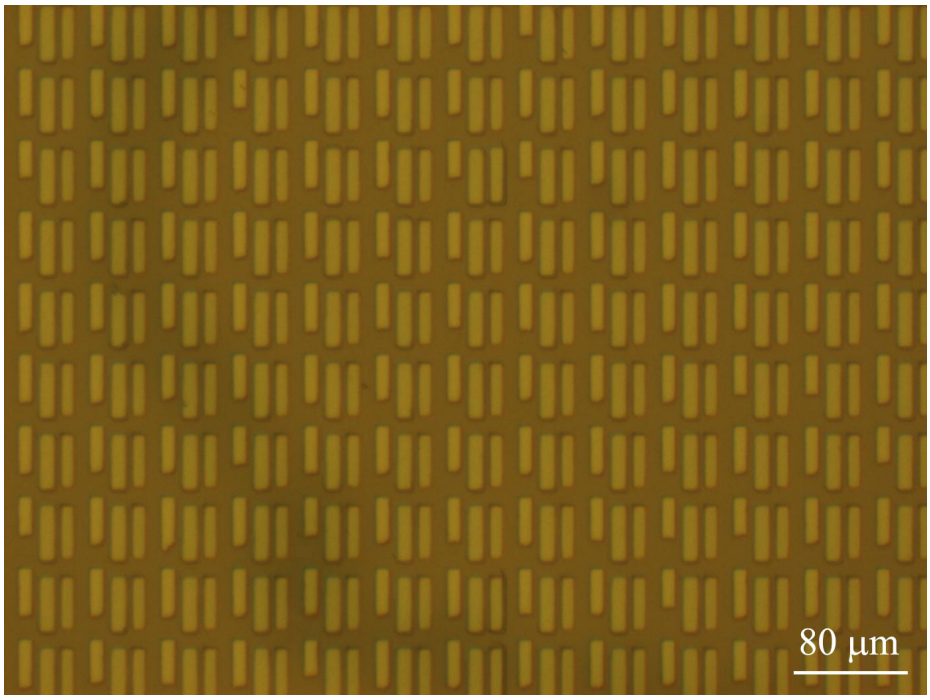

(b)

Figure 6.10: Optical micrographs of transfer printed polymer patterns. (a) After the green and red-color subpixel arrays have been deposited. (b) After the RGB-subpixels have been deposited.

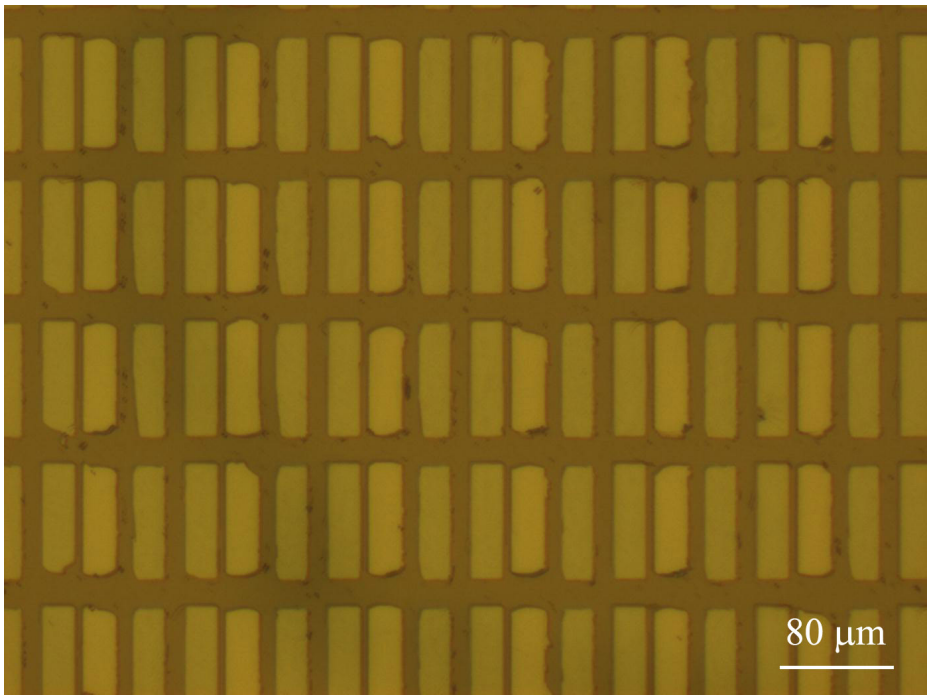

(a)

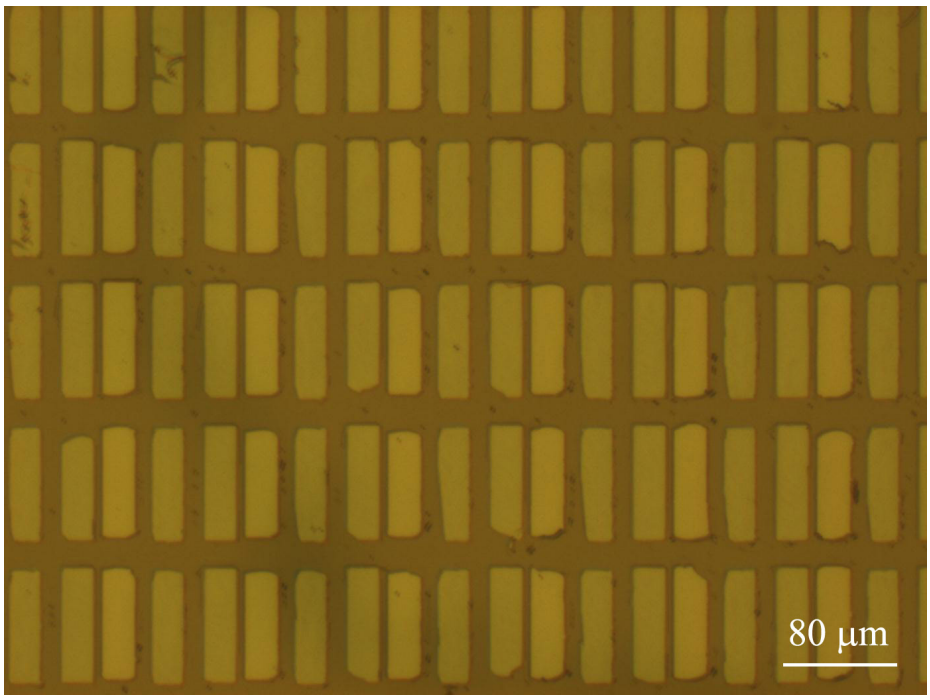

(b)

Figure 6.11: Two optical micrographs of transfer printed polymer patterns with R, G, B subpixels. Subpixel size is $24\mu m \times 80\mu m$.

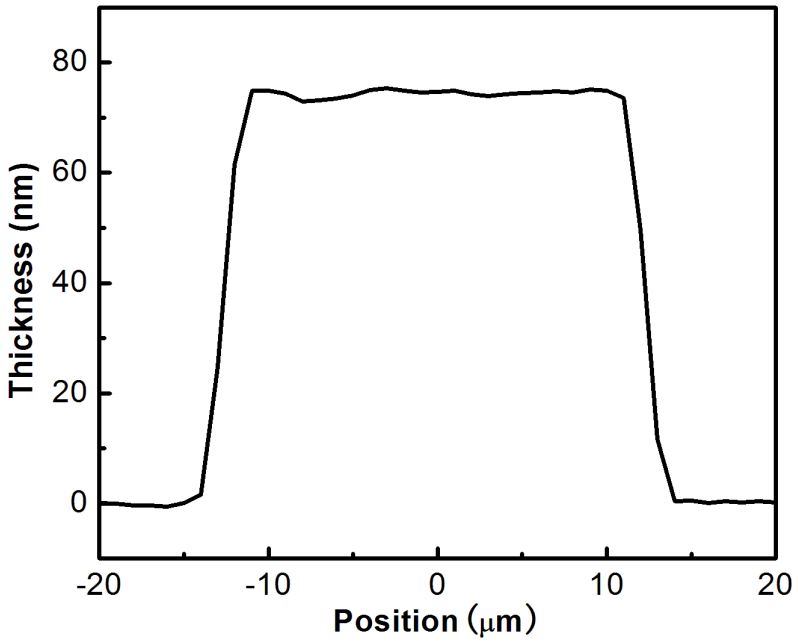

Figure 6.12: Surface profile scan of a typical transfer printed polymer film. The root-mean-square roughness is calculated to be ∼1.2 nm from multiple scans.

transfer printing technique with regard to thickness uniformity, in contrast to the usually uneven surface profiles resulted from other wet-printing methods.

We have optimized the transfer printing method to achieve better printing qualities. For example, we used cyclohexane as the solvent to spin coat the PDMS layer, instead of the initially used toluene, which greatly improved the film quality of the prepared PDMS layer. Two more micrographs of patterned polymer layers are shown in Figure 6.13 at higher magnification. PVK + PBD + C6 green mixture layer is again used here for the demonstration and the printing settings are $60°C$ and 50 psi. The rectangles again have dimensions of $24\mu m \times 80\mu m$. From these micrographs, it is clear that transfer printed polymer patterns have very sharp edges. In contrast, laser induced thermal imaging technique mentioned in Section 2.3.1 has very rough edges when used for polymer patterning (left part of Figure 2.2b, repeated here as Figure

6.14), probably because the force exerted on the polymer film is generated from the volume expansion of the underlying layer so that the force is not well defined in location. The ability of having sharp-edge polymer patterns is particularly important to achieve high resolution patterning.

6.7 Critical Conditions for Successful Printing

While a broad temperature and pressure ranges can be utilized for success patterning of the polymer layers, it is valuable to know the minimum temperature and pressure required. Various experiments are performed under different temperature and pressure settings for this purpose. The green mixture PVK+PBD+C6 is again used for these experiments. Figure 6.14 (a)-(h) show typical printed polymer patterns under boundary conditions. Each row has two micrographs, which are patterned under the same temperature but at slightly different pressures. In each row the pressures are chosen so that the left pattern has a poor quality pattern while the right image shows good quality pattern. For example, Figure 6.15a is an optical micrograph of a printed polymer patterned under $50°C$ and 40 psi, which clearly shows that the pattern quality is poor, while the good pattern shown to the right (Figure 6.15b) was achieved under the same temperature but with a higher pressure of 50 psi. By combining the results shown on Figure 6.15a and Figure 6.15b (and the fact that good pattern quality always resulted under even higher pressures, say 60 psi), we can say that the minimum pressure required for a complete pattern formation (breaking of the polymer film under the edges of the stamp protrusions) of the green mixture is $\sim$50 psi at a temperature of $50°C$. Similar experiments are performed at $70°C$, $90°C$, $110°C$, as shown in Figure 6.14 (c)-(h).

A pressure vs. temperature graph is drawn based on the experiments and is given in Figure 6.14i. Experiments which resulted in good quality patterns are drawn

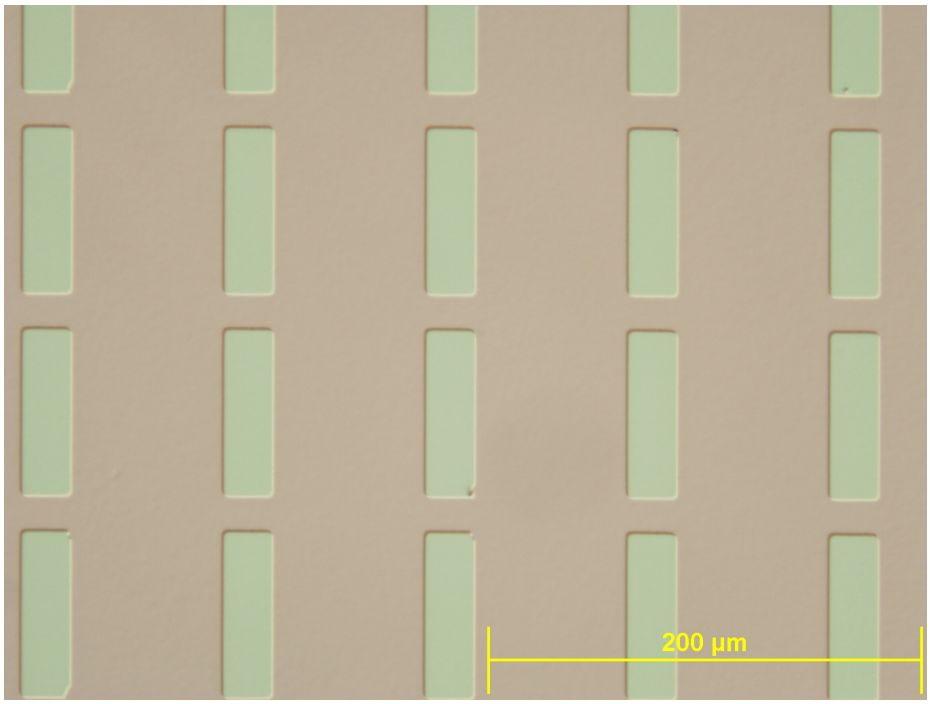

(a)

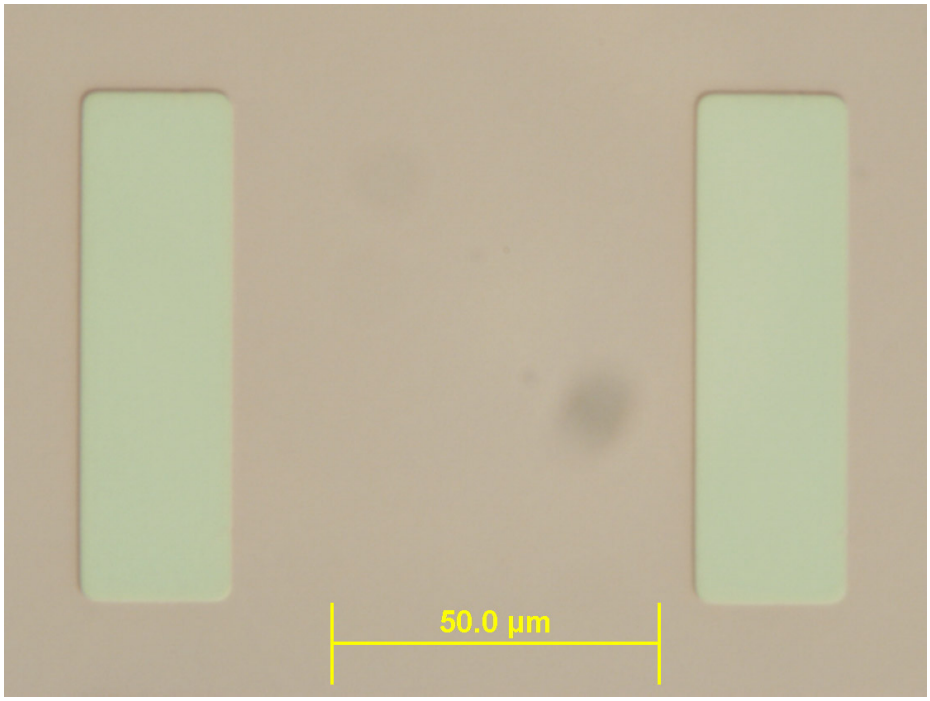

(b)

Figure 6.13: Transfer printing method can pattern polymer layers with very sharp edges. Two micrographs of PVK+PBD+C6 patterns printed at $60°C$ and 50 psi are shown at high magnification. Substrate is PDMS and size of the rectangles is $24\mu m \times 80\mu m$.

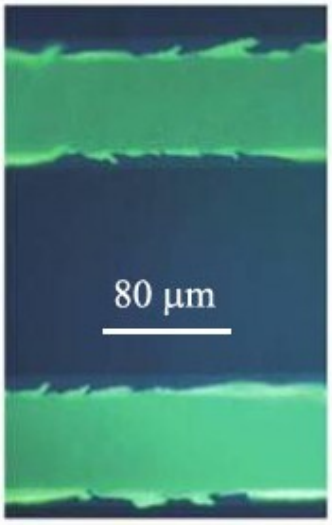

Figure 6.14: Polymer layer pattern deposited by laser-induced thermal imaging (LITI) method [45, 47].

as green dots, while bad quality patterns are drawn in red squares. The eight experiments which are located in the boundary regions (corresponding to Figure 6.14 (a)-(h)) are connected by a green line and a red line, respectively for convenience. The green line shown here is the minimum pressure and temperature settings in order to achieve a good pattern. Higher temperature and pressure (above the green line) will also result in good patterns and is designated as "working region", while to the lower-left of the red line is designated as "non-working region".

The results shown in Figure 6.14i suggests that the minimum pressure required for the breaking of polymer layer decreases (linearly to first proximation) as the printing temperature increases. In our finite element analysis simulation, when all layers are modeled by linear elastic materials, the maximum stress within the polymer layer (located close to the stamp edge) is linearly proportional to the value of the applied pressure. This suggests that the yield stress of the polymer blend layer also has a linear dependence on the temperature.

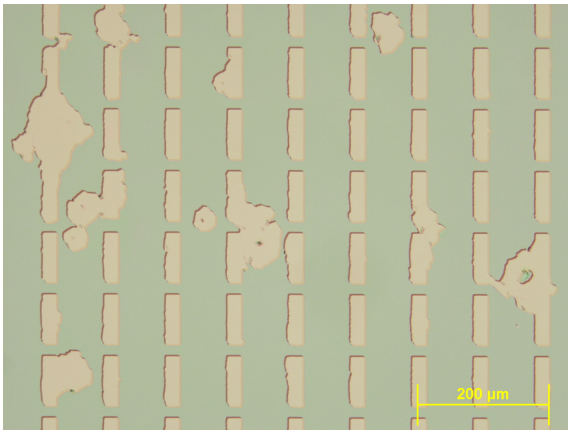

(a) 50°C, 40 psi

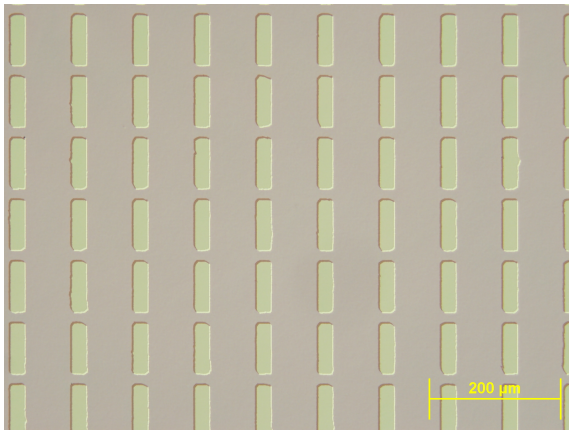

(b) 50°C, 50 psi

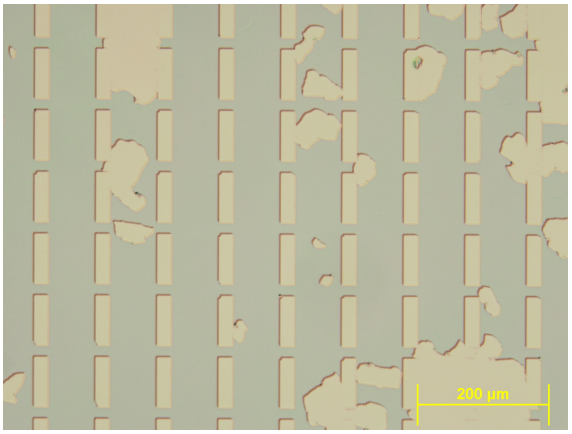

(c) 70°C, 30 psi

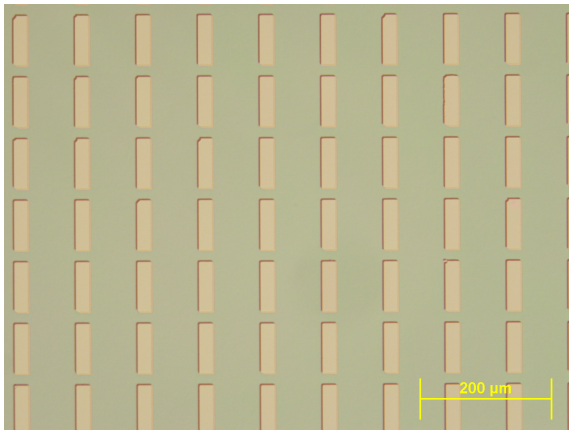

(d) 70°C, 40 psi

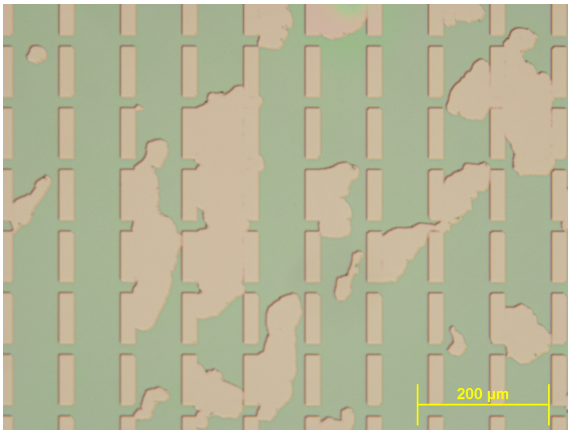

(e) 90°C, 20 psi

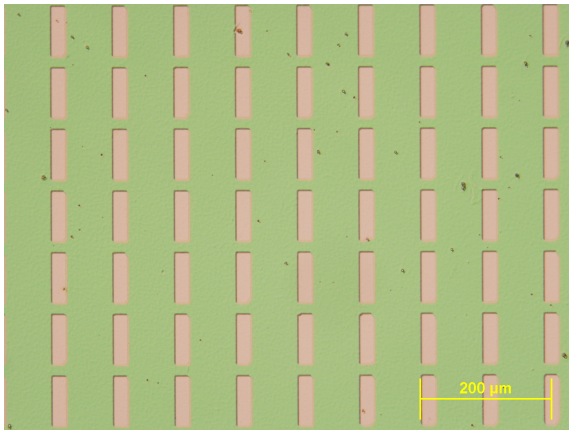

(f) 90°C, 30 psi

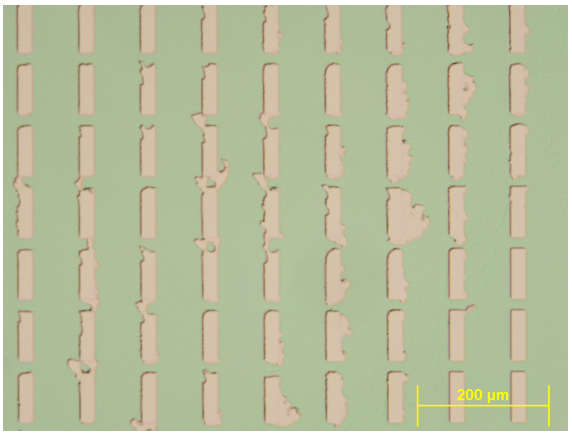

(g) 110°C, 10 psi

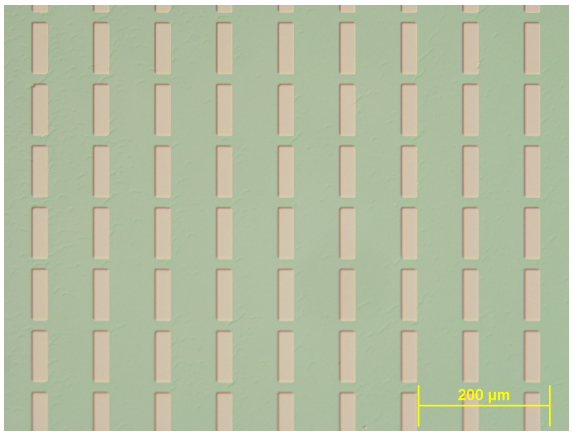

(h) 110°C, 20 psi

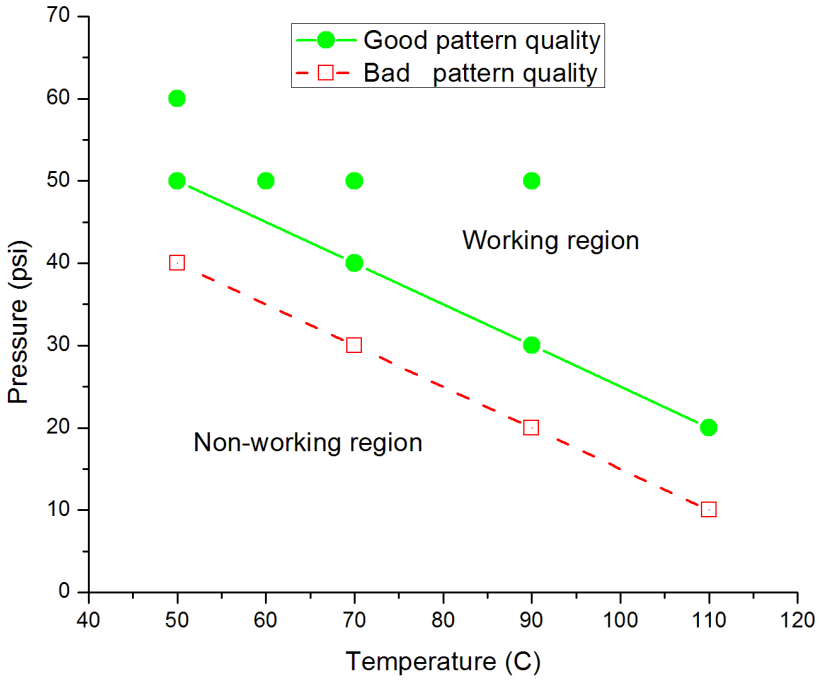

(i) Printing conditions used in experiments ((a)-(h), and extra) are plotted in Pressure vs. Temperature graphs. Two lines which show boundary printing conditions separating the "good" and "bad" regions are shown for convenience.

Figure 6.14: Various polymer layer patterns (PVK+PBD+C6 on PDMS side) resulting from transfer printing experiments with different printing temperature and pressure settings (a)-(h). Minimum temperature and pressure required for a good-quality pattern can be inferred from these experiments and are plotted in (i).

6.8 Fundamental Limiting Mechanism

In Section 6.5 the results of our finite element simulation suggest that the stress distribution within the polymer layer is non-uniform, with large stresses localized along the silicon stamp edges. The maximum stress calculated is proportional to the pressure applied on the top edge of the stamp. We hypothesis that the fundamental process which leads to the behavior of Figure 6.14i is that for the printing process to be successful the pressure applied on the stamp must be large enough, so that the maximum stress seen by the polymer layer must exceed its yield stress and thus a local rupture of the polymer at the edges will occur.

The yield stress of our film (PVK+PBD+C6) and its dependence on temperature is unknown, which prevents us from drawing a direct conclusion on the breaking mechanism of our transfer printing method. However, for most polymers, the yield stress does decrease as temperature increases. For example, Figure 6.15 shows the dependence of shear yield stress vs. temperature for three amorphous polymers, poly(vinyl chloride) (PVC), polycarbonate (PC), and PMMA. The data points are taken from Ref. [41] and the temperature axis has been normalized to $T - T_g$ for convenience, where T_g is the glass transition temperature. The three solid lines shown are linear fits to the data points for each polymer. It is clear from Figure 6.15 that the shear yield stress for these three polymers decreases linearly as temperature increases within the glassy range of $T < T_g$. Similar dependence of the yield stress on temperature was observed for other polymers, for example, polyethylene [7].

Several theories have been proposed to model the yield behavior of amorphous polymers as a function of temperature and strain rate, such as Ree-Eyring theory, Robertson theory and Argon theory [56]. For example, Ree-Eyring theory predicts that [56]:

$$\frac{\tau}{T} = A_\alpha[ln(2C_\alpha\dot{\gamma}) + \frac{\Delta H_\alpha}{RT}] + A_\beta Sinh^{-1}(C_\beta\dot{\gamma}exp\{\frac{\Delta H_\beta}{RT}\}) \tag{6.1}$$

Where, τ is the shear yield stress, T is the absolute temperature, R is the universal gas constant, $\dot{\gamma}$ is the strain rate, ΔH is the molecular activation energy required for molecular displacement, A and C are material constants.

With the fitting parameters $(A_\alpha, C_\alpha, \Delta H_\alpha, A_\beta, C_\beta, \Delta H_\beta)$ provided in Ref. [56] and assuming a low strain rate of $\dot{\gamma} = 0.00001[1/sec]$, the compression yield stress for PMMA and PC are calculated according to Eqn. 6.1 and are shown in Figure 6.16. The Argon theory calculation of PMMA is also shown, with its details given also in Ref. [56]. These different theories all predict an approximately linear dependence of the yield stress (tensile, compressive or shear stresses are related to each other by some factors) for amorphous polymers for $T < T_g$.

For the PVK+PBD+C6 films currently under study, they are also amorphous. In addition, the glass transition temperature of PVK is about $200°C$ and the effective glass transition temperature for the mixture is estimated to be about $120°C$ [23]. So the printing temperature of our experiments shown in Figure 6.14i falls in the glassy range similar to that of Figure 6.15 and Figure 6.16. Although experimental values of the yield stress of the PVK+PBD+C6 film under different temperatures are not available, it is reasonable to assume that they will follow a similar linear dependence on temperature, which agrees well with our experimental results shown in Figure 6.14i.

Based on the previous discussion, we propose that the pattern formation is a result of polymer yield and breaking at the stamp edge when the applied pressure is large enough so that the stress exceeds the yield stress of the polymer film. Other possibilities, for example, that the polymer pattern was formed due to a stretching effect when the stamp is peeled off, is unlikely. This is because the two plates was separated from each other after the pressure had been released and the temperature had been cooled down to room temperature. Thus the results will not heavily depend on the printing pressure and temperature, which is contrary to our experimental

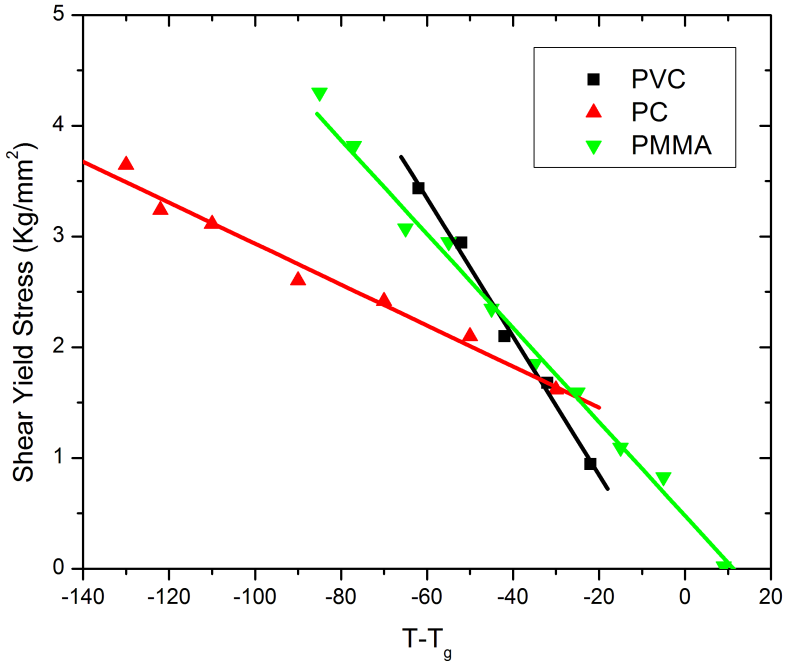

Figure 6.15: The shear yield stress vs. T-T_g for PC, PVC and PMMA. Data points taken from Ref. [41].

results.

6.9 Device Characterization with Printed Polymer Films

Since active materials are patterned in this work, it is essential to study the electronic properties of the polymer layers after processing and the interface between the printed material and the underlying layers. Several outcomes are possible as a result of the transfer printing process. For example, the printed layer may not form intimate contact with the ITO target substrate and thus may prevent hole injections into the polymer layers. Also, the polymer layers may degrade during the thermal and pressure cycles.

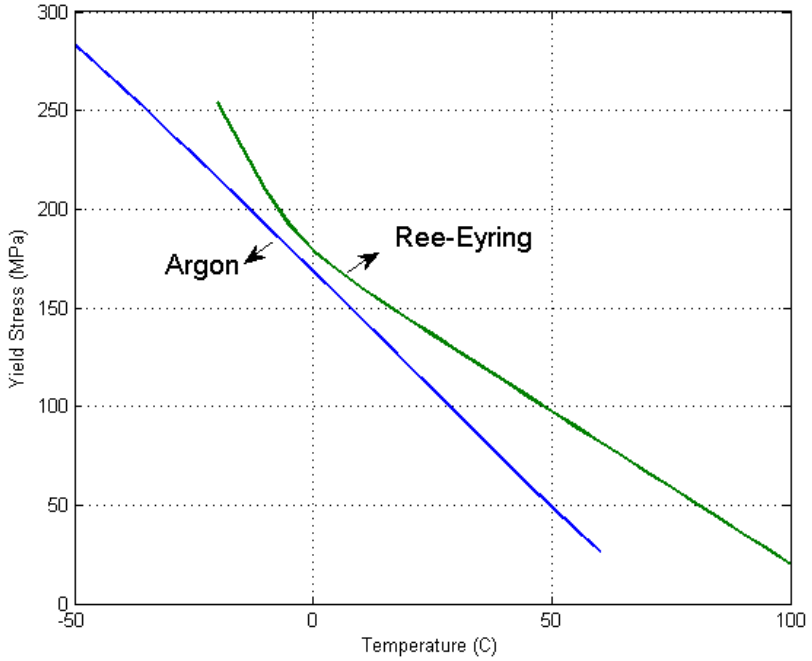

(a) PMMA, $T_g = 105°C$

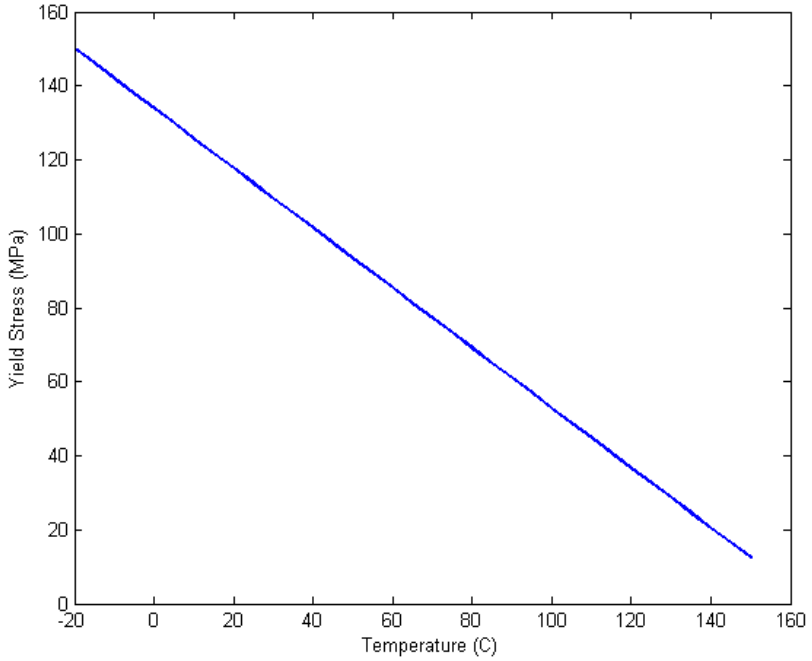

(b) PC, $T_g = 150°C$

Figure 6.16: The compression yield stress vs. temperature predicted by Ree-Eyring model for (a) PMMA and (b) PC. The Argon model is also shown for PMMA. Parameters used for the calculation are from Ref. [56]

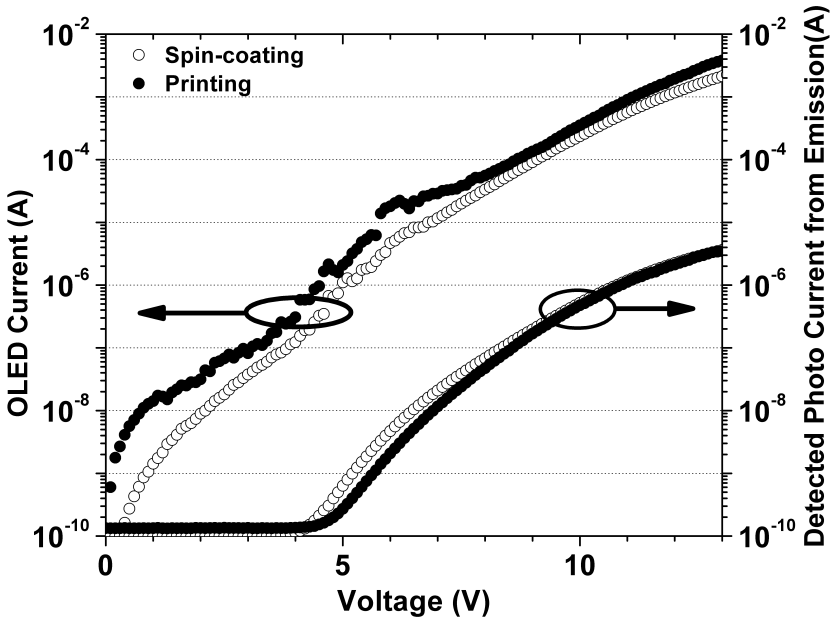

Figure 6.17: Comparison of I-V characteristics of OLEDs with polymer film deposited by transfer printing ($50°C$ and 50 psi) and spin coating.

We have fabricated OLED devices where the polymer blend film (usually the green mixture) was transfer printed onto an ITO-coated glass substrate followed by thermal evaporation of Mg:Ag cathode layer. Control devices with the same structure are made with the light-emitting layers deposited by spin-coating. Figure 6.17 shows I-V curves and light emission vs. voltage curves from printed devices (closed symbols) and from spin-coated control devices (open symbols). The printing condition used is $50°C$ and 50 psi. Both the I-V curves and the light emission from the two devices almost overlap with each other, meaning the devices printed under $50°C$ and 50 psi have similar performance compared to spin-coated controls. The results clearly show that the interface between the printed layer and the ITO bottom electrode is of good quality. In addition, the printed layer itself must have retained its original electronic and optical properties after the transfer printing process.

Since a broad range of temperature and pressure are used in our printing exper-

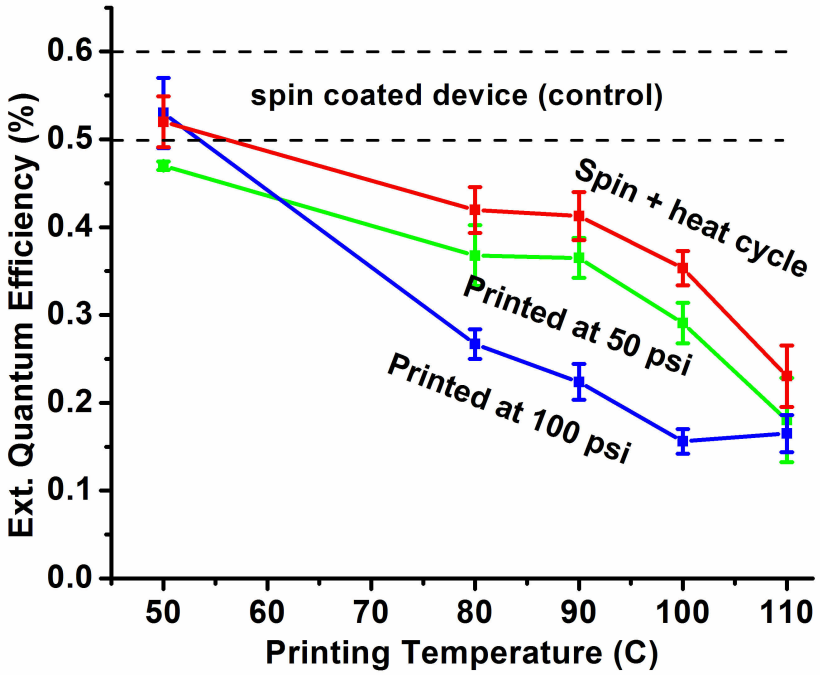

Figure 6.18: Effect of printing temperature and pressure on OLED device performance. The external quantum efficiency is calculated for comparison. Efficiencies are compared to spin-coated control devices, which mostly fall into the range marked with the two dashed lines. Devices labeled with "spin + heat cycle" were prepared with spin-coating that had undergone the same thermal cycle with printed devices.

iments, it is also worthwhile to study the effect of printing condition on device performance. For this purpose, printed devices were fabricated under various printing conditions and tested. Figure 6.18 shows the external quantum efficiencies of devices prepared under a printing pressure range of 50–100 psi and temperature range of 50–110°C. The spin-coated control devices have external quantum efficiencies in the range of about 0.5–0.6%, which are marked in the graph by the two dashed lines. Devices prepared at 50°C have identical performance compared to spin-coated control devices. However, higher temperature and higher pressure during the printing steps are harmful to device performance.

Based on our understanding about the transfer printing process, we suspect that several reasons could lead to the observed temperature and pressure effect. For exam-

ple, organic materials are known to degrade due to thermal treatment. In addition, since physical contact is made during the printing procedures, contact-related defect (e. g., contamination caused by contact of two surfaces) could easily occur, which might affect device performance.

We suspected that thermal degradation might be a main factor in causing the performance dependence on temperature. For that purpose, we fabricated special devices which are labeled as "spin + heat cycle" devices. In the "spin + heat cycle" devices, the polymer layers were spin-coated onto ITO-glass substrate and were inserted into the nano-imprinter to undergo the same thermal cycle as the printed polymer layer, except that no pressure was applied on the spin-coated layer. After the thermal cycle, Mg:Ag cathode was evaporated and the devices were tested. The external quantum efficiencies of these devices are also given in Figure 6.18, labeled as "spin + heat cycle". Comparing the "spin + heat cycle" devices with spin-coated control devices, the only difference is that the former had undergone an additional thermal treatment process. In contrast to the spin-coated controls, however, these devices share a similar dependence of the device performance on temperature to the printed devices, as can be seen from Figure 6.18. These results show that thermal degradation is probably the most important factor that affects the device performance during the transfer printing process.

We also measured the printed film thickness at different printing pressures. The results are shown in Figure 6.19. The initial film thickness of the PVK+PBD+C6 layer formed by spin coating is about 73.5 nm. The films were printed onto a silicon substrate at the same temperature of $110°C$ but with different pressures from 10, 50, 100 to 200 psi. As can be seen from Figure 6.19, a thinner film thickness is measured when a higher pressure is applied. The decrease of film thickness, and the film morphology change as a result of the squeeze, during the printing cycle, might affect the final device performance as well, in addition to the thermal degradation

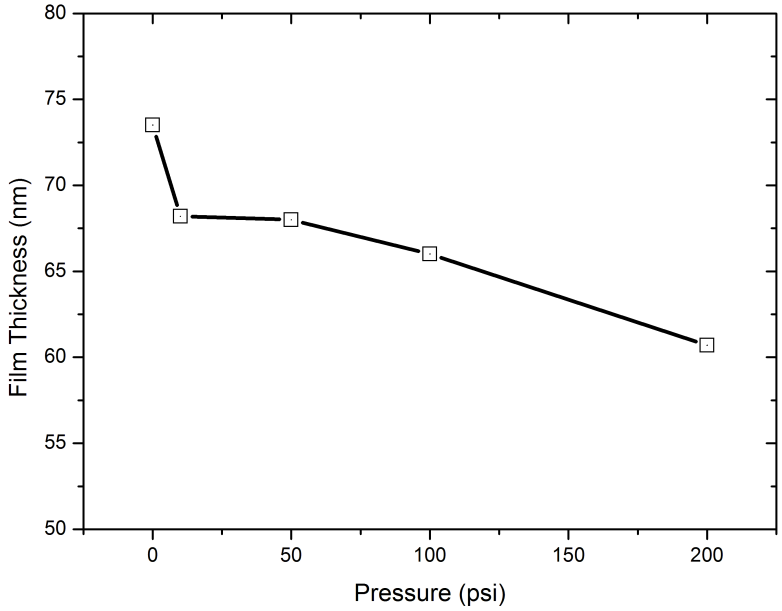

Figure 6.19: Effect of pressure on film thickness of the printed PVK+PBD+C6 layer.

effect.

In conclusion, our experimental results suggest that thermal degradation is the main factor resulting in the performance dependence of printed devices. Other factors, such as film thickness or morphology change and contact-related defects and extended exposure of the layer to air, etc, might also contribute to the lower efficiencies.

6.10 Summary

In summary, we developed a transfer printing technique used for polymer layer patterning aimed for full-color OLED applications. R, G, and B subpixel arrays are successfully patterned with transfer printing as a demonstration of the method. This method is able to achieve very high resolution (over 530 ppi color display resolution) with good quality patterns and sharp edges and uniform film thickness. OLED devices with printed polymer layers under modest temperature and pressure show

performances comparable to spin-coated control devices, meaning the printed/ITO interface is nearly "ideal" and the printed layers retain the original electronic properties after the printing process. However, higher temperature or higher pressure conditions are found harmful to device performance, which is thought to be caused mainly by thermal degradation of the polymer introduced during the printing process. The transfer printing method is believed to have low-cost potential for full-color OLED display fabrications since it is a parallel process (so high throughput) and the stamp is reusable, etc.

We believe that the transfer printing method is versatile and can be utilized for the fabrication of OLED displays for various applications, either large-area displays or small-to-medium sized displays. In particular, the transfer printing method is capable of super-high-resolution patterning, which has not been demonstrated in other patterning techniques. It might find unique application opportunities in areas where a super-high resolution is required, such as the micro-displays found in electronic viewfinders for cameras and camcorders, head-mounted displays used for mobile computing, virtual reality, or computer-gaming applications, etc. As shown in Figure 1.3, eMagin already has several micro-display modules available on the market but a white OLED + color filter structure is utilized in their current products for the moment. The eMagin SVGA+ micro-display shown in Figure 1.3a has a resolution of $852(\times 3) \times 600$ with a diagonal size of 0.61" and a pitch of only 15 μm. With other patterning techniques currently available, it is difficult to achieve such a small feature size, while our transfer printing method have already demonstrated a color pixel pitch of 48 μm and we think it has a great potential to go to even higher resolution. If a R, G, B self-emitting subpixel configuration can be used instead of the white OLED + color filter approach, higher power efficiencies can be achieved, which is critical for mobile applications.

Chapter 7

Transfer Printing Without Polymer Edge Breaking

7.1 Overview

In Chapter 6 we introduced a transfer printing method for the patterning of light-emitting polymer layers aimed at full-color OLED display applications. A stamp is pressed against the spin-coated polymer layer to break the layer at the edges of stamp protrusions, followed by a transfer step to deposit the polymer pattern onto a device plate. The minimum temperature and pressure required for a successful breaking is related to the mechanical properties of the polymer films. In this chapter we introduce an alternative transfer printing method in which the mechanical-breaking step of the polymer films is not necessary. Instead, the polymer film to be patterned is directly deposited onto the patterned stamp surface by spin coating. Since the stamp has protrusions and recessions, discrete regions of the polymer film are formed by spin-coating. Followed by a transfer printing step, the polymer layers on the stamp protrusions can be deposited onto a device plate, while the rest of the polymer films will remain on the stamp. This method is similar to the work by Choi et al [13] but polymer layers are patterned in our work instead of small molecules. Two different approaches have been explored within this category and they are referred to as the

"hard-hard" and the "hard-soft" approaches, respectively. The details of the two different approaches will be discussed in the following sections.

The information in this chapter was presented in Ref. [36].

7.2 The Hard-Hard Approach

7.2.1 Concept of the Hard-Hard Approach

The concept of the hard-hard approach of the transfer printing method is illustrated in Figure 7.1. First, a hard printing stamp is prepared with designed protrusion/recession patterns. The printing stamp is usually made from silicon and is fabricated by conventional photolithography followed by reactive-ion etching. In order to achieve successful releasing of the polymer layers from the stamp surface in the following steps, the stamp surface is treated with a low-energy self-assembly layer. In this work, PFOTS is chosen as the layer and is grown on the stamp surface by solution process. The detail of the PFOTS growth has been discussed in Section 4.2. The polymer layer to be patterned is then spin-coated onto the stamp surface. The stamp has a depth of protrusions in the range of several hundred nanometers while the polymer layer is ∼100 nm so the polymer layer formed is discontinuous. The stamp is then brought into contact and pressed against a device plate (e.g., silicon or glass, which is usually hard) at elevated temperature. Upon separation, polymer layers on top of the protrusion region, and thus in direct contact with the substrate, will be transferred onto the substrate due to the adhesion difference. The rest of the polymer film remains on the stamp, since it is not in contact with the device plate surface. By repeating these steps three times, we are able to create patterned R, G, B subpixel arrays required for full-color OLED displays.

This approach is referred to as the "hard-hard" approach, due to the fact that both the stamp and the substrate which come into contact are hard.

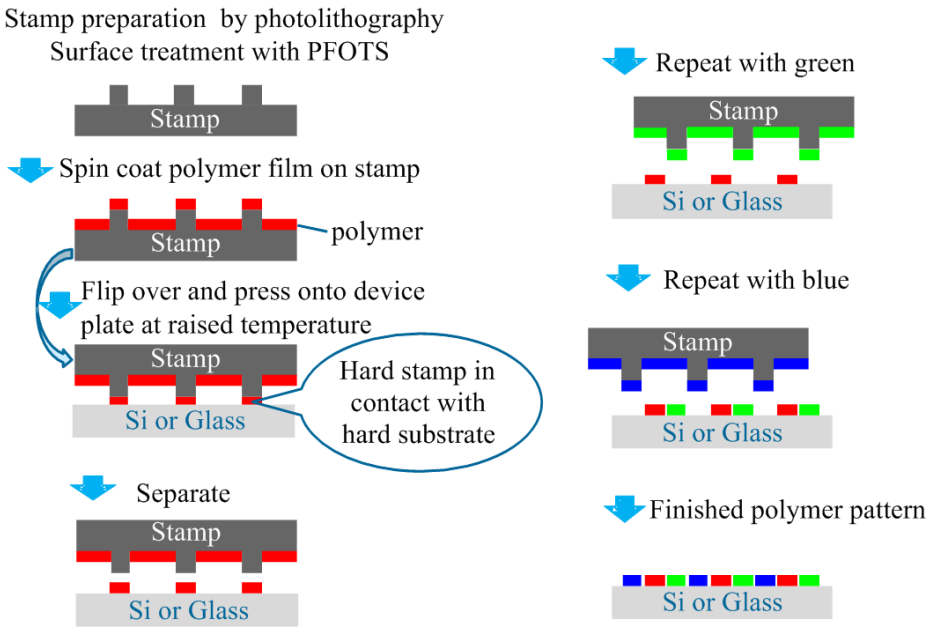

Figure 7.1: Schematic diagram of the hard-hard approach of the transfer printing method.

7.2.2 Printing Results

The hard stamp used in the hard-hard approach is fabricated from a silicon wafer. As a demonstration, arrays of rectangular-shaped protrusions with a dimension of $24\mu m \times 80\mu m$ are etched into the silicon wafer at a height larger than 700 nm. The stamp after the patterning is immersed into a ~20 mM PFOTS in non-hydrous dodecane solution and kept overnight to allow the self assembly on the stamp surface. The stamp is then removed from the solution and rinsed with DI water and blown dry. The green blend PVK+PBD+C6 is used and is spin coated to form a thin layer on top of the stamp surface. Figure 7.2a shows a micrograph of the stamp after the spin-coating of the polymer blend.[1] We can see that the spin-coated polymer film covers only part of the raised features and the film is not continuous. This can be

[1]The stamp surface after the PFOTS treatment is very hydrophobic. It is generally very difficult to form a polymer layer on top of a hydrophobic surface by spin-coating. In our experiments, we found that the PFOTS-coated stamp can be successfully spin-coated with the polymer layer. However, in a control experiment where a PFOTS-coated flat silicon wafer is used, spin-coating of the polymer layer is almost impossible. The differences observed may arise from the fact that the stamp surface is not flat so that it's more difficult to de-wet the solution.

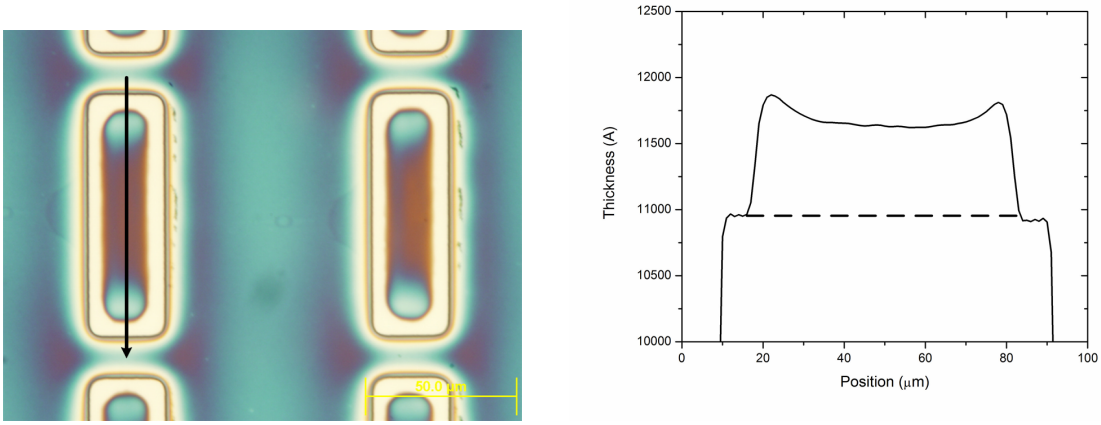

(a) (b)

Figure 7.2: The polymer layer formed by spin-coating on the stamp protrusion is non-uniform in thickness. (a) An optical micrograph of the polymer-coated stamp surface. (b) A typical surface profile scan of the polymer-coated stamp along the line shown in (a). The dashed line refers to the stamp substrate

more clearly shown in a line scan of the film. Figure 7.2b is a typical line scan that is performed along the line shown in Figure 7.2a. The dashed line shown in Figure 7.2b refers to the top of the protrusions before the film deposition. It is clear that the spin-coated film covers the center portion of each protrusion and the film thickness is not uniform, especially in areas close to the protrusion edges where pileup of the polymer is observed.

After the spin-coating of the polymer blend on top of the stamp surface, the transfer printing step is performed with a nano-imprinter (Nanonex NX-2000). Figure 7.3 shows the final pattern on a silicon substrate after the transfer printing step performed at a pressure of 500 psi and various temperatures: (a) $110°C$, (b) $130°C$, (c) $150°C$. At 500 psi and $110°C$ only small part of the polymer film are transferred. At 500 psi and $130°C$ more polymer film are transferred and at $150°C$ near-complete transfer is observed. Figure 7.4 shows two micrographs of the stamp surface after the transfer printing, which correspond to incomplete transfer (Figure 7.4a) and complete transfer cases (Figure 7.4b). It is clearly shown from Figure 7.4a that in the case of

incomplete transfer, often only the polymer films at the edge of each protrusion are transferred while the center part of the films (on each protrusion) are left behind on the stamp.[2] As shown in Figure 7.2 the spin-coated polymer films are un-even in thickness and are usually thicker at the edges. During the transfer printing step, only the thick part of the polymer films are in contact with the device plate and thus are transferred. The rest of the polymer film can not make a physical contact with the device plate and thus is left on the stamp. When the temperature is high, the polymer film becomes softer and thus can deform more easily to achieve a more intimate contact. This explains the trend observed in Figure 7.3: when the temperature is raised from $110°C$ to $130°C$ then to $150°C$, more and more polymer are transferred, while almost complete transfer is observed in the latter case. In the final case, the temperature used is $150°C$ which is $30°C$ higher than the effective glass transition temperature of PVK + PBD + C6, estimated to be $120°C$ [23]. So the polymer film is soft enough and can deform under the high pressure of 500 psi until a conformal contact is achieved. After the transfer, the surface of the stamp protrusions are clear of polymer films, as shown in Figure 7.4b.

Figure 7.5 is an illustration of the hard-hard transfer printing approach in dealing with non-flat surfaces. The polymer film formed by spin-coating is non-uniform in thickness. And both the stamp and device plate are hard so during the transfer printing step usually a non-conformal contact is achieved. As a result, only the portion of polymer film in direct contact with the device plate can be successfully transferred. Only under high temperature and high pressure settings can the polymer film deform enough to achieve a better contact and thus an almost complete transfer.

Although the transfer printing results using the hard-hard approach is not opti-

[2]In the case of incomplete transfer the polymer films do break up. We think the breaking mechanism here is different to the one discussed in Chapter 6. The breaking here might be caused by the stretching of the polymer film during the separation of the two plates. Notice that breaking occurs at different positions for different pixels and the partially transferred films are randomly shaped, as shown in Figure 7.3b and Figure 7.4a

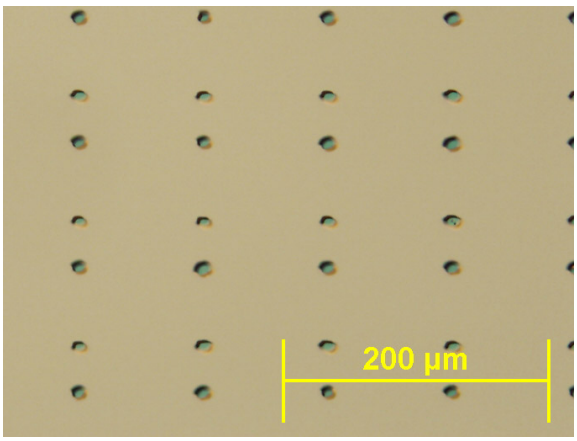

(a) 110°C

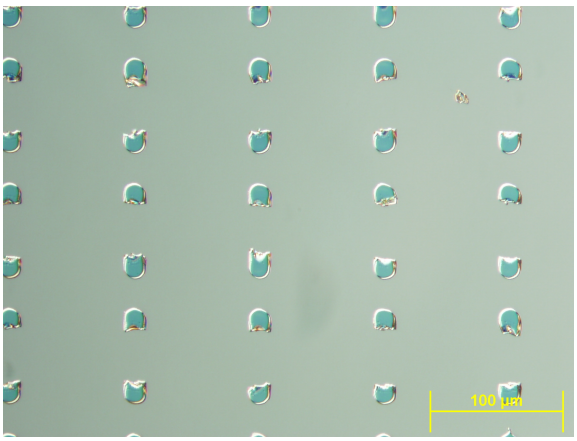

(b) 130°C

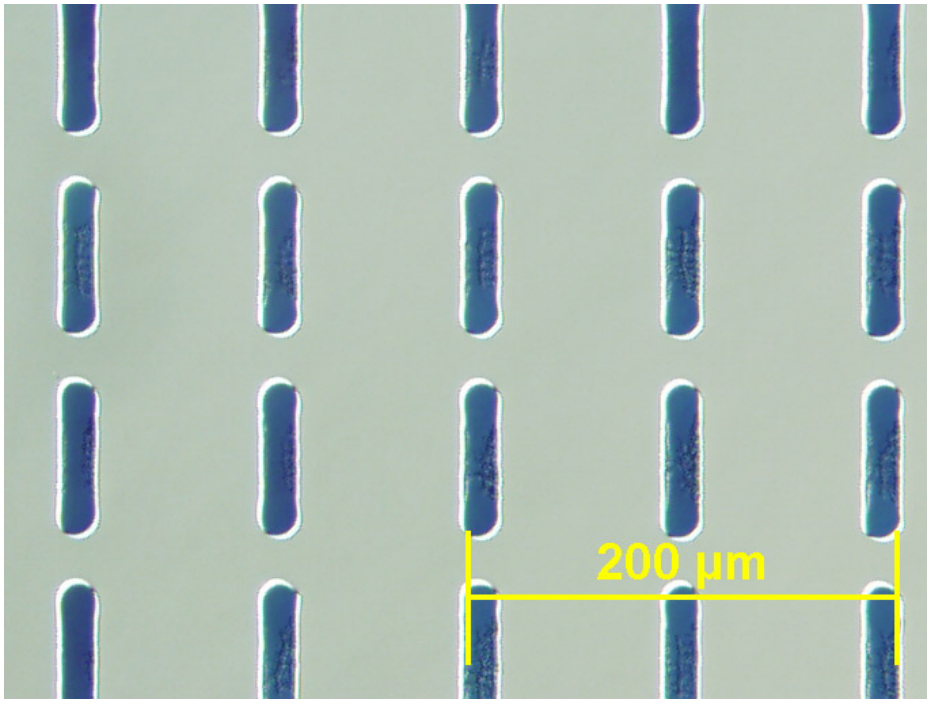

(c) 150°C

Figure 7.3: Printing results of the hard-hard approach at pressure 500 psi and at different temperature. Micrographs shown here are the final pattern of PVK+PBD+C6 blend after being transferred onto a silicon substrate.

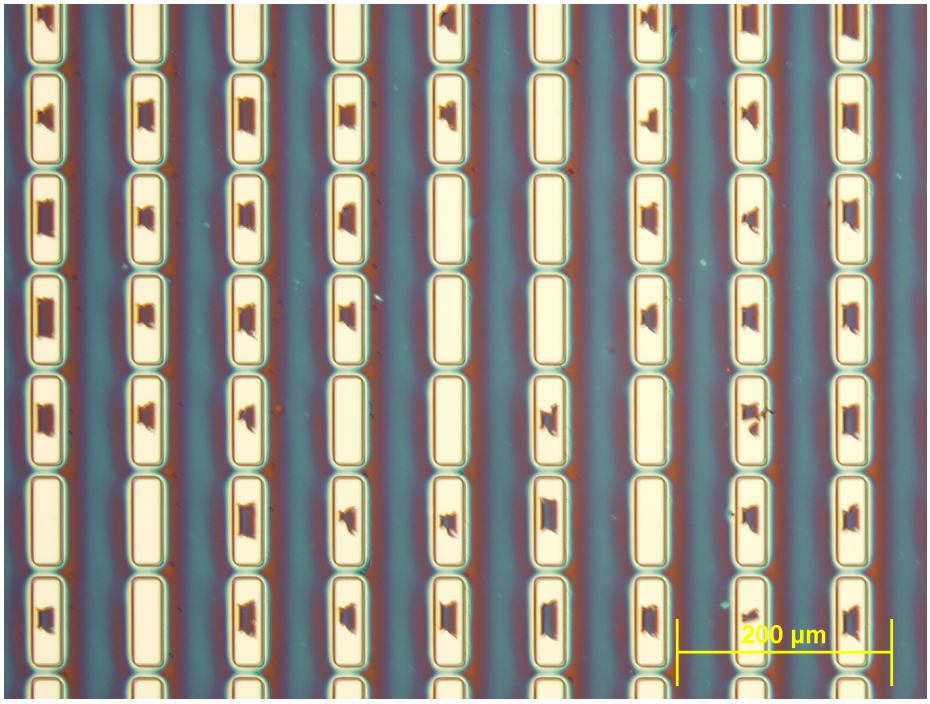

(a) Incomplete transfer, 130°C and 500 psi

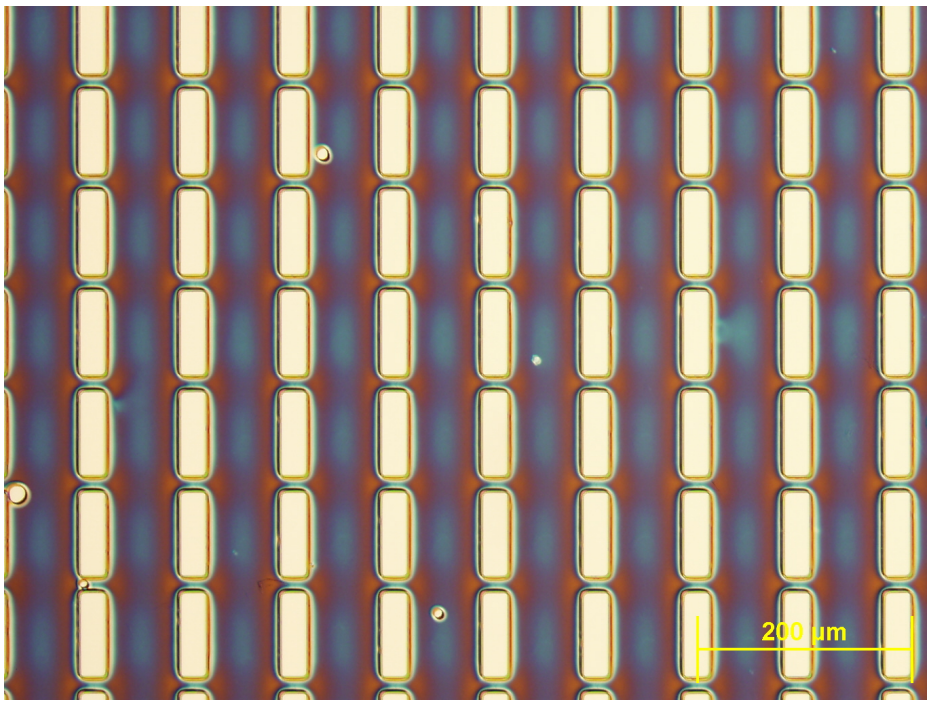

(b) Complete transfer, 150°C and 500 psi

Figure 7.4: Micrographs of the stamp surface after the transfer printing step. Incomplete vs. complete transfer are observed under different printing conditions.

Figure 7.5: Schematic diagram of the hard-hard approach in dealing with non-flat surface.

mum, we still went forward and demonstrated its ability in organic patterning for full-color OLED displays. An example of the hard-hard approach used for R, G, B subpixel array patterning is given in Figure 7.5. For this demonstration, the three blend films are patterned one-by-one with the hard-hard approach and deposited onto a single glass substrate. A glass substrate is used here as the device plate since visual alignment is required for multi-layer registration. Alignment is done in the same way as shown in Figure 6.3 and its discussions. All printing is done at 500 psi and 150°C in order for an almost complete transfer to occur. Figure 7.6a is an optical micrograph of the glass substrate after the green light-emitting blend has been deposited by the hard-hard approach. Figure 7.6b is taken after the red light-emitting blend has also been deposited and finally Figure 7.5c is taken after the blue light-emitting blend has also been deposited. The mis-alignment was caused by machine limitations used for the alignment. Although the printed polymer patterns are not perfect, they clearly demonstrate the ability of the hard-hard approach as a patterning method for polymer patterning.

7.3 The Hard-Soft Approach

As demonstrated in the last section, the hard-hard approach lacks the ability to deal with non-flat surfaces which often results in incomplete transfer. In this section, we propose and explore a hard-soft approach that can accommodate non-ideal surfaces more easily. The concept of the hard-soft approach and its printing results are

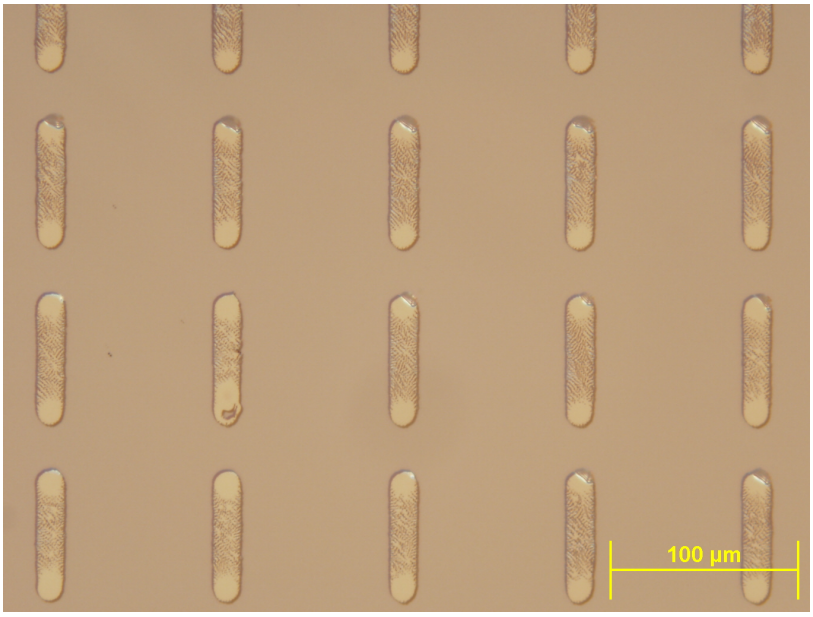

(a)

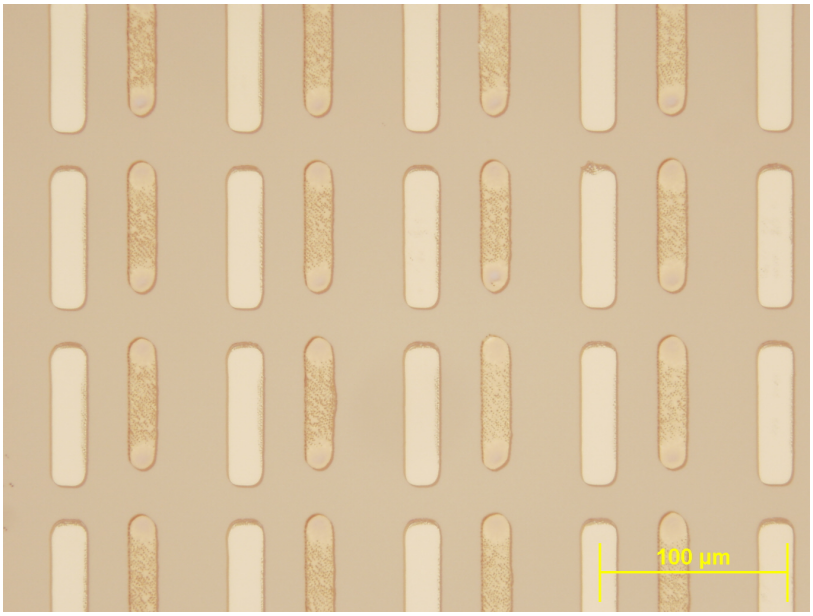

(b)

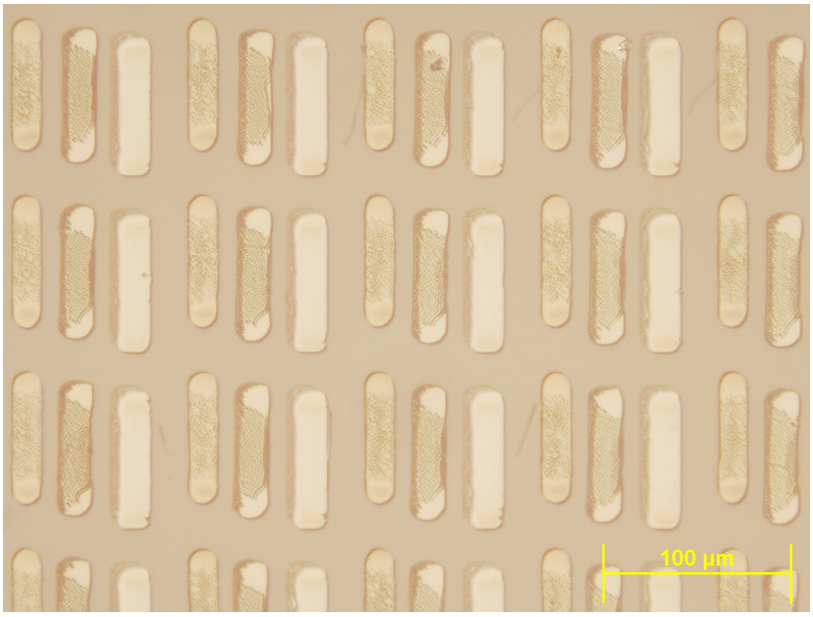

(c)

Figure 7.5: Optical micrographs of transfer printed polymer patterns. (a) After the printing of the green subpixel arrays. (b) After the printing of the red subpixel arrays. (c) After the green, red, and blue-subpixels have been deposited.

discussed below and are compared to the results from the hard-hard approach.

7.3.1 Concept of Hard-Soft Approach

The concept of the hard-soft transfer printing approach is illustrated in Figure 7.6. The first two steps of the hard-soft approach are the same as the hard-hard approach, i.e., the fabrication of the hard stamp and the surface treatment with PFOTS followed by spin-coating of the polymer layers on top of the stamp surface. The main difference of the hard-soft approach, compared to the hard-hard one, is that an intermediate transfer step by using a soft layer is introduced. Here, the same PDMS-coated silicon substrate that is used in Chapter 6 is used. In the first transfer printing step, the stamp is brought into contact and pressed against the PDMS/Si substrate at elevated temperature. Upon separation, polymer layers on top of the stamp protrusion regions, and thus in direct contact with the PDMS surface, will be transferred onto the PDMS side. For this to occur, the surface energy of the PDMS layer needs to be adjusted

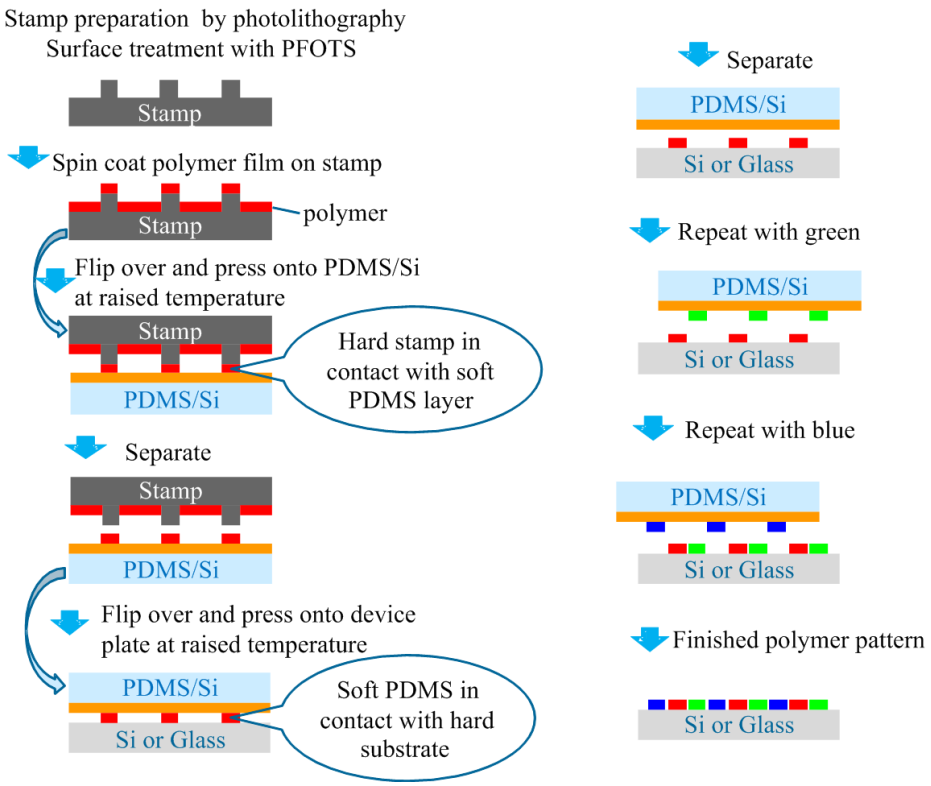

Figure 7.6: Schematic diagram of the hard-soft transfer printing approach.

beforehand. By another transfer printing step, the pattern on the PDMS/Si side can be further transferred onto a device plate (silicon or glass have been used for demonstration purpose). By repeating these steps three times, we are able to create patterned R, G, B subpixel arrays required for full-color OLED displays. Notice that the PDMS layer is soft and it is used in both of the two transfer printing steps, so that the contact in both printing steps become a "hard-soft" one.

7.3.2 Printing Results

In the hard-soft transfer printing approach, the polymer layers are transferred twice, first from the stamp to the PDMS, then from the PDMS to the final target plate. In order for the transfer to occur, the surface of the PDMS needs to be treated so that the adhesion of the polymer layer to the PDMS layer is higher than that of the stamp surface while lower than that of the final substrate. The stamp surface has

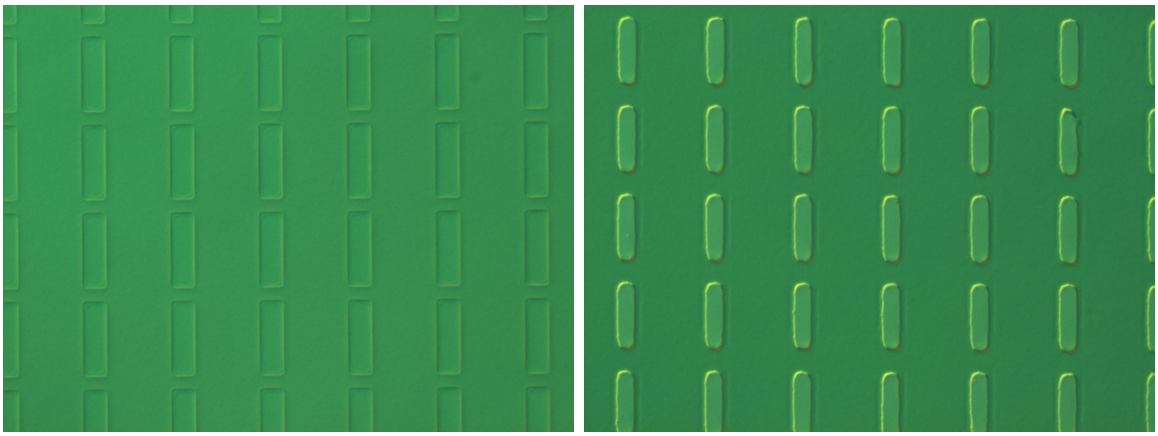

(a) No oxygen plasma treatment on the PDMS (b) PDMS treated with oxygen plasma for 30 seconds

Figure 7.7: Micrographs of the PDMS surface after the first transfer printing step. (a) No oxygen plasma treatment is performed on the PDMS surface before the transfer printing. No polymer is transferred onto the PDMS side (the contrast seen on the image is impression caused by the pressing of the hard stamp). (b) The PDMS is treated with an oxygen plasma for 30 seconds, which results in the successful transfer of the polymer films onto the PDMS.

been treated with a PFOTS layer and thus is not sticky. The device plate surface (either glass, silicon or ITO) is usually in a high energy state when clean. We use an oxygen plasma to treat the PDMS surface in order to achieve a medium surface energy state.

Figure 7.7 shows two optical micrographs of the PDMS surface after the first transfer printing step. For Figure 7.7a no plasma treatment has been performed on the PDMS layer before the transfer printing. For Figure 7.7b the PDMS surface has been treated with oxygen plasma for 30 seconds before the printing. As shown in the two micrographs, no polymer film has been transferred onto the PDMS surface for Figure 7.7a,[3] while a complete transfer of the polymer films is observed for Figure 7.7b.

Figure 7.8 shows two optical micrographs of the PDMS surface after the second

[3]The rectangular-shaped contrast shown in the image are impressions left on the PDMS caused by the pressing of the hard stamp. This is often observed when the PDMS baking was done at low temperatures such as $130°C$.

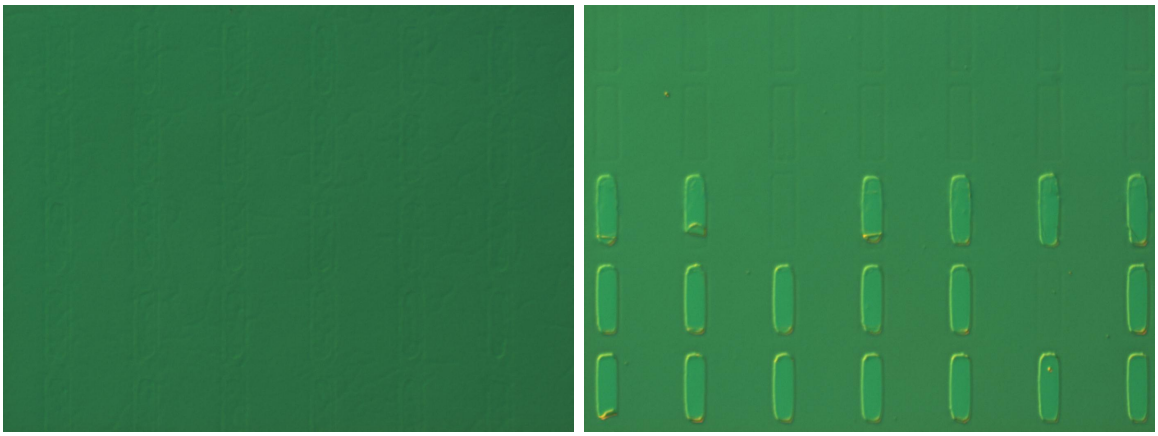

(a) Complete transfer (b) incomplete transfer

Figure 7.8: Micrographs of the PDMS surface after the second transfer printing step. (a) With a short oxygen plasma treatment, the polymer pattern can be successfully transferred and no polymer film is left on the PDMS surface. (b) If the oxygen plasma treatment is too long, it is difficult to achieve a complete transfer of the polymer films in the second transfer step.

transfer printing step. For Figure 7.8a a short-period (∼15 seconds) plasma treatment has been performed on the PDMS layer and a complete transfer of the polymer pattern is observed, with no polymer films left behind. For Figure 7.8b the PDMS surface has been treated with an oxygen plasma for 30 seconds before the printing. Part of the polymer pattern have been transferred while part of the polymer film still exist on the PDMS surface. From our experience, we concluded that a short period (∼10-15 seconds) oxygen plasma treatment of the PDMS surface is optimum for high yield transfer on both of the two transfer printing steps and this condition is used in the rest experiments.

Figure 7.9 shows four micrographs at different stages of the hard-soft printing. Figure 7.9a is an optical micrograph of the stamp after the spin-coating of the polymer layers, and Figure 7.9b is taken on the stamp after the first transfer step, i.e., polymer layers on top of the stamp protrusions have been transferred onto the PDMS surface. Figure 7.9c is the polymer pattern formed on the PDMS surface after the first printing step, and Figure 7.9d is the final polymer pattern transferred onto a glass substrate

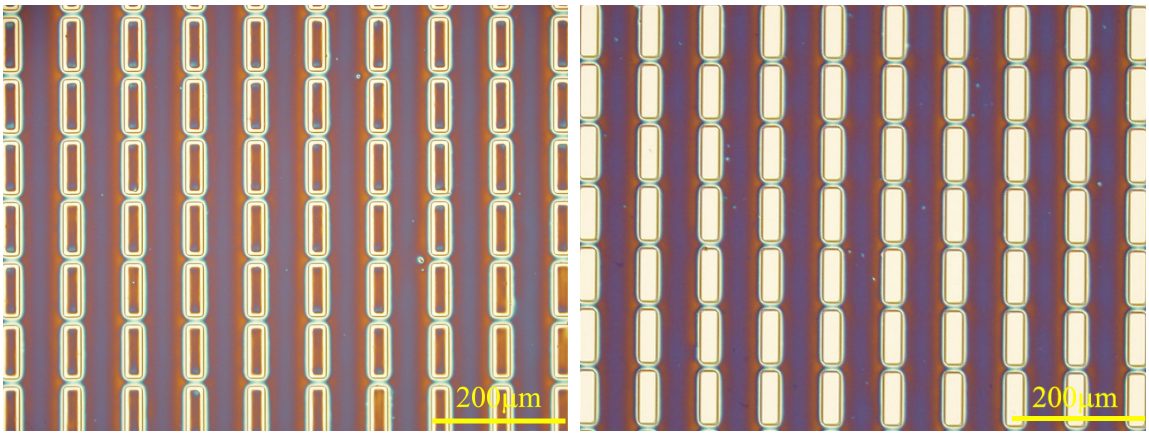

(a) Stamp after spin-coating (b) Clear stamp after first transfer step

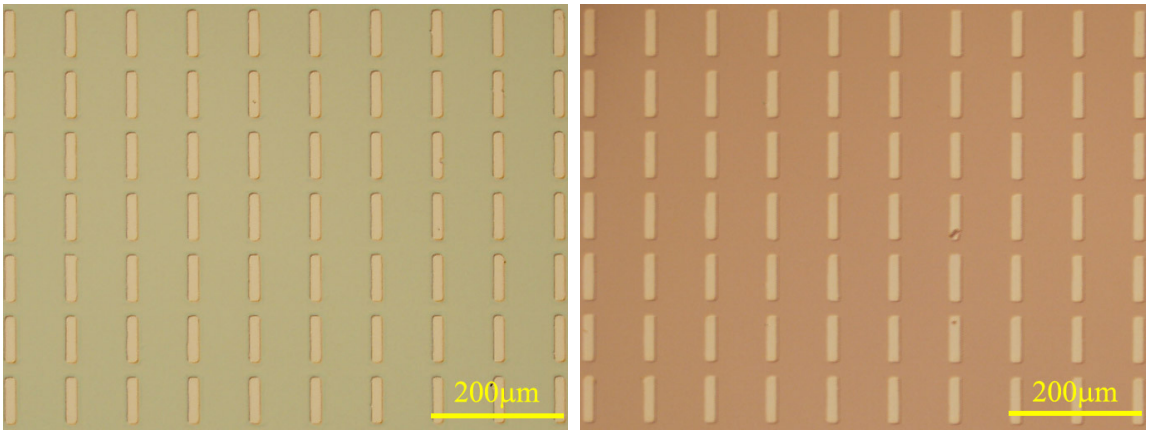

(c) Polymer pattern on PDMS (d) Polymer pattern on glass substrate

Figure 7.9: Polymer patterns at different stages of the hard-soft transfer printing approach.

by the second printing step. A printing condition of 400 psi and 110°C is used for this experiment.

Comparing the hard-soft printed films shown in Figure 7.9 to those from a hard-hard approach shown in Figure 7.3, it is clear that the hard-soft approach is superior in dealing with non-uniform thickness. In fact, since the PDMS layer is so soft, a very low pressure is required in order to achieve a conformal contact. Figure 7.10 shows four more soft printed polymer patterns at 110°C and various pressures: (a) 200 psi, (b) 100 psi, (c) 50 psi, and (d) 20 psi. We can see that even at a low pressure of 20 psi, the un-even polymer film can be transferred successfully, which means the PDMS

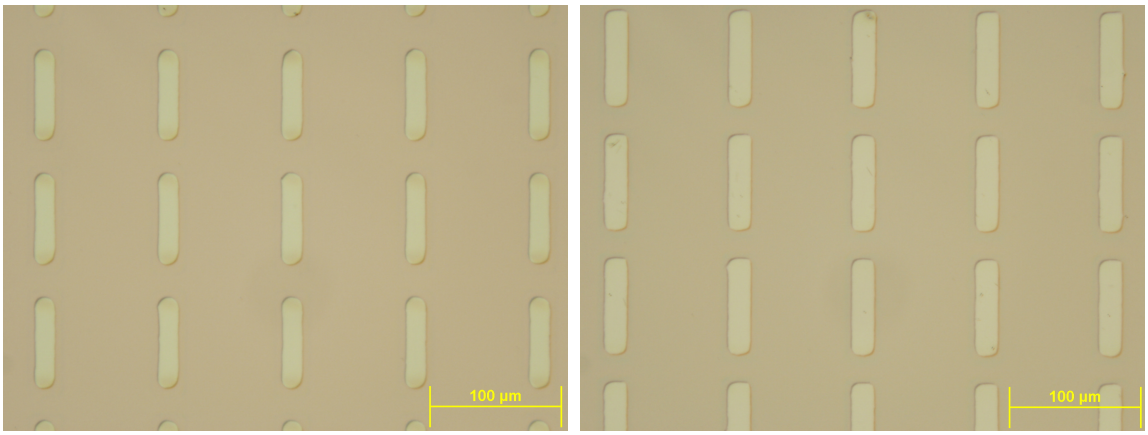

(a) 200 psi (b) 100 psi

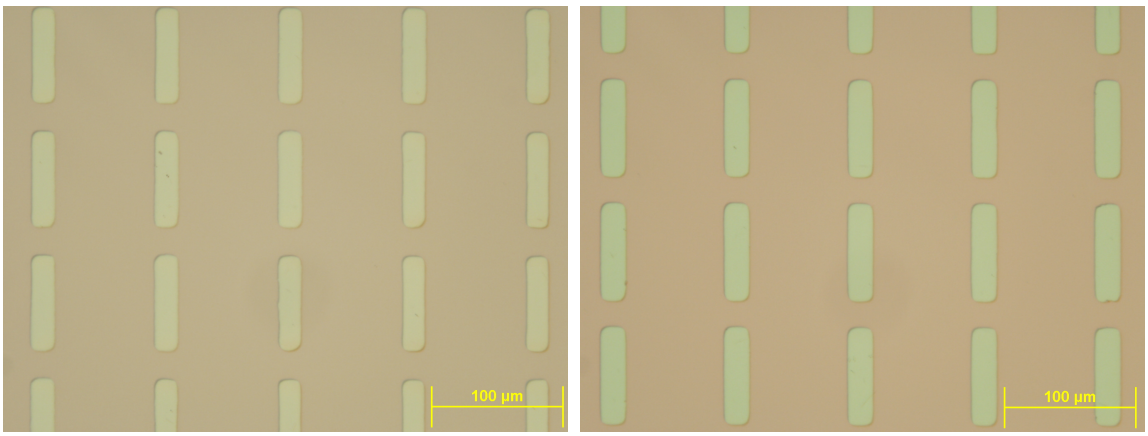

(c) 50 psi (d) 20 psi

Figure 7.10: Polymer patterns formed on the PDMS surface after the first soft-printing step. Printing temperature is $110°C$ while pressure varies.

layer is in intimate contact with the non-uniform polymer layer during the printing process.

Figure 7.11 is a schematic illustration of the hard-soft transfer printing approach in dealing with non-flat surfaces, which has just been described experimentally. Although the polymer film formed by spin-coating is non-uniform in thickness, the elastomeric PDMS layer used can deform easily under low pressures and thus a conformal contact can still be achieved. Complete transfer of the polymer film thus occur. Since the same PDMS layer is also used in the second transfer printing step, it can accommodate a similar surface non-ideality of the layers to be transferred, as in-

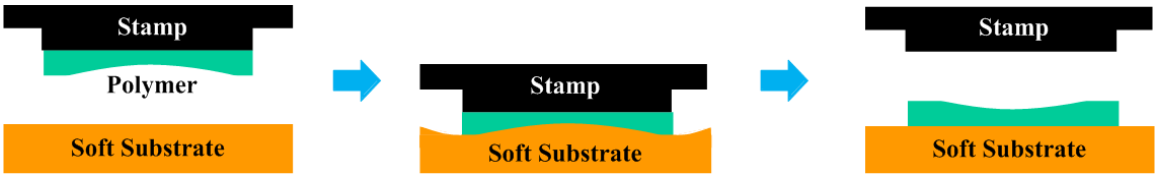

Figure 7.11: Schematic diagram of the hard-soft approach in dealing with non-flat surface.

dicated in the last panel of Figure 7.11. Besides, the real device plate surface is often non-flat with the underlying structures. Thus it is clear that the hard-soft approach is a more versatile method than the hard-hard approach.

Now that the concept of the hard-soft transfer printing approach has been introduced, we can go ahead and demonstrate its ability for organic patterning for full-color OLED displays. An example of the hard-soft approach used for R, G, B subpixel array patterning is given in Figure 7.11. For this demonstration, the three blend films are patterned one-by-one with the hard-soft approach and deposited onto a single glass substrate. A glass substrate is used here as the device plate since visual alignment is required for multi-layer registration. Alignment is done in the same way as shown in Figure 6.3 and its discussions in the text. For this specific experiment all transfer printing steps are done at 400 psi and 110°C. Figure 7.12a is an optical micrograph of the glass substrate after the green light-emitting blend has been deposited by the hard-hard approach. Figure 7.12b is taken after the red light-emitting blend has also been deposited and finally Figure 7.11c is taken after the blue light-emitting blend has also been deposited. The results shown here clearly demonstrate the ability of the hard-soft approach as a patterning method for polymer patterning. The superior capability of the hard-soft approach in dealing with non-flatness is also demonstrated, in sharp contrast to the hard-hard approach.

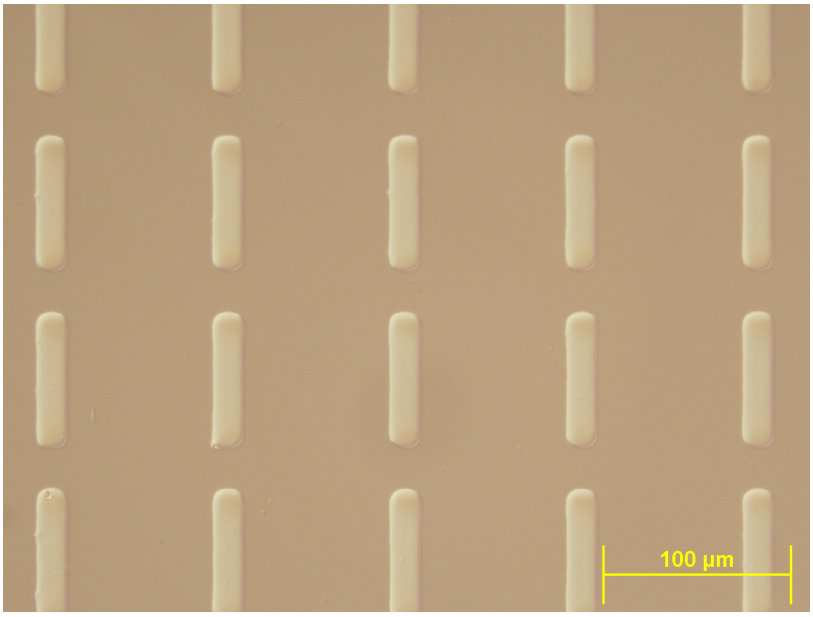

(a)

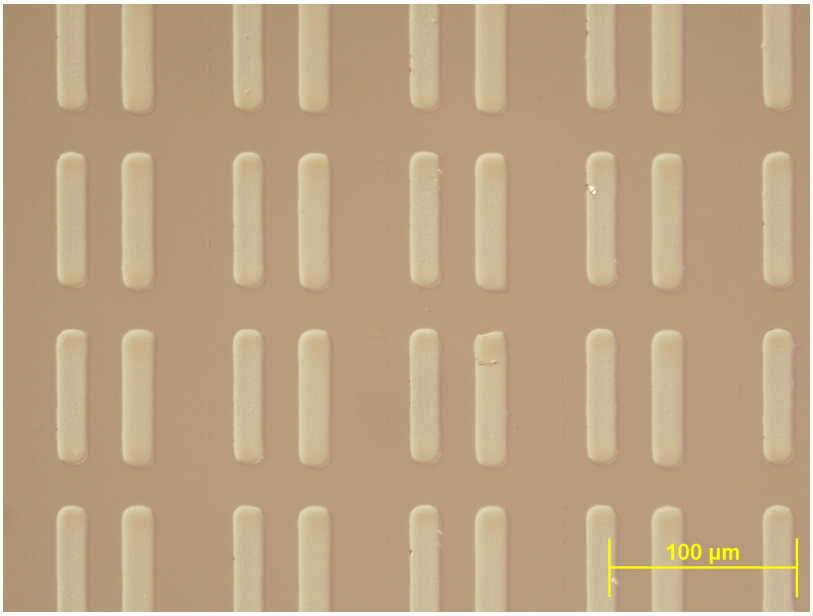

(b)

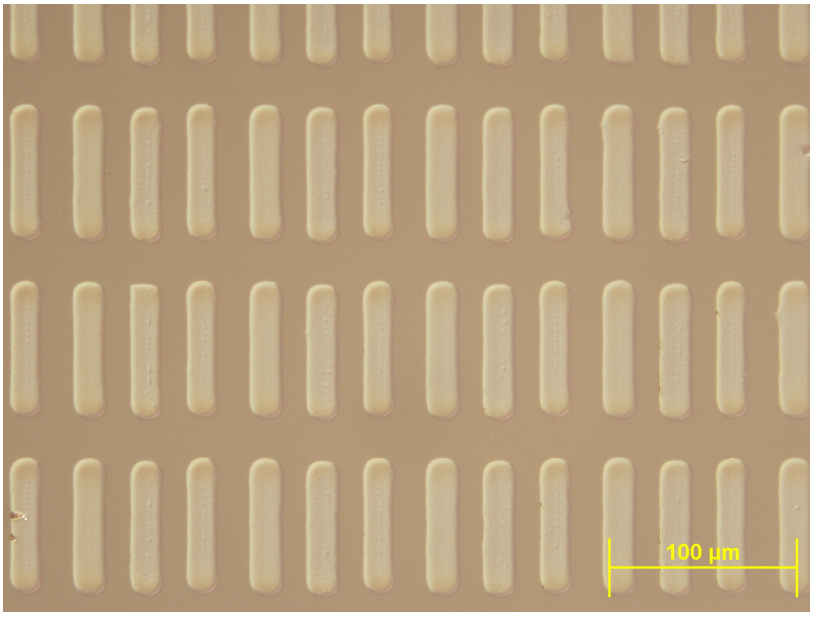

(c)

Figure 7.11: Optical micrographs of transfer printed polymer patterns. (a) After the printing of the green subpixel arrays. (b) After the printing of the green and red subpixel arrays. (c) After the green, red, and blue-subpixels have been deposited.

7.4 Summary

In summary, a transfer printing technique which does not require the breaking of polymer film was demonstrated in this chapter. The polymer film is formed directly on top of the stamp surface by spin coating. Due to the stamp structure with protrusions and recesses, the as-deposited polymer film is discontinuous and can be directly transfer printed. Two different approaches, the "hard-hard" and the "hard-soft" approaches, have been utilized to transfer the polymer film on top of the stamp protrusions to a device plate. While the "hard-hard" approach has fewer processing steps, it lacks the ability to deal with non-planar films. In contrast, the "hard-soft" approach can successfully transfer print non-flat films and thus is more versatile, although it requires more processing steps. Finally, R, G, B subpixel arrays are deposited with the two approaches as demonstrations of the transfer printing method for full-color OLED display fabrication.

Chapter 8

Conclusion

8.1 Summary

In summary, three new printing methods are introduced in this thesis for the patterning of organic films required by full-color OLED displays. All methods introduced here are parallel processes, which may have a high-throughput and low-cost potential. In particular, the transfer printing method introduced in Chapter 6 can achieve very-high-resolution patterning for polymer films, which has not been demonstrated by other patterning methods. It may find its early application in displays which require a very-high resolution, such as in micro-displays.

8.2 Future Work

8.2.1 Transfer Printing Small Molecules

In the past years, there have been more rapid progress in the development of small molecular light-emitting material than in polymers. As a result, the most advanced OLED nowadays are based on small molecules. The transfer printing method introduced in this thesis in Chapter 7 could be easily adapted to be used for small molecule patterning, by direct evaporating the small molecules onto the stamp surface followed by a transfer printing step. Both single layer and multi-layer stacks of small molecules

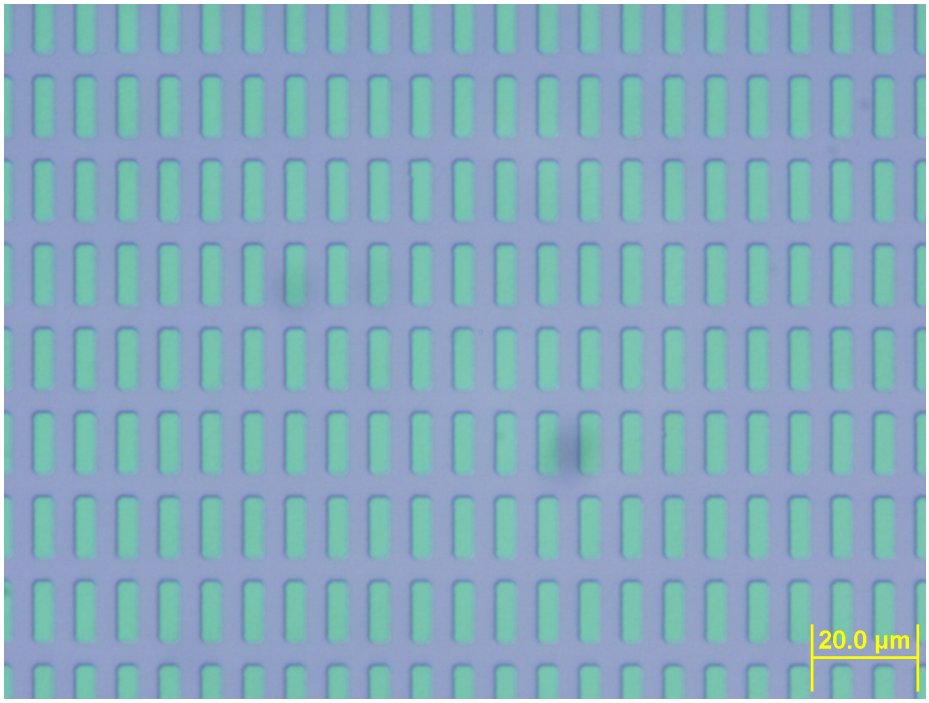

Figure 8.1: An array of Alq_3 film printed onto an ITO-glass substrate, with features at $4\mu m \times 12\mu m$.

can be evaporated onto the stamp and transferred as a whole stack. As preliminary work, we fabricated a silicon stamp with protrusions of $4\mu m \times 12\mu m$. The stamp was treated with PFOTS layer and a thin layer of Alq_3 of about 55 nm was evaporated onto the stamp surface. The Alq_3 layer was then transferred onto an ITO-glass substrate, which is shown in Figure 8.1. The transfer yield was close to 100%. As can be seem from this result, features as small as 4 μm can be easily printed with very-high yield.

8.2.2 Printing Color Filters

Color filters are widely used in LCDs and are usually patterned by three photolithography steps and the cost is high. There have been many efforts to try to pattern the color filters with new printing method, such as ink-jet printing, etc. But the ink-jet printed film uniformity is inferior to photolithography patterned color filters, and thus has difficulty in achieving a uniformity level required by the LCD industry standard.

We think that our transfer printing method can also be utilized to print the color filters for the LCDs. In fact, since the color filters only absorb light emitted from the backlight unit and are not electronically active layers, it might be less challenging to pattern the color filters than to pattern the OLED layers. We believe that our transfer printing method can be easily adapted for color filter patterning.

Bibliography

[1] `http://www.oled-info.com/devices`.

[2] M. Anthamatten, S. A. Letts, and R. C. Cook. Controlling surface roughness in vapor-deposited poly(amic acid) films by solvent-vapor exposure. *Langmuir*, 20:6286–6296, 2004.

[3] A. C. Arias, J. Daniel, B. Krusor, S. Ready, V. Sholin, and R. Street. All-additive ink-jet-printed display backplanes: materials development and integration. *Journal of the SID*, 15:485–490, 2007.

[4] M. Bale, J. C. Carter, C. J. Creighton, H. J. Gregory, P. H. Lyon, P. Ng, L. Webb, and A. Wehrum. Ink-jet printing: the route to production of full-color P-OLED displays. *Journal of the SID*, 14(5):453–459, 2006.

[5] R. Banga, J. Yarwood, A. M. Morgan, and B. Evans. FTIR and AFM studies of the kinetics and self-assembly of alkyltrichlorosilanes and (perfluoroalkyl) trichlorosilanes onto glass and silicon. *Langmuir*, 11(11):4393–4399, 1995.

[6] M. Boroson, L. Tutt, K.n Nguyen, D. Preuss, M. Culver, and G. Phelan. Non-contact OLED color patterning by radiation-induced sublimation transfer (RIST). *SID Digest*, 36:972–975, 2005.

[7] N. W. J. Brooks, R. A. Duckett, and I. M. Ward. Temperature and strain-rate dependence of yield stress of polyethylene. *J. Poly. Sci.: Part B: Poly. Phys.*, 36:2177–2189, 1998.

[8] J. B. Brzoska, L. Benazouz, and F. Rondelez. Silanization of solid substrates—a step toward reproducibility. *Langmuir*, 10:4367–4373, 1994.

[9] J. H. Burroughes, D. D. C. Bradley, A. R. Brown, R. N. Marks, R. H. Friend, P. L. Burns, and A. B. Holmes. Light-emitting diodes based on conjugated polymers. *Nature*, 347:539–541, 11 Oct. 1990.

[10] Y. Cao, C. Kim, S. R. Forrest, and W. Soboyejo. Effects of dust particles and layer properties on organic electronic devices fabricated by stamping. *J. Appl. Phys.*, 98:033713, 2005.

[11] J. Carter, P. Lyon, C. Creighton, M. Bale, and H. Gregory. Developing a scalable and adaptable ink jet printing process for OLED displays. *SID Digest*, 36:523–525, 2005.

[12] J. Chen, V. Leblanc, S. H. Kang, P. J. Benning, D. Schut, M. A. Baldo, M. A. Schmidt, and V. Bulović. High definition digital fabrication of active organic devices by molecular jet printing. *Adv. Func. Mater.*, 17:2722–2727, 2007.

[13] J. H. Choi, K. H. Kim, S. J. Choi, and H. H. Lee. Whole device printing for full colour displays with organic light emitting diodes. *Nanotechnology*, 17:2246–2249, 2006.

[14] A. A. Darhuber, S. M. Troian, and S. Wagner. Physical mechanisms governing pattern fidelity in microscale offset printing. *J. Appl. Phys.*, 90:3602–3609, 2001.

[15] A. A. Darhuber, J. P. Valentino, S. M. Troian, and S. Wagner. Thermocapillary actuation of droplets on chemically patterned surfaces by programmable microheater arrays. *J. Microelectromech. Syst.*, 12:873–879, 2003.

[16] B. de Gans and U. S. Schubert. Inkjet printing of well-defined polymer dots and arrays. *Langmuir*, 20:7789–7793, 2004.

[17] P. G de Gennes. Wetting: statics and dynamics. *Rev. Mod. Phys.*, 57:827–863, 1985.

[18] R. D. Deegan. Capillary flow as the cause of ring stains from dried liquid drops. *Nature*, 389:827–829, 1997.

[19] S. R. Forrest, P. Burrows, and M. Thompson. The dawn of organic electronics. *IEEE Sepctrum*, pages 20–34, Aug 2000.

[20] H. Fox and W. Zisman. *J. Colloid Sci.*, 5, 1950.

[21] M. C. Gather, A. Köhnen, A. Falcou, H. Becker, and K. Meerholz. Solution-processed full-color polymer organic light-emitting diode displays fabricated by direct photolithography. *Adv. Funct. Mater.*, 17:191–200, 2007.

[22] Y. Gorand, L. Pauchard, G. Calligari, J. P. Hulin, and C. Allain. Mechanical instability induced by the desiccation of sessile drops. *Langmuir*, 20:5138–5140, 2004.

[23] T. Graves-Abe, F. Pschenitzka, H. Z. Jin, B. Bollman, J. C. Sturm, and R. A. Register. Solvent-enhanced dye diffusion in polymer thin films for polymer light-emitting diode application. *J. of App. Phys.*, 95:7154–7163, 2004.

[24] D. A. Head. Modeling the elastic deformation of polymer crusts formed by sessile droplet evaporation. *Phys. Rev. E*, 74(2):021601, 2006.

[25] T. R. Hebner and J. C. Sturm. Local tuning of organic light-emitting diode color by dye droplet application. *Appl. Phys. Lett.*, 73(13):1775–1777, 1998.

[26] T. R. Hebner, C. C. Wu, D. Marcy, M. H Lu, and J. C. Sturm. Ink-jet printing of doped polymers for organic light emitting devices. *Appl. Phys. Lett.*, 72(5):519–521, 1998.

[27] G. H. Heilmeier and R. J. Williams. Ferroelectric behavior of liquid crystals and related fluids. *J. Chem. Phys.*, 44:638, 1966.

[28] T. Hirano, K. Matsuo, K. Kohinata, K. Hanawa, T. Matsumi, E. Matsuda, R. Matsuura, T. Ishibashi, A. Yoshida, and T. Sasaoka. Novel laser transfer technology for manufacturing large-sized OLED displays. *SID Digest*, 38:1592–1595, 2007.

[29] H. S. Hwang, A. A. Zakhidov, J. K. Lee, X. Andre, J. A. DeFranco, H. H. Fong, A. B. Holmes, G. G. Malliaras, and C. K. Ober. Dry photolithographic patterning process for organic electronic devices using supercritical carbon dioxide as a solvent. *J. Mater. Chem.*, 18:3087–3090, 2008.

[30] W. Jia and H. Qiu. Fringe probing of an evaporating microdroplet on a hot surface. *Inter. J. Heat and Mass Transfer*, 45:4141–4150, 2002.

[31] H. Jin and J. C. Sturm. Large-Area Wet Micro-Printing (LAMP) for organic device patterning. *Mater. Res. Soc. Symp. Proc.*, 871E:I6.27, 2005.

[32] H. Jin and J. C. Sturm. Large-Area Wet Micro-Printing (LAMP) for organic device patterning. In *5th Annual Flexible Displays and Microelectronics Conference*, Phoenix, AZ, 2006.

[33] H. Jin and J. C. Sturm. Profile optimization of wet-printed polymers for OLED devices. In *Materials Research Society Spring Meeting*, San Francisco, CA, 2006.

[34] H. Jin and J. C. Sturm. Improved emission uniformity in polymer OLEDs fabricated by Large-Area Wet Micro-Printing. In *6th Annual Flexible Displays and Microelectronics Conference*, Phoenix, AZ, 2007.

[35] H. Jin and J. C. Sturm. Macroscopic vs. microscopic profile optimization for printed OLED devices by Large-Area Wet Micro-Printing. In *Electronic Materials Conference*, University of Notre Dame, 2007.

[36] H. Jin and J. C. Sturm. Hard-hard vs. hard-soft approaches to transfer printing for full-color OLED patterning using direct organic deposition on patterned stamps. In *Materials Research Society Spring Meeting*, San Francisco, CA, 2008.

[37] H. Jin and J. C. Sturm. Transfer printing of electroluminescent polymer for full-color OLED patterning. In *7th Annual Flexible Displays and Microelectronics Conference*, Phoenix, AZ, 2008.

[38] H. Jin and J. C. Sturm. Performance of OLEDs with polymer layers fabricated by transfer printing. In *8th Annual Flexible Electronics and Displays Conference*, Phoenix, AZ, 2009.

[39] H. Jin and J. C. Sturm. Super-high-resolution transfer printing for full-color OLED display patterning. In *SID Display Week*, page 40.2, San Antonio, TX, 2009.

[40] M. Kashiwabara, K. Hanawa, R. Asaki, I. Kobori, R. Matsuura, H. Yamada, T. Yamamoto, A. Ozawa, Y. Sato, S. Terada, J. Yamada, T. Sasaoka, S. Tamura, and T. Urabe. Advanced AM-OLED display based on white emitter with microcavity structure. *SID Digest*, 35:1017–1019, 2004.

[41] M. Kitagawa. Power law relationship between yield stress and shear modulus for glassy polymers. *J. Poly. Sci.: Poly. Phys. Ed.*, 15:1601–1611, 1977.

[42] E. Kitazume, K. Takeshita, K. Murata, Y. Qian, Y. Abe, M. Yokoo, K. Oota, and T. Taguchi. Development of polymer light-emitting diode (PLED) displays using the relief printing method. *SID Digest*, 37:1467–1470, 2006.

[43] Y. P. Kong, L. Tan, S. W. Pang, and A. F. Yee. Stacked polymer patterns imprinted using a soft inkpad. *J. Vac. Sci. Technol. A*, 22(4):1873–1878, 2004.

[44] D. Lee, J. Chung, J. Rhee, J. Wang, S. Hong, B. Choi, S. Cha, N. Kim, K. Chung, H. Gregory, P. Lyon, C. Creighton, J. Carter, M Hatcher, O. Bassett, M. Richardson, and P. Jerram. Ink-jet printed full-color polymer LED displays. *SID Digest*, 36:527–529, 2005.

[45] S. T. Lee, B. D. Chin, M. H. Kim, T. M. Kang, M. W. Song, J. H. Lee, H. D. Kim, H. K. Chung, M. B. Wolk, E. Bellmann, J. P. Baetzold, S. Lamansky, V. Savvateev, T. R. Hoffend Jr., J. S. Staral, R. R. Roberts, and Y. Li. A novel patterning method for full-color organic light-emitting devices: Laser Induced Thermal Imaging (LITI). *SID Digest*, 35:1008–1011, 2004.

[46] S. T. Lee, J. Y. Lee, M. H. Kim, M. C. Suh, T. M. Kang, Y. J. Choi, J. Y. Park, J. H. Kwon, H. K. Chung, J. Baetzold, E. Bellmann, V. Savvateev, M. Wolk, and S. Webster. A new patterning method for full-color polymer light-emitting devices: Laser Induced Thermal Imaging (LITI). *SID Digest*, 33:784–787, 2002.

[47] S. T. Lee, M. C. Suh, T. M. Kang, Y. G. Kwon, J. H. Lee, H. D. Kim, and H. K. Chung. LITI (Laser Induced Thermal Imaging) technology for high-resolution and large-sized AMOLED. *SID Digest*, 38:1588–1591, 2007.

[48] K. Long. *Towards Flexible Full-Color Active Matrix Organic Light-Emitting Displays: Dry Dye Printing for OLED Integration and* 280°*C Amorphous-Silicon Thin-Film Transistors on Clear Plastic Substrates*. PhD thesis, Princeton University, Princeton, NJ, 2006.

[49] D. E. Mentley. State of flat-panel display technology and future trends. *Proc. IEEE*, 90(4):453–459, Apr 2002.

[50] S. M. Miller, S. M. Troian, and S. Wagner. Direct printing of polymer microstructures on flat and spherical surfaces using a letterpress technique. *J. Vac. Sci. Technol.*, B20:2320–2327, 2002.

[51] C. D. Müller, A. Falcou, N. Reckefuss, M. Rojahn, V. Wiederhirn, P. Rudati, H. Frohne, O. Nuyken, H. Becker, and K. Meerholz. Multi-colour organic light-emitting displays by solution processing. *Nature*, 42:829–833, 2003.

[52] L. Pauchard and C. Allain. Stable and unstable surface evolution during the drying of a polymer solution drop. *Phys. Rev. E*, 68(5):052801, 2003.

[53] M. Pope, H. P. Kallmann, and P. Magnante. Electroluminescence in organic crystals. *J. Chem. Phys.*, 38:2042–2043, 1963.

[54] F. Pschenitzka. *Patterning techniques for polymer light-emitting devices.* PhD thesis, Princeton University, Princeton, NJ, 2002.

[55] F. Pschenitzka and J. C. Sturm. Three-color organic light-emitting diodes patterned by masked dye diffusion. *Appl. Phys. Lett.*, 74:1913–1915, 1999.

[56] J. Richeton, S. Ahzi, L. Daridon, and Y. Remond. Modeling of strain rates and temperature effects on the yield behavior of amorphous polymer. *J. Phys. IV France*, 110:39–44, 2003.

[57] Z. Shen, P. E. Burrows, V. Bulovic, S. R. Forrest, and M. E. Thompson. Three-color, tunable, organic light-emitting devices. *Science*, 276:2009–2011, June 27, 1997.

[58] T. Shimoda, K. Morii, S. Seki, and H. Kiguchi. Inkjet printing of light-emitting polymer displays. *MRS Bulletin*, 28:821–827, 2003.

[59] M. Stein. *Organic vapor phase deposition and vapor jet printing for electronic and optoelectronic device applications.* PhD thesis, Princeton University, Princeton, NJ, 2004.

[60] M. Stein, P. Peumans, J. B. Benziger, and S. R. Forrest. Direct, mask- and solvent-free printing of molecular organic semiconductors. *Adv. Mater.*, 16:1615–1620, 2004.

[61] C. W. Tang and S. A. VanSlyke. Organic electroluminescent diodes. *Appl. Phys. Lett.*, 51(12):913–915, 1987.

[62] C. W. Tang, S. A. VanSlyke, and C. H. Chen. Electroluminescence of doped organic thin films. *J. Appl. Phys.*, 65(9):3610–3616, 1989.

[63] V. N. Truskett and K. J. Stebe. Influence of surfactants on an evaporating drop: fluorescence images and particle deposition patterns. *Langmuir*, 19:8271–8279, 2003.

[64] L. R. van den Doel and L. J van Vliet. Temporal phase-unwrapping algorithm for dynamic interference pattern analysis in interference-contrast microscopy. *App. Opt.*, 40(25):4487–4500, 2001.

[65] S. R. Wasserman, Y. T. Tao, and G. M. Whitesides. Structure and reactivity of alkylsiloxane monolayers formed by reaction of alkyltrichlorosilanes on silicon substrates. *Langmuir*, 5:1074–1087, 1989.

[66] C. C. Wu. *Light-emitting devices based on doped polymer thin films.* PhD thesis, Princeton University, Princeton, NJ, 1997.

[67] C. C. Wu, J. C. Sturm, R. A. Register, J. Tian, E. P. Dona, and M. E. Thompson. Efficient organic electroluminescent devices using single-layer doped polymer thin

films with bipolar transport abilities. *IEEE Trans. Elec. Dev.*, 44:1269–1281, 1997.

[68] C. C. Wu, C. I. Wu, J. C. Sturm, and A. Kahn. Surface modification of indium tin oxide by plasma treatment: an effective method to improve the efficiency, brightness, and reliability of organic light emitting devices. *Appl. Phys. Lett.*, 70(11):1348–1350, 1997.

[69] K. J. Yoo, S. H. Lee, A. S. Lee, C. Y. Im, T. M. Kang, W. J. Lee, S. T. Lee, H. D. Kim, and H. K. Chung. 302-ppi high-resolution AMOLED using laser-induced thermal imaging. *SID Digest*, 36:1344–1347, 2005.

[70] B. Young. Flexible displays: the market and the challenges. In *7th annual flexible displays and microelectronics Conference*, page 1.2a, Phoenix, AZ, 2008.